OPTIMAL CONTROL OF ATMOSPHERIC AIR INJECTION FOR ENHANCED OIL RECOVERY

By

Shahrad Khodaei Booran

BEng in Chemical Engineering Co-op, Ryerson University, Toronto, 2011

MASc in Chemical Engineering, Ryerson University, Toronto, 2013

A dissertation presented to

Ryerson University

in partial fulfillment of the

requirements for the degree of

Doctor of Philosophy

in the program of

Chemical Engineering

Toronto, Ontario, Canada, 2017

Author's Declaration

I hereby declare that I am the sole author of this dissertation. This is a true copy of the dissertation, including any required final revisions, as accepted by my examiners.

I authorize Ryerson University to lend this dissertation to other institutions or individuals for the purpose of scholarly research.

I further authorize Ryerson University to reproduce this dissertation by photocopying or by other means, in total or in part, at the request of other institutions or individuals for the purpose of scholarly research.

I understand that my dissertation may be made electronically available to the public.

OPTIMAL CONTROL OF ATMOSPHERIC AIR INJECTION FOR ENHANCED OIL RECOVERY

Doctor of Philosophy

2017

Shahrad Khodaei Booran

Chemical Engineering

Ryerson University

Abstract

Gas-based enhanced oil recovery (EOR) processes rely on the injection of gases such as carbon dioxide, nitrogen, and natural gas into heavy oil reservoirs to reduce inherent oil viscosity. Although these processes are very promising, they face the problem of limited and costly gas supply.

This study investigates the conditions, specifically temperature variation, under which freely available air at low temperatures, low pressures, and non-reactive environments for heavy oil recovery. To that end, preliminary experiments are carried out to demonstrate the possibility of beneficial effects of air temperature variation with time. Furthermore, this research aims to utilize the theory of optimal control to determine optimal air temperature versus time function to maximize the heavy oil recovery. For this purpose, the conditions necessary for optimal control are derived and utilized in a computational algorithm.

The preliminary experiments are executed by injecting air into a lab-scale heavy oil reservoir at different pressures (0.169-0.514 MPa absolute) and temperatures in the range of 25-90^{o}C. Reservoirs of four different permeabilities (40-427 Darcy) are used in experiments. When air is injected with a periodic temperature variation between 90^{o}C and 75^{o}C that has an average of 78^{o}C, the recovery is increased from 58.2% to 69.1% of the original-oil-in-place (OOIP) in comparison to that using constant temperature air injection at the maximum temperature of 90^{o}C. That is a considerable improvement of oil recovery by 18.6%.

Furthermore, utilizing optimal control the optimal interfacial temperature versus time (control policy) is determined between 90^{o}C and 82^{o}C, which registers 20.66% increase in the oil recovery in comparison to that at the constant temperature of 90^{o}C. The accuracy of optimal control is experimentally validated. The results show that the average relative difference between the predicted heavy oil recovery and the experimental value is a low value of 1.82%.

Acknowledgements

I wish to express my sincere gratitude to Dr. Simant R. Upreti, and Dr. Farhad Ein-Mozaffari for their kind guidance, supervision, and suggestions throughout the entire period of my studies.

I am very grateful for the invaluable assistance of faculty members and technologists in the Chemical Engineering Department of Ryerson University, especially those provided by Ali Hemmati, Daniel Boothe, and Tondar Tajrobehkar during the equipment manufacture and system setup.

I would also like to thank Goretti Praticante and Louise Lichacz in the Department of Chemical Engineering.

Dedication

Dedicated to my mother for her love and support throughout my life.

Table of Contents

List of Tables

List of Figures

List of Appendices

List of Symbols and Nomenclature

A	area, m^2
C_p	specific heat capacity, joules/g °C
$D(\omega, T)$	dispersion coefficient of solvent in media, m^2/s
D_p	diameter of the particle, m
g	gravity, m/s^2
I	objective functional
J	augmented objective functional
K	permeability of the medium, Darcy
K_r	relative permeability of the medium
k	thermal conductivity coefficient
m	cumulative mass of produced live oil, g
P	pressure, MPa
Q	volumetric fluid flow rate through the media, m^3/s
r	distance along the radial direction, m
R	radius of the cylindrical medium, m
S	finite differential surface area along r-direction, m^2
T	temperature, ^oC
T_{int}	interfacial temperature of the solvent at the solvent-heavy oil interface, ^oC
t	time, min
t_f	duration of the oil recovery experiment, min
V	volume of a finite element in the medium, m^3
v	Darcy velocity, m/s
z	distance along the vertical direction, m
Z	height of heavy oil inside the medium at a given r and t, m
Z_o	initial height, m

Greek Symbols

ϕ	porosity of the medium
$\lambda_1, \lambda_2, \lambda_3$	costate variables
μ	viscosity of the live oil, mPa.s
μ_o	live oil viscosity coefficient, kg/m.s
ρ	live oil density, kg/m^3
ω	mass fraction of gas solvent in heavy oil
ω_{int}	mass fraction of the gas solvent at the solvent-heavy oil interface
π	pi value

Abbreviations

API	American Petroleum Institute
ASP	Alkali-Surfactant-Polymer
BFGS	Broyden-Fletcher-Goldfarb-Shanno Method
CSS	Cyclic Steam Stimulation
EOR	Enhanced Oil Recovery
PDE	Partial Differential Equation
MEOR	Microbial Enhanced Oil Recovery
NMR	Nuclear Magnetic Resonance Spectroscopy
OOIP	Original-oil-in-place
ODE	Ordinary Differential Equation
SAGD	Steam Assisted Gravity Drainage
Vapex	Vapor extraction

Chapter 1: Introduction

1.1 Crude Oil and Its Characteristics

In general, crude oil is a mixture of liquid hydrocarbons of varying degree of volatility. It also contains some nitrogen, sulfur, and oxygen.[1] Although, the percentage of each component may vary widely in different locations. Regardless of variations, however, almost all crude oil range from 82 to 87 percent carbon by weight and 12 to 15 percent hydrogen by weight.[2]

Crude oils are typically classified according to their viscosities and API (American Petroleum Institute) gravities, which is defined based on the ratio of the weight of equal volumes of a crude oil and pure water at standard conditions. Table 1 shows the grades of the crude oils based on API gravity. Furthermore, the types of crude oil reservoirs are conventional and unconventional based on their viscosities and API gravities. The viscosity of conventional oil reservoirs is lower than 100 centipoise (cP) with API gravity of 20^o or greater, while unconventional oil reservoirs have the viscosity higher than 100 cP with API gravity of 20^o or less.[2]

Conventional oil reservoirs typically contain the highest quality, lightest oil, which can flow from underground reservoirs with comparative ease. On the other hand, unconventional oil reservoirs that have a high viscosity (10^4 – 10^6 cP or even higher) are often tar-like, and require external forces for oil recovery. Some examples of unconventional oil reservoirs are oil shale, bitumen, heavy and extra-heavy crude oils, and deep-sea oils.[3]

Table 1: Classification of crude oil according to the API degree

Crude oil classifications	API degree (º)
medium crude oil	higher than 31.1
medium crude oil	31.1 to 22.3
heavy crude oil	22.3 to 10
extra-heavy crude oil	Below 10

Typically, most heavy oil and natural bitumen are thought to be expelled from source rocks as light or medium oil and later converted to heavier components by bacterial degradation in subsurface reservoirs.[4,5,6]. Heavy oils are asphaltic, dense and viscous oils having an API gravity of between 10º and 20º API and a viscosity greater than 100 cP. Bitumen or tar sands share similar attributes to heavy oil but are yet more dense and viscous with API gravity less than 10º API and viscosities usually greater than 10,000 cP.[7]

1.2 Crude Oil and Energy Source

With 90 million barrels of oil consumed worldwide daily, conventional oil reserves are being drawn down rapidly. New sources of hydrocarbon are required to supplement the decline of traditionally produced light crudes with low viscosity. Alternative sources of hydrocarbon energy include coal, shale production of oil and gas, heavy oil/bitumen and oil shale.[8] The high viscosity of these non-conventional crude oils demand more energy intensive operations not only for their production and upgrading but also for transportation and consequently they are costlier to extract. However, yet, with estimated reservoirs of 3.3960×10^3 billion barrels of heavy oil (i.e., Venezuela in the Orinoco heavy-oil belt)[9] and 5.5050×10^3 billion barrels of bitumen (i.e., Alberta, Canada),

they represent alternative ample hydrocarbon resources for the oil production at an economically-viable scale.[10]

The heavy oil and bitumen reservoirs in Canada, in particular, are one of the largest hydrocarbon resources in the world.[2] Alberta's tar sand resides in three deposits (Athabasca, Cold Lake, and Peace River) and covers an area equal to the size of the province of New Brunswick.[8,11] There are estimated 1.7-2.5 trillion barrels of bitumen in place in Alberta's oil sands. Canada's recoverable oil resource is second only to Saudi Arabia's.

At current production rates, resources from Alberta's tar sands could supply Canada's energy needs for more than 500 years, or the total world needs for up to 15 years and about 39% of Canada's total oil production is from oil sands.[2]

Currently, approximately 1.3 million barrels are produced per day and the production is expected to grow to three million bpd by 2020.[8,11] This fact indicates that heavy oil and bitumen reservoirs have tremendous potential for meeting the ever-increasing demands of energy and useful petroleum products. However, as it was mentioned previously, the main difficulty in the heavy oil and bitumen recovery is their immobility under reservoir conditions due to their high viscosity ($10^4 – 10^6$ cP or even higher).[12]

Thus, the active production of heavy oil and bitumen demands specific technological solutions that are economical as well as environmentally benign.[8,11,12]

1.3 Crude Oil Recovery

In general, the production of crude oil from an underground reservoir can be classified in three terms: primary, secondary, and tertiary production.

The initial production of crude oil from an underground reservoir is accomplished by the use of natural reservoir energy. This type of production is termed primary products. Sources of natural reservoir energy that lead to major products include the swelling of reservoir fluids, the release of solution gas as the reservoir pressure declines, nearby communicating aquifers, and gravity drainage.[11,13] However, when the natural reservoir energy declines, it becomes necessary to augment the natural energy with an external source, such as injection of fluids, either natural gas or water. The use of this injection scheme is called a secondary recovery operation.[13] When water injection is used as the secondary recovery process, the process is referred to as water flooding.

The main purpose of either natural gas injection or a water injection process is to re-pressurize the reservoir and then to maintain the reservoir at a high pressure.[11,13] Similarly, natural gases can be injected into the oil reservoir to maintain reservoir pressure.[13] The recovery efficiency of a water flood is largely a function of the sweep efficiency of the flood and the ratio of the oil and water viscosities.

Sweep efficiency is a measure of how well the water has come in contact with the available pore space in the oil bearing zone. When an injected water is much less viscous than the oil it is meant to displace, the water could begin to finger, or channel, through the reservoir. This is referred to as viscous fingering and leads to significant bypassing of residual oil and lower flooding

efficiencies. This bypassing of residual oil is an important issue in applying enhanced oil recovery techniques as well as in water flooding.[8,11,13]

Tertiary recovery processes were developed for application in situations in which secondary processes had become ineffective. However, the same tertiary processes were also considered for reservoir applications for which secondary recovery techniques were not used because of low recovery potential.

The tertiary recovery processes are also known as Enhanced Oil Recovery (EOR) processes. EOR processes attempt to create favorable conditions for improving oil recovery through (i) swelling of oil, (ii) increase in capillary number, (iii) reduction of the oil viscosity, (iv) reduction of the interfacial tension between the displacing fluid and the oil, (v) reduction of capillary forces in the reservoir, and (vi) alternation of the reservoir rock wettability.[3,14]

1.4 Heavy Oil and Bitumen and Enhanced Oil Recovery

Enhanced oil recovery (EOR) processes are used to recover heavy oil or reduce residual oil from reservoirs when oil cannot be either produced at all or improved economically using primary and secondary recovery processes.[1,15]

In general, EOR processes are classified into four main categories, thermal EOR, chemical EOR, gas EOR, and microbial EOR.[3] Figure 1 represents four types of EOR processes, which are typically defined by the nature of the fluid injected into the reservoir.

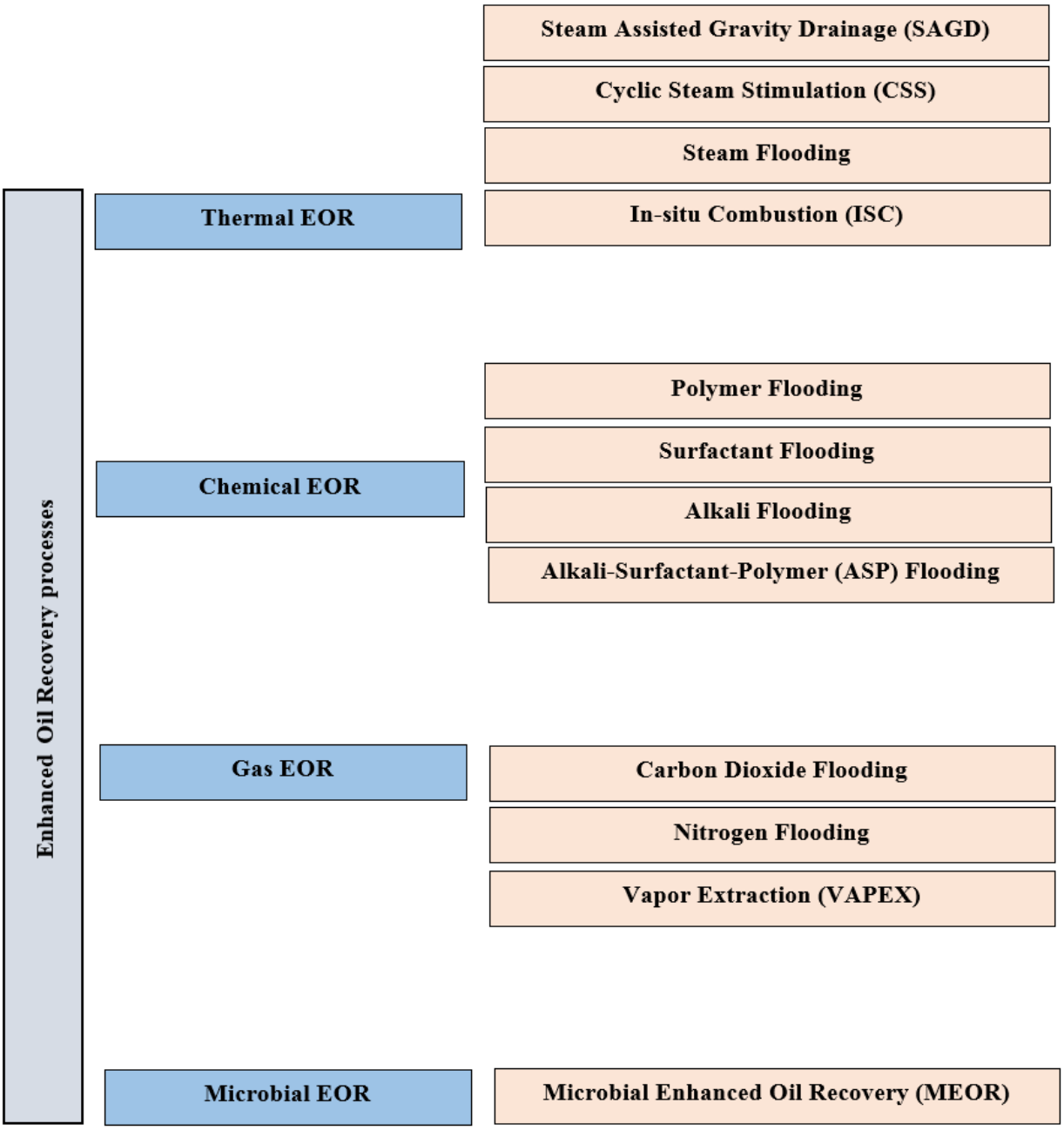

Figure 1: Classification of EOR processes

The total world oil production from EOR is about 3.5% of the total daily oil production of 85 million barrels.[14] The majority of EOR oil production is from thermal methods contributing about 2 million barrels of oil per day.[14] Thermal EOR relates to processes that require thermal energy

through hot water, steam, or air injection to decrease the viscosity of heavy oil and bitumen.[16] Thermal EOR process, particularly Steam Assisted Gravity Drainage or SAGD is the most common in-situ process presently used for heavy oil and bitumen recovery due to its simplicity and high recovery efficiency. It is noteworthy that SAGD accounts for 25-75% of the OOIP.[8,17] For example, Alberta in 2009 produced 664,000 barrels per day of heavy oil using SAGD.[11] However, thermal processes also face some inherent limitations.[8,11,18] In thermal EOR, the steam is generated by burning natural gases; thus the cost of producing steam is very sensitive to increases in the price of natural gas. Furthermore, steam generation facilities are required and accounted for about 30% of the capital cost in SAGD. Also, steam production requires a significant source of water, usually from lake or aquifer. Additionally, most thermal EOR processes have high heat loss energy intensity and have large negative impacts on the environment.[8,11] Despite well-insulated, the heat loss is inevitable, through the well casing, to the overburden and ground water below the reservoir. Moreover, greenhouse gas emissions and effluent water disposal pose significant challenges for these processes.[2,8,11] It is important to note that over the last decade researchers have combined different EOR processes to enhance the production yield or reduce energy consumption or negative environmental impacts. One of the examples is Steam-Solvent processes.

Thermal EOR is followed by gas-based EOR, which contributes about a two-thirds of a million barrels of oil per day.[14] Gas-based enhanced oil recovery (EOR) processes rely on the injection of gases such as carbon dioxide, nitrogen, and natural gas into heavy oil reservoirs to reduce inherent oil viscosity. The presence of a dissolved gas in the oil enhances the recovery by (i) creating a saturated displacement front by swelling oil in reservoir pores, and (ii) reducing the interfacial tension at the interface between the oil and water.[12,19] As of today, carbon dioxide injection has

gained considerable attention for oil recovery, especially in the US.[20,21] In 2006, about 37% of oil production in the US was contributed by carbon dioxide-based EOR, due to the availability of cheap carbon dioxide from natural sources.[22] Some of the advantages of carbon dioxide are its high solubility in oil and availability from large and inexpensive natural gas sources.[3,22-25] It has been reported that carbon dioxide EOR is economically attractive at oil prices around $20 US per barrel.[26,27] However, carbon dioxide injection faces many challenges including: (i) solvent loss caused by pipelines corrosion (ii) long start-up times and low initial rates oil recovery, (iii) high cost of capture and storage of carbon dioxide from air or other sources excluding natural sources, power plants or industrial sources at the current time.[3,22,23,28]

The oil production from chemical EOR is estimated about a third of a million barrels of oil per day. Chemical EOR is a flooding process where chemical agents like polymer, surfactant, alkali or any combination [alkali-surfactant-polymer (ASP)] are used to either reduce the interfacial tension between the oil and the injected fluid or to improve the volumetric sweep efficiency.[29,30] Polymers such as polyacrylamide and polysaccharides are used to improve sweep efficiency.[29,31] The application of chemical flooding declined sharply in the US after 1988 due to rising prices of chemical flooding agents primarily surfactant.[29,31,33] ASP flooding has received considerable attention in China in the last decade.[29] Reservoir characteristics is another factor that limits the applicability of chemical EOR. For example, the reservoir features such as temperature, depth, salinity, and pH highly impact on the performance of chemical EOR.[2]

The heavy oil recovery using microbial injection process though is quite small due to lack of complete understanding of the mechanisms involved in microbial injection process and the impact

of each device on different reservoir conditions.[35] It may be noted that EOR projects are strongly influenced by economics and crude oil prices. Therefore, since oil prices are expected to rise substantially in the future, EOR processes would become more economical to use.[22,26]

1.5 Challenges and Research Objectives

Among the non-thermal EOR processes, the important ones are the gas EOR processes. Over the years, many researchers have conducted various lab-scale experiments by using pure or mixture hydrocarbon gases (i.e., propane, butane, and hexane) injection for heavy oil recovery.

However, some of the major limitations of gas EOR are high costs and limited supplies of gas solvents, and solvent losses from oil reservoirs. Therefore, we have to look for those solvents for heavy oil recovery that are readily available at low costs, and are environmentally friendly.

Based on aforementioned considerations, atmospheric air injection is an potentially viable process for heavy oil recovery because of its free availability.[34,35] As a result, the first objective of this study is to investigate the applicability of freely atmospheric air as a solvent for heavy oil recovery under moderate and non-reactive temperature and pressure conditions in a solvent-assisted gravity drainage process.

For this purpose, experiments are performed with a lab-scale reservoir model and air injection at sufficiently low temperatures (25^{o}C-90^{o}C) and pressures (0.169-0.514 MPa) (absolute) to preclude any hydrocarbon oxidation.

The second objective of this study is to prove experimentally that oil production can be increased by suitable varying air injection temperature with time. The air interfacial temperature versus time is considered as a control function.

The third objective of this study is to develop a robust mathematical model of the experimental recovery process, utilize it to determine the optimal control function, and validate the function.

1.6 Structure of the Dissertation

This dissertation is organized into six chapters as follows.

Chapter 1: This chapter provides a brief background of crude oil and different processes of heavy oil recovery. Also, the research objectives and organization of the text are introduced.

Chapter 2: In this chapter, literature review is provided on gas EOR and the impact of different factors (i.e., viscosity) on gas EOR performance. This chapter also presents optimal control applications for enhanced oil recovery.

Chapter 3: The experimental methods and procedures are explained in this chapter.

Chapter 4: This chapter presents optimal control of the air-based gas EOR. The optimal control is formulated. The necessary conditions are derived for the maximum of the heavy oil recovery. An optimal control algorithm is developed to determine optimal air interfacial temperature versus time policy to maximize oil production.

Chapter 5: In this chapter, the experimental and numerical simulation results are presented, analyzed and discussed in details.

Chapter 6: This chapter summarizes the contributions of this research, and identifies recommendations for future work.

Chapter 2: Literature Review

As previously mentioned, gas EOR processes rely on the injection of gases such as carbon dioxide into heavy oil reservoirs to reduce native oil viscosity. The following sections discuss in detail about the mechanism of gas EOR, the factors that impact heavy oil recovery, and optimal control application for enhanced oil recovery.

2.1 Mechanism of Gas EOR

The mechanism of gas EOR is based on the phenomenon of viscosity reduction of heavy oil in the presence of the absorbed solvent (in this case atmospheric air injected), which is predominantly nitrogen.[36,37] The absorbed solvent facilitates oil recovery by reducing the interfacial tension between the oil and water, and creating a saturated displacement front by swelling oil in the reservoir pores. As a result, the heavy oil reservoirs become mobile and flow under gravity for easy recovery.[12] Furthermore, the gas solvent mixes with the heavy oil phase through combined phenomena of molecular diffusion, viscosity reduction, capillary action, gravitational flow, and surface renewal. The net effect is dispersion, which cannot be described by solvent diffusivity alone.[38]

2.2 Factors that Influence Gas EOR

Some of the relevant parameters and factors that impact gas EOR, such as viscosity, diffusion, dispersion, and permeability of the heavy oil reservoir are discussed next.

2.2.1 Heavy Oil Viscosity and Gas EOR

As indicated before, one of the biggest challenges of heavy oil recovery is the high viscosity of heavy oil that does not flow spontaneously and cannot be produced efficiently with conventional primary and secondary oil recovery processes.[1,15] In gas EOR, the gaseous solvent injection results in viscosity reduction. The viscosity of heavy oil and bitumen is a strong function of temperature in comparison with pressure, but while gases are dissolved in heavy oil and bitumen, pressure can influence the viscosity.[1,15] In general, heavy oil viscosity is the function of temperature, the concentration of dissolved gases, pressure, and asphaltene. Lederer has reported that the correlation for dependence of viscosity on the solvent concentration as [39]

$$\mu_{mix} = \mu_s^{fs} \mu_B^{fB} \tag{1}$$

where

$$f_B = \frac{\gamma C_B}{\gamma C_B + C_s};\ f_s = 1 - f_B \tag{2}$$

where γ is a weight factor having a value between zero and unity, f_B is a weighted fraction of the more viscous component, μ_B and μ_s are the viscosities (Pa.s) of bitumen and the injected solvent respectively, and C_B and C_s are the volume fraction of bitumen and solvent, respectively.[39] Das and Butler (1996) used the two parameters viscosity and temperature, and their correlation as given below:[40]

$$log_{10} log_{10}(\mu + 0.7) = b_1 + b_2 log_{10} T \tag{3}$$

where μ is the viscosity of Peace River bitumen (Pa.s), T is the absolute temperature (^oK), and b_1 and b_2 values are 9.5235 and -3.5723, respectively.[40] Jin (1999) also developed the empirical

correlation between the viscosity of produced oil with butane solvent concentration and the correlation was:[41]

$$\mu(C_s) = 16609 C_s^{-2.12} \quad (4)$$

$$\mu(\omega_s) = 0.0094655 \omega_s^{-2.12} \quad (5)$$

where μ is the heavy oil or bitumen viscosity in poise, C_s is the volume fraction of butane in the heavy oil, and ω_s is the mass fraction of butane in the heavy oil.[41]

2.2.2 Diffusion and Gas EOR

Solvent gas diffusion in the heavy oil and bitumen is the primary reason for viscosity reduction, and hence it affects the production rate,[40] which makes diffusion phenomenon most important in gas EOR process. Diffusivity of injected gas solvent (i.e., air) can be determined by either experimental methods or by empirical correlations.[42] The experimental methods are classified under direct and indirect method. In the direct method, there would be a compositional analysis of heavy oil sample extracted at different times. Indirect methods are classified into two categories:

1. Based on property change such as volume, pressure, solute volatilization rate, the position of the gas-light interface, etc.
2. Diffusivity measurement from self-diffusion coefficients which are measured by Nuclear Magnetic Resonance Spectroscopy (NMR).[38]

Hayduk and Cheng (1971) gave a relationship between diffusivity and solvent viscosity:[43]

$$D = \alpha \mu^{-\beta} \quad (6)$$

where α and β are constants for each diffusive substance. The diffusivity of propane and butane in the Peace River bitumen were estimated using an indirect method by Das and Butler (1996).[40] They obtained the optimized constant values α and β in the Hayduk and Cheng (1971) correlation, for propane and butane to measure the diffusion coefficients. The empirical relationship for butane determined as:

$$D_s = 4.1300 \times 10^{-10} \mu^{-0.46} \quad (7)$$

Regarding to propane, the correlation was found as:

$$D_s = 1.3060 \times 10^{-9} \mu^{-0.46} \quad (8)$$

Upreti and Mehrotra (2000, 2002) estimated the diffusivity of carbon dioxide (CO_2), methane (CH_4), ethane (C_2H_6), and nitrogen (N_2) in Athabasca bitumen, in the range of 25°C to 90°C at 4 and 8 MPa. They used an indirect non-intrusive pressure decay experimental method to find the diffusivity of these gases as a function of gas concentration in bitumen. They developed the following correlation for average gas diffusivity:[12,19,42]

$$\ln D = d_o + d_1(T + 273.15) \quad (9)$$

They observed that diffusivity is a function of gas concentration in bitumen, and at a given gas concentration and pressure, the diffusivity increases with temperature. Lastly, their results indicate that gas diffusivity increases with pressure at a given temperature and gas concentration.

2.2.3 Dispersion and Gas EOR

Diffusion is a special case of dispersion where the fluid is stationary. Hence, the dispersion is a combined effect of diffusion and convective motion. At a macroscopic scale, this convective transport is Darcy's law describes a porous media. The variation in the reservoir properties results in a macroscopic dispersion. When the fluids are moving through porous media, the dispersion coefficient increases due to convective mixing and the dispersion may be higher than that due to diffusion alone.[44] Dispersion in porous media comprises concentration gradient in both longitudinal and transverse to the direction of solute-solvent flow.[19,42]

2.2.4 Permeability of the Reservoir and Gas EOR

In general, the reservoir volumes consist of sandstone which is considered as high porous and high permeable media. Porosity is a measurement of the fraction of bulk volume occupied by accessible pore space. Equation (10) shows the relationship between porosity and the volume fraction.

Permeability describes the fluid conductivity through porous media. Permeability is directly related to the porosity, and it depends on the porous connectivity and the size of the porous volumes. Permeability can be calculated by Darcy's law which was developed semi-empirically by Darcy in the 19th century for single phase flows and in the 20th century for multiphase flows.[45] The permeability coefficient depends on both material and the fluid properties. The greater the *K* value is, the higher will the flow rate be.[46] Darcy's law is expressed by:

$$\text{Porosity } (\emptyset) = \frac{\text{Volume of the void space } (V_V)}{\text{Total or bulk volume of the rock (or glass bead) } (V_T)} \quad (10)$$

$$Q = \frac{K\Delta P}{\eta \Delta L} A \tag{11}$$

where Q is the flow rate, K is the permeability coefficient, ΔP is the pressure difference, A is the cross-sectional area of the flow, η is the fluid viscosity, and ΔL is the flow length. The permeability is expressed in Darcy or millidarcy, and most of the oil reservoirs are in the range of ten to several hundreds of millidarcy.

2.3 Optimal Control and Enhanced Oil Recovery

An optimal control is a function that optimizes the performance of a system changing with time, space, or any other independent variable.[48] As a subject, optimal control is a superset of optimization that deals with the determination control functions for a given system that will optimize a particular performance criterion subject to constraints describing the system dynamics.

Optimal control has applications in many different fields, including aerospace, process control, and engineering. Only simple optimal control problems were solved before the 1950s. The revolution of the digital computers in the 1950s allowed the application of optimal control theory and methods to complex problems. Many applications of optimal control theory to enhanced oil recovery methods were developed.[48]

For example, optimal control was used to determine the concentration-dependent dispersion of propane in vapour extraction of heavy oil.[48] In more detail, the necessary conditions for the minimum were fundamentally derived, utilizing optimal control. A computational algorithm is formulated to calculate the propane dispersion function simultaneously with the propane-heavy oil

interfacial mass fraction. The results show that dispersion of propane is a unimodal function of its concentration in heavy oil, and lies in the range, 0.50000×10^{-5}–7.9930×10^{-5} m^2/s.

In a similar case, optimal control was utilized to enhance the oil production of vapour extraction using propane and butane injection pressure versus time as the control function. The results showed the optimal policy successfully lead to a 20-35% increase in the experimental oil production with propane and butane as pure solvents, and heavy oil of 14,500 mPa·s viscosity in lab scale reservoirs of 25 and 45 cm heights, and 204 Darcy permeability. Lastly, according to the results, the experimental oil production values from the optimal policy were within ± 5% of those predicted by the optimal control algorithm.[49]

Until now, many researchers have done different experiments, and mathematical modeling to have a better understanding of transport mechanism in gas EOR as well as recognize critical parameters to increase the heavy oil recovery performance (control functions such as dispersion coefficient and solvent injection pressure versus time).[48,49,60]

However, to the best of our knowledge, no one has applied optimal control policy by utilizing solvent interfacial temperature versus time as a control function to maximize oil production in gas EOR.

Chapter 3: Experimental Setup

The sections below describe experimental setups and procedures followed in this study to investigate the impacts of atmospheric air injection on heavy oil recovery. The first experimental setup is used for determination of the effects of permeability, air pressure, and air temperature on heavy oil recovery. The second setup is used for determining the concentration of air at the heavy oil interphase during air injection process. This setup is used to gather the data at different temperatures.

3.1 Air Injection Experimental Setup

Figure 2 shows the schematic of the experimental setup used to recover heavy oil from a cylindrical reservoir model by injecting air at different temperatures and pressures. This setup allows to generate heavy oil production data with constant and varying air temperature with time. The setup consists of a cylindrical pressure vessel with an internal diameter of 15 cm and height of 80 cm. A resistance temperature detector (Rugged Transition Joint Probe, Newport Electronics, CA, US) and a pressure transducer (Voltage Output Pressure Transducer, PX01C1-200G5T, Omega Inc., Canada) are provided to measure, respectively, the air temperature and pressure inside the vessel. Also, a digital thermometer (VWR traceable digital thermometer with recorder output, Mississauga, Ontario, Canada) is installed to record the interfacial temperature of the physical model.

Inside the vessel and suspended from a load cell (Miniature Load Cell Model 31, Honeywell Sensotec, OH, US) is a physical reservoir model (of 3 cm radius and 25 cm length), which is

brought into contact with air during an experiment. The load cell tracks the decrease in the mass of the physical model with time as the oil is produced. The live oil production was recorded online every 5 seconds with data acquisition system from the load cell, which exhibited reduction in the weight of the model. The physical models are prepared from Fort Kent heavy oil (supplied by Saskatchewan Research Council, Alberta, Canada) of viscosity 14,500 mPa.s at 20^{o}C and glass beads (BALLOTINI® Impact Beads, Potters Industries LLC, PA, US) packed together in a cylindrical stainless steel wire mesh. The models are homogeneous with a porosity around 0.38 and have different permeability values, namely, 40, 87, 204, and 427 Darcy.

A flow meter (In-line flow meters, FL46302, Omega Inc., QC, Canada) monitors the flow of air to the pressure vessel. To maintain a desired air pressure inside the pressure vessel at any time two pressure control valves (PV101-10V, Omega Inc., QC, Canada) are used, respectively, at the air entrance and the air exit. The air inside the pressure vessel is heated using a heating tape (Heat tape with the controller, HTWC 101, Omega Inc., QC, Canada) wrapped around the pressure vessel. The pressure vessel is covered with an aluminum wrap to minimize the heat loss to the surrounding. All instruments are connected via a data acquisition system to a computer and interfaced with LabView version 7.1 software. To be able to cool down the air temperature inside the vessel, cold water is circulated through a copper coil (40 inches long and with 0.25-inch tube diameter) wrapped around the vessel.

To collect the heavy oil recovered in an experiment, the pressure vessel has a small funnel connected directly to a calibrated collection tube. A load cell (Mid Range Precision Miniature Load Cell model 31, Honeywell Sensotec, Columbus, OH) is attached to the calibrated collection tube. A digital thermometer (VWR® Traceable® Digital Thermometer with Recorder Output, ON,

Canada) upstream of the collection tube helps to monitor and record the temperature in the pressure vessel. A collection tube sends the recovered oil to a viscometer (VISCO PRO 2000, Cambridge Viscosity, Inc., MA, US). The recovered oil is then directed to a stainless steel flash tank of 300 cm^3 capacity.

The tank is heated to 70^oC for 30 minutes with the help of the heating tape to separate the dissolved air from the oil. This air is then routed to two water columns in series, which are used to measure the amount of dissolved air in oil.

The columns are made of acrylic and have capacities $2.6000\times10^3 cm^3$ and $2.9000\times10^3 cm^3$, respectively. The first column is filled with water. The second column is calibrated and used to collect the water displaced from the first column when the air is separated. Table 2 shows the range of parameters used in this study. The temperature above 90^oC was avoided to preclude any hydrocarbon oxidation (please see Section 5.1.5). The range was selected based on the recent research on gas EOR.[48-50]

Table 2: Parameters range used in this study

parameter	**range**
temperature	25-90^oC
pressure	0.169-0.514 MPa absolute
permeability	40-427 Darcy

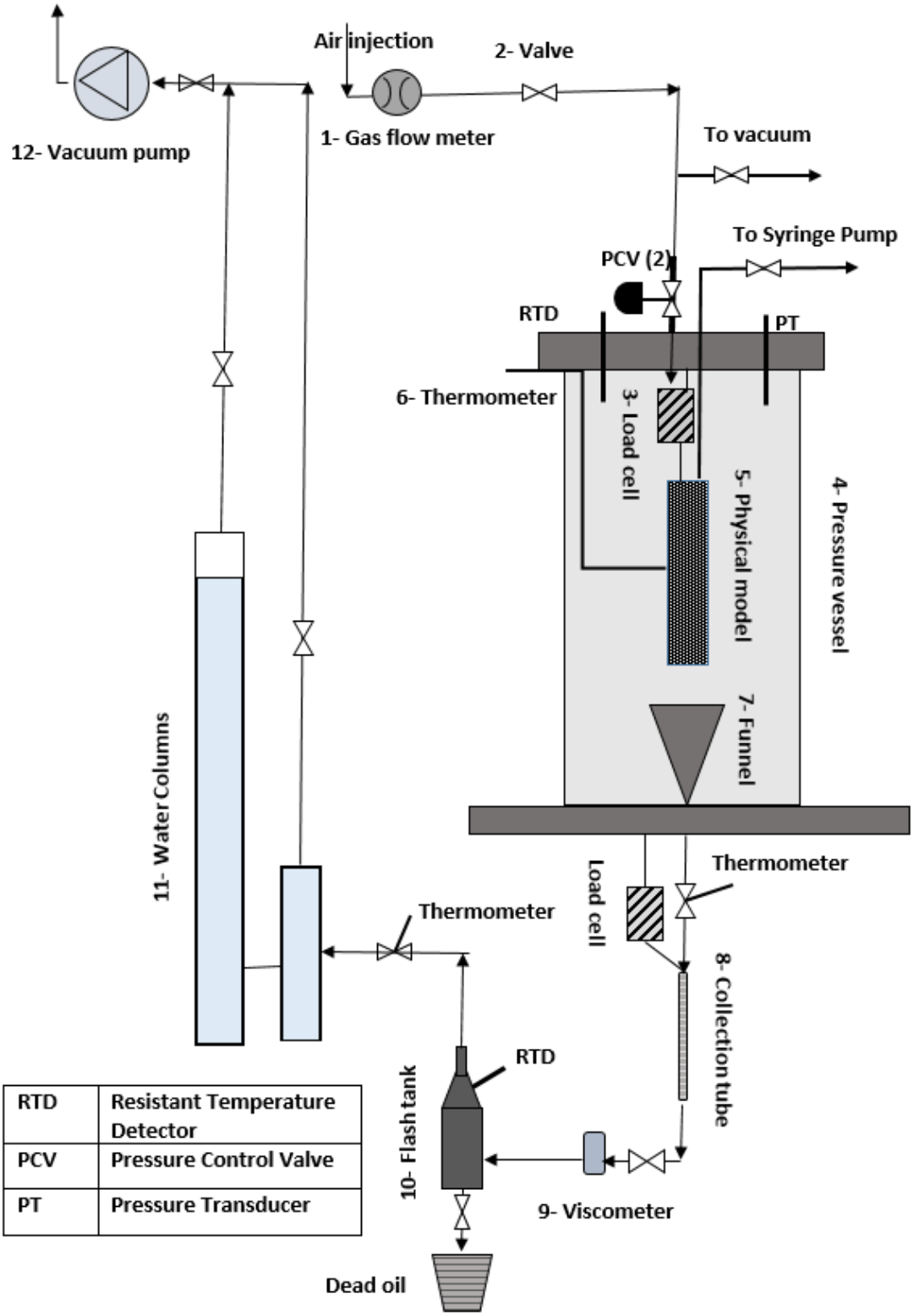

Figure 2: Schematic diagram of the experimental setup. The list of equipment in order are: 1-gas flow meter, 2-valve, 3-load cell, 4- pressure valve, 5- physical model, 6- thermometer, 7- funnel, 8-collection tube, 9- viscometer, 10- flash tank, and 11-water columns

3.2 Experimental Procedure

Before starting each experiment, the air was purged from the pressure vessel by applying vacuum close to 0.1 MPa (absolute) using a vacuum pump. Then the atmospheric air was injected into the pressure vessel at different pressures (0.169, 0.286, 0.403 and 0.514 MPa absolute) and temperatures (25-90^{o}C).

The run time for each experiment was 430 minutes (a little over seven hours). At the start of each experiment, the initial air flow rate to the pressure vessel was set at 2.5 L/min and then gradually decreased to 0.13 L/min.

The penetration of air into the physical model eventually led to the production of "live oil," which drained out from the bottom of the model by gravity and accumulated in the collection tube. After a certain amount of live oil had been collected in the collection tube, the live oil was directed through the viscometer to the flash separation tank preheated to 70^{o}C for about 30 minutes to separate the air dissolved in the oil.

As the separated air moved from the flash tank to the first water column, the water level of the second column started to rise. The increase in the level was recorded. The valve on the top of the first column was then opened to release the air to the fume hood. The air-free "dead oil" from the flash tank was weighed and recorded. At the end of an experiment, the air flow was shut, and the pressure vessel was vented to atmosphere. A photo of the experimental setup is shown in Figure 3.

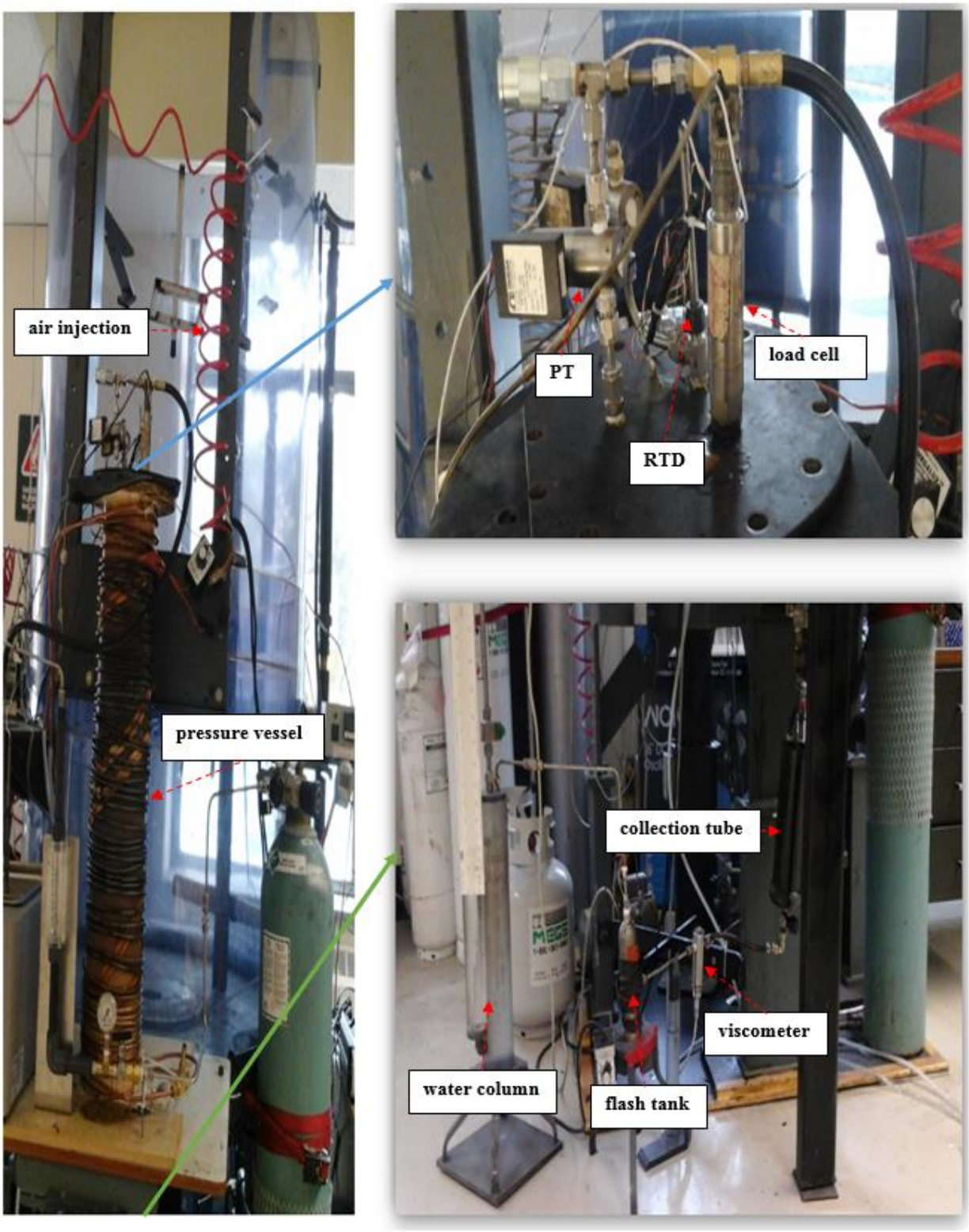

Figure 3: Picture of Air Injection Experimental Set

3.3 Physical Model Preparation

The physical model was made of heavy oil of a viscosity of 14,500 mPa.s at 20^{o}C. Oil-saturated porous medium with glass beads of known permeability was packed in a cylindrical wire mesh of 3 cm radius and 25 cm length. The oil packing was prepared using a known mass of heavy oil, 602.86 g, which was placed in a temperature-controlled heater. The heavy oil was heated for 30 minutes at 70^{o}C, for sufficient reduction in oil viscosity to promote glass beads mixing. Glass beads were gradually added to the heated heavy oil to ensure proper mixing without trapping air bubbles.

After heavy oil was thoroughly mixed with the glass beads, the saturated mixture was packed into the cylindrical wire mesh physical model. The saturated mixture was slowly poured inside the cylindrical wire mesh as a thin layer, and allowed to settle under gravity. Then another layer oil was added. This process was repeatedly to fill the wire mesh. This method of preparing oil-saturated beads ensured that the medium was homogenous, and did not trap any air. After the entire mesh was packed, it was weighed and left at room temperature for one day to reach thermal equilibrium (at about 23^{o}C room temperature) prior to the experiments.

Porosity is a measurement of the fraction of bulk volume occupied by accessible pore space. The porosity of the packing of different glass beads was measured by the imbibition or saturation method. A cylindrical model was filled with the glass beads and weighed. The cylindrical model was flooded with water from the bottom until it is saturated. The cylindrical model filled with water was again weighed. The porosity of glass beads in the cylindrical model was determined from the amount of water in the cylindrical model. Table 3 lists the properties of the glass beads

used for the physical model preparation. Knowing the density of the glass beads and density of the heavy oil, the porosity of the physical model was measured to be 0.38.

Table 3: Properties of glass beads used in this study

size range (mm)	**porosity**	**permeability** (Darcy)
0.84000-0.59400	0.38500	427
0.59400-0.41900	0.38000	204
0.41900-0.24800	0.37800	87
0.24800-0.21000	0.37600	40

3.3.1 Permeability of Physical Model

We prepared physical models of different permeabilities to investigate the impact of permeability on heavy oil recovery. The procedure of permeability measurement was adopted by El-Haj (2007).[71] To measure the permeability of the porous medium made of heavy oil and glass beads, a vertical acrylic cylinder of 6 cm internal diameter and 21 cm height was used. The cylinder had two ports, one at the air entrance and the other for the air exit. A differential pressure transducer (Differential Pressure Transducer, PX409, Omega Inc., QC, Canada) was used to connect the inlet and outlet ports to measure the pressure difference across the media as air passed through the porous medium. The flow rate of air at the outlet was measured by a flow meter (In-line flow meters, FL46302, Omega Inc., QC, Canada). The permeability of the porous medium is given by[49]

$$K = \frac{Q\mu\Delta x}{A\Delta P} \times 1.01325 \times 10^{12} \quad (12)$$

where Q is the volumetric fluid flow rate through the media, A is the cross-section area of fluid flow through the medium, μ is the dynamic viscosity of the fluid, and ΔP is the pressure difference across the medium of thickness Δx. The values of these parameters are listed in Table 4 for glass beads of size in the range 0.248-0.210 mm. With these values, Equation (12) yields the permeability of 40 Darcy.

Table 4: Parameters for calculation of permeability for glass bead size 0.248-0.210 mm

parameter	**value**
Q (m^3/s)	1.66001×10^{-5}
μ at 20°C (Pa.s)	1.8401×10^{-5}
Δx (m)	0.21000
A (m^2)	2.82000×10^{-3}
ΔP (Pa)	577.00

3.4 Solvent Gas Solubility and Live Oil Density

As previously mentioned, the collected live oil was delivered to stainless steel flash separation tank (300 cm^3) to separate the solvent gas from oil by heating the flash tank to 70°C. After a particular time, the amounts of absorbed gas transfer to gas measuring columns initially filled with water, and the residual oil (deal oil) is collected and measured.

The mass of the solvent gas was determined as follows. A known amount of live oil was transferred to the flash tank and heated at maintained temperature of 70°C to ensure proper flashing of the gas.

The flashed gas was delivered to the first water column. Wherein, the water was displaced resulting in a rise of the water level in the second water column. After 10 minutes the differential pressure reading approached zero with no more displacement in the second water column. The displaced volume of water determined the gas volume. The valve on the top of the first water column was opened to vent the gas, and the net amount of dead oil was collected by opening the valve at the bottom of the flash tank. By knowing the amount of air dissolved in oil, the solvent gas-free oil (dead oil) weight, and the volume of the live oil, the solubility of the solvent gas was determined as well as the live oil density using the following formulas:

$$\omega = \frac{m_{gas}}{m_{gas}+m_{oil}} \tag{13}$$

$$\rho = \frac{m_{gas}+m_{oil}}{V_{Live\ oil}} \tag{14}$$

where ω is the dissolved mass fraction of the solvent gas, m_{gas} is the mass of liberate solvent gas, m_{oil} is the mass of the dead oil, ρ is the live oil density, and $V_{\text{Live oil}}$ is the volume of live oil. A sample of air solubility and live oil density calculations is presented in Appendix B.

3.5 Interfacial Solvent Concentration Setup

This experimental setup was designed to determine the air interfacial concentration at different pressures and temperatures. This innovative part consists of a high-pressure vessel, syringe pump, water bath, data acquisition system, and capillary tubes for the sample oil collection. It is important to mention that the purpose of these data is to derive the empirical correlation between the interfacial mass fraction of air (ω_{int}) and the interfacial temperature of air (T_{int}). This correlation furnishes the boundary condition of the mass transfer model.

3.5.1 Experimental Procedure and Interfacial Solvent Concentration

Figure 4 shows the experimental setup for determination of atmospheric air concentration at the heavy oil interfacial. Before starting lab experiment, the air was purged from the pressure vessel by applying vacuum close to 0.1 MPa (absolute) using a vacuum pump. Then, the pressure vessel was filled with 25 g of heavy oil of viscosity 14,500 mPa.s. The filling up the pressure vessel was done slowly to avoid entrapment of air within heavy oil layers. After thoroughly sealing the pressure vessel it was placed in a water bath. The objective of the water bath was to maintain the temperature at a set temperature. The top end of the vessel was connected to the syringe pump and the capillary tube that was used to take the oil sample from the top most layers, very close to the heavy oil surface (about one millimeter) into a sealed collection tube. The run time for each test was 430 minutes (a little over seven hours).

At the start of each experiment, the initial air flow rate to the pressure vessel was set at 0.13 L/min. We have also installed a digital thermometer (VWR Traceable Digital Thermometer with recorder output, Mississauga, Ontario, Canada) to record the interfacial temperature of the heavy oil. After collecting the live oil inside a sealed sample tube, the sample was weighted. Then the tube was open to atmosphere and heated to around 70^{o}C to release the dissolved and residual air in the oil. After flushing the solvent gas out the tube the dead oil was weighed. From the mass balance, air mass fraction in the oil was calculated. The experiments were performed at different injection pressures and temperatures. The solvent concentration thus obtained is the interfacial concentration used in this study.

Table 5 lists the interfacial air mass fraction at different temperatures at the constant pressure of 0.514 MPa.

Table 5: Temperature versus interfacial concentration for air at pressure of 0.514 MPa

temperature (°C)	air mass fraction (ω_{int})
25	0.015601
50	0.061102
75	0.16603
90	0.46301

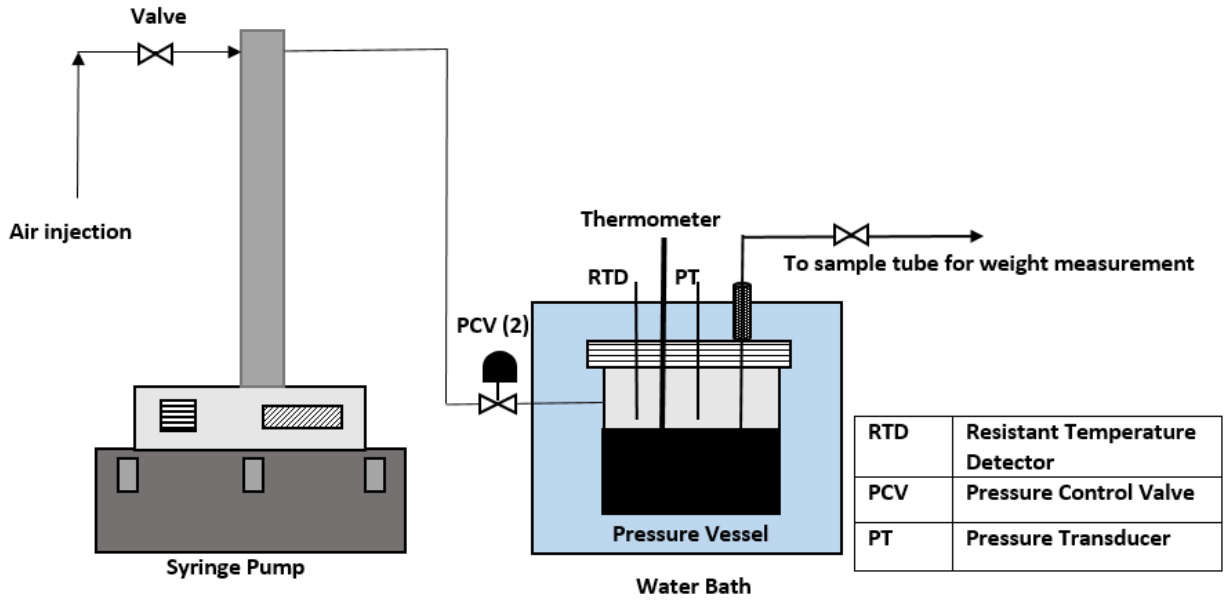

Figure 4: Schematic of solvent-heavy oil system for the measurement of interfacial solvent concentration

3.6 Experimental Results Repeatability

The accuracy of this study was based on data collected from load cell weight change during the experiments. Therefore, it was essential to calibrate the load cell at the start of each experiment and compare its readings with scalar at the beginning and end of each experiment.

Also, the second load cell was used to have a better control of heavy oil recovery during each experiment. Lastly, the relative errors between the oil recovery from the repeated experiments were found to be in the range of 1.3-1.5%.

3.7 Laboratory Equipment

A list of the instrumentation and laboratory equipment used in this study is shown in Table 6.

Table 6: List of equipment used in this study

instrument	information	range	accuracy (Error %)
Resistance Temperature Detector	Rugged transition joint probe, Newport Electronics, Santa Ana, CA	0−230°C 0−2500 (psig)	0.1% (Full scale)
Pressure Transducer	Voltage output pressure transducer, PX01C1-200G5T, Omega, Inc., Laval, Quebec, Canada	-46−121°C 0−200 (psig)	0.05%
Load Cell	Mid Range Precision Miniature Load Cell model 31, Honeywell Sensotec, Columbus, OH, USA	1000 g to 1000 lb -53–121°C	0.15% (of full load)
Flow Meter	In-line flow meters, FL46302, Omega, Inc., Laval, Quebec, Canada	-10–65°C 150 psig (max)	5%
Pressure Control Valve	PV101-10V, Omega Inc., Laval, Quebec, Canada	-10–50°C 200 psig (max)	0.5%
Heating Tape	Heat tape with the controller, HTWC 101, Omega, Inc., Laval, Quebec, Canada	232 °C (max)	5%
Digital thermometer	VWR traceable digital thermometer with recorder output, Mississauga, Ontario, Canada	−50–1300°C	0.3%
Viscometer	VISCO PRO 2000, Cambridge Viscosity, Inc., Medford, MA, USA	0.2–20,000 cP	1.0% (of full scale)
Differential Pressure Transducer	differential pressure transducer, PX409, Omega, Inc., Laval, Quebec, Canada	-45-121°C 0−200 (psig)	0.08%
Gas Chromatography Mass Spectrometry with a thermal conductivity detector	Perkin Elmer Autosystem XL GCMS/TCD, Woodbridge, Ontario, Canada	1.0-1200 u (amu)	±0.1 m/z mass accuracy

Chapter 4: Optimal Control of Air Injection

This chapter presents the optimal control of air injection gas EOR to maximize heavy oil recovery using air interfacial temperature versus time as a control function. For this purpose, the necessary conditions for maximum heavy oil recovery are derived based on detailed heat and mass transfer model of the gas EOR experiments carried out in this study. The model enables the determination of oil production, and the change in the height of the physical model with time. A computational algorithm is developed to compute the optimal policy.

4.1 Determination of Optimal Control

Optimal control principles help us to determine the policies that optimize some performance criterion, subject to the constraints imposed by the physical nature of the underlying process. The principles are based on the classical calculus of variations. Even for modest processes, the application of optimal control principles generates highly nonlinear differential equations that require the use of numerical techniques for the solution.[48]

In this study, we use the interfacial air temperature versus time as the control function. The determination of optimal control is based on the mathematical model of the experimental process. It is important to note that the model comprising of mass and heat transfer balances is a set of highly non-linear partial differential equations, and poses a moving boundary problem. Its analytical solution is not possible. Therefore, the optimal control problem is solved numerically after deriving and satisfying the necessary conditions for optimal control.[48] A computational algorithm is implemented in C++ language is used to solve the optimal control problem.

4.2 Mathematical Model Formulation

As mentioned earlier, we develop a detailed mass and heat transfer models of the air injection process for heavy oil recovery based on previous studies. The assimilation of heat transfer is done for the first time in this work. The details are as follows.

4.2.1 Mass Transfer Model

A mathematical model below is to describe the mass transfer process in the experiments mentioned above. The assumptions of the model developed are as follows:

1. The flow of the live oil along the vertical direction is governed by Darcy's law in the porous medium of the lab-scale heavy oil reservoirs used in this work

   Justification: The live oil flow is a creeping flow since Reynold's numbers (Re) calculated for the live oil flow are less than unity.

2. The diffusion of the air takes place along the radial direction only. diffusion in the vertical direction is neglected.

   Justification: Diffusion occurs in the radial direction over a large surface area along the circumference of the cylindrical model. In contrast, diffusion in the vertical direction occurs over a much smaller area at the top of the cylindrical model. Moreover, convection is dominant in the vertical direction.

3. The porous medium has uniform porosity and permeability

   Justification: The oil was mixed uniformly with glass beads and packed in a cylindrical stainless steel wire mesh. Thus, each model has a uniform permeability, and no heterogeneities exist (please see Section 3.3).

4. The density of the live oil is assumed constant.

Justification: A sensitivity analysis (see Section 5.2.7) shows that the small variation (± 5%) in the live oil density (ρ), the change in maximum objective functional in comparison to base value at 204 Darcy permeability and air pressure of 0.514 MPa (absolute) is insignificant.

5. There were no chemical reactions as the absorption of the solvent gas in heavy oil is purely a physical phenomenon. (please see Section 5.1.5)

The unsteady state mass balance for the air in a cylindrical differential element is given by:

$$\begin{pmatrix}\text{Accumulation of the}\\ \text{solvent mass over a}\\ \text{finite time interval } \Delta t\end{pmatrix} = \begin{pmatrix}\text{Rate of the solvent}\\ \text{mass input along}\\ r \text{ and } z\\ \text{direction}\end{pmatrix} - \begin{pmatrix}\text{Rate of the solvent}\\ \text{mass output along}\\ \text{r and z direction}\end{pmatrix} \quad (15)$$

As per our assumption, the penetration of the air takes along r-direction. The transport of the air along r-direction is given by Fick's first law:

$$\begin{pmatrix}\text{Rate of the solvent}\\ \text{mass input along}\\ r\\ \text{direction}\end{pmatrix} - \begin{pmatrix}\text{Rate of the solvent}\\ \text{mass output along}\\ r\\ \text{direction}\end{pmatrix} = (J_g S)_r - (J_g S)_{r+\Delta r} \quad (16)$$

where J_g is the mass flux of the air, and is given by:

$$J_g = -\rho D \frac{\partial \omega}{\partial r} \quad (17)$$

The mass transfer of the live oil along z-direction is governed by the Darcy flow. *D* is undermined air dispersion in the porous media which is a function of both concentration and temperature. The dispersion of the solvent gas along z-direction is negligible while bulk is moving:

$$\begin{pmatrix}\text{Rate of the solvent}\\ \text{mass input along}\\ \text{z}\\ \text{direction}\end{pmatrix}-\begin{pmatrix}\text{Rate of the solvent}\\ \text{mass output along}\\ \text{z}\\ \text{direction}\end{pmatrix}=(vA\rho\omega)_z-(vA\rho\omega)_{z+\Delta z} \quad (18)$$

Substituting Equations (16) and (18) into (15) results in the following unsteady state mass balance for the solvent gas equation

$$\frac{\delta}{\delta t}(V\emptyset\rho\omega)=\left[(vA\rho\omega)_z+\left(J_gS\right)_r\right]-\left[(vA\rho\omega)_{z+\Delta z}+\left(J_gS\right)_{r+\Delta r}\right] \quad (19)$$

In the equation above, $\emptyset$ is the medium porosity, *V* is the finite differential volume, *S* is the finite differential surface area along r-direction, and A is the finite differential cross-sectional area along z-direction are given by:

$$V=2\pi r\Delta r\Delta z \quad (20)$$

$$S=2\pi r\Delta z \quad (21)$$

$$A=2\pi r\Delta r \quad (22)$$

By substituting the Equations (17), (20), (21), and (22) into Equation (19) yields the following unsteady state partial differential equation.:

$$\frac{\partial\omega}{\partial t}=\frac{\partial D}{\partial\omega}(\frac{\partial\omega}{\partial r})^2+D\left[\frac{1}{r}\frac{\partial\omega}{\partial r}+\frac{\partial^2\omega}{\partial r^2}\right]-\frac{1}{\emptyset}\left[\omega\frac{\partial v}{\partial\omega}\cdot\frac{\partial\omega}{\partial z}+v\frac{\partial\omega}{\partial z}\right] \quad (23)$$

In the above equation, ω is the mass fraction of air and *v* is the Darcy velocity of the live oil within porous media along z-direction given by:

$$v = \frac{K_r K \rho g}{\mu} \tag{24}$$

where μ is the viscosity of live oil, ρ is the density of the live oil, K_r is the relative permeability, K is the medium permeability and g is gravity. Since the porous medium is saturated only with heavy oil, the effective permeability equals the absolute permeability, and then the relative permeability is equal to unity.

The following is the correlation used for μ:[49]

$$\mu = \mu_o \omega^{-2} \tag{25}$$

where μ_o is the live oil viscosity coefficient, calculated from experimentally obtained live oil viscosity and solvent gas solubility mass fraction.

By putting the above expressions in Equation (23), the mass balance equation over finite element can be written as:

$$\frac{\partial \omega}{\partial t} = \left(\frac{\partial D}{\partial \omega}\right).\left(\frac{\partial \omega}{\partial r}\right)^2 + \frac{D}{r}\left(\frac{\partial \omega}{\partial r}\right) + D\left(\frac{\partial^2 \omega}{\partial r^2}\right) - 3\alpha \frac{\omega^2}{\phi}\left(\frac{\partial \omega}{\partial z}\right) \tag{26}$$

where $\alpha = \frac{K K_r \rho g}{\mu_o}$

Initial and Boundary Conditions for the Mass Transfer

Initially, there was no air inside the packing. However, at all time, its surface has the air concentration equal to its equilibrium saturation concentration under prevailing temperature and pressure. There is no production of live oil at the beginning, so the initial height of the physical model of the heavy oil sample is Z_o.

Thus the initial conditions at t = 0 are:

$$\omega = \begin{cases} 0, \ \forall 0 < z < Z_o, \forall\ 0 \le r < R \\ \omega_{int}(0), \ at\ z \in \{0, \ Z_0\} \ \forall 0 \le r < R; \text{and at } r = R \ and \ 0 \le z \le Z_o \end{cases} \quad (27)$$

$$Z=Z_0 \ \forall\ 0 \le r \le R$$

It is important to note that *r* is the radius measured radially outward from the center vertical axis of the physical model and *z* is the vertical distance measured upward from the bottom of the model as it shown in Figure 5.

Furthermore, the boundary conditions at $t \geq 0$ are:

$$\omega = \omega_{\text{int}}(t) \text{ at } r = R \ \ \forall 0 \le z \le Z(r,t) \text{ and } \ z \in \{0, Z(r,t)\} \forall\ 0 \le r < R \quad (28)$$

where *Z(r,t)* is the height of the heavy oil in the physical model at a given *r* and *t*. Furthermore, due to symmetric of the physical model, we have the following:

$$\frac{\partial \omega}{\partial r} = 0 \ \forall 0 \le z \le Z(0,t) \text{ and } r = 0 \quad (29)$$

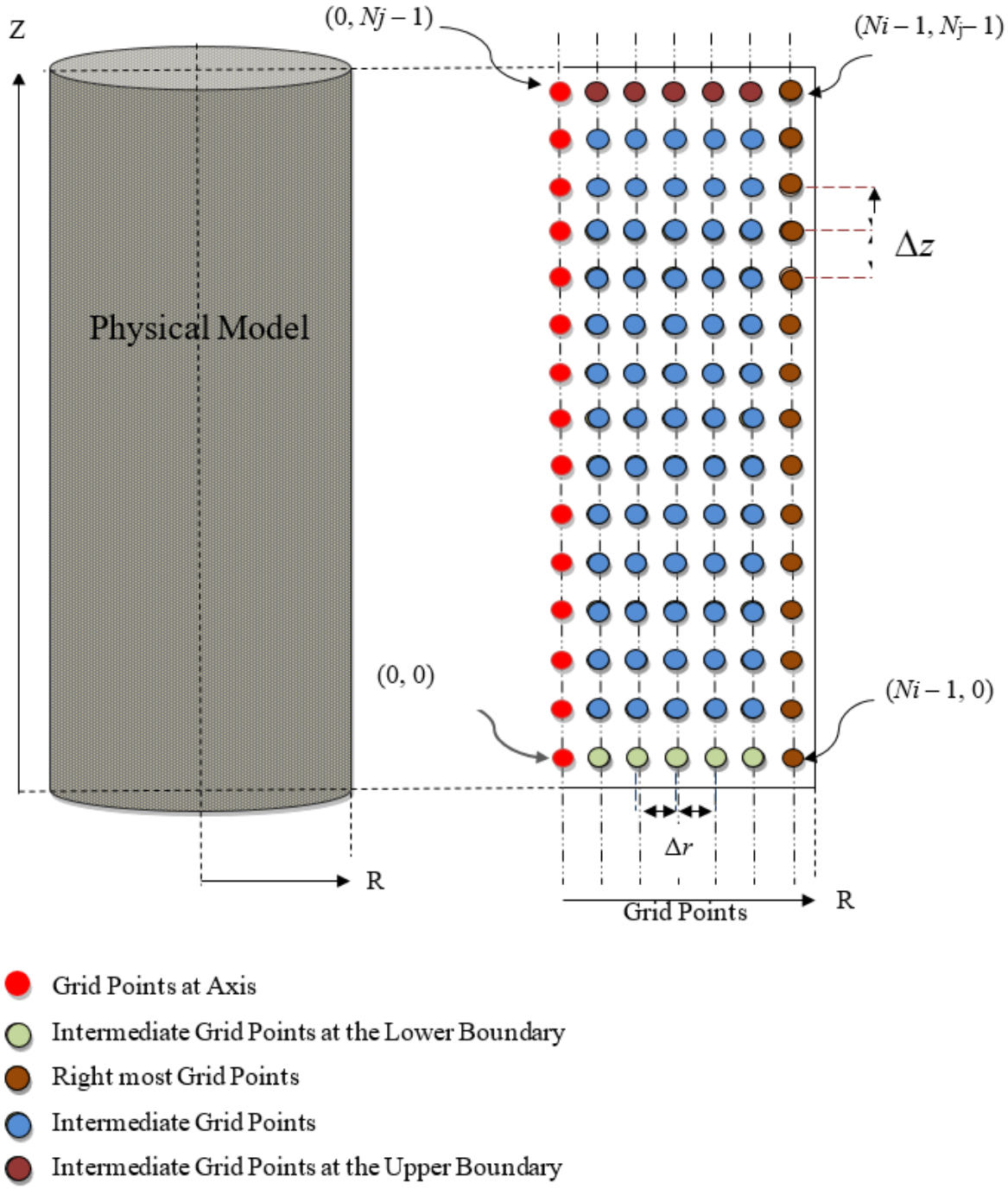

Figure 5: Cylindrical Model and Node Distribution

4.2.2 Change in Height at Any Time

The production of oil reduces the height *Z(t,r)* of the bitumen in the packed medium. The change in the height with time at any radial location is given by the negative of Darcy velocity at the bottom of the physical model as:

$$\frac{\partial Z}{\partial t} = \frac{-v_o(t,r,0)}{\emptyset} = -\frac{K_r K \rho g}{\mu \emptyset} \tag{30}$$

where $v_o(t,r,0)$ is the Darcy velocity of the produced oil at a given r, and averaged over the differential volume, 2πrdrdz at the bottom, that is, at *Z*=0. It is important to note that The solvent–heavy oil interface at the top of the physical model moves down and the height of the bitumen, *Z(t,r)*, decreases with time due to live oil drainage. Thus, we have a moving boundary problem, which is described by Equation (30).

4.2.3 Calculation Mass of Live Oil

The cumulative mass of produced live oil at any time was calculated from multiplying differential volume with live oil density and medium porosity. For a calculated change in height mass of live oil produced was obtained by integrating the multiple from 0 to *R* as:

$$m_{cal} = 2\pi\rho\emptyset \int_0^R (Z_o - Z(r,t)) r dr \tag{31}$$

4.2.4 Heat Transfer Model

The mathematical below is for the heat transfer process for the porous media in the experiments as mentioned earlier. The assumptions of the model developed are as follows:

1. The flow of the live oil along the vertical direction is governed by Darcy's law in a porous medium; Negligible radioactive effects.

Justification: The live oil flow is a creeping flow since Reynold's numbers (Re) calculated for the live oil flow are less than unity.

2. The porous medium has uniform porosity and permeability.

   Justification: As previously mentioned, the oil was mixed uniformly with glass beads and packed in a cylindrical stainless steel wire mesh. Thus, each model has a uniform permeability, and no heterogeneities exist.

3. The density of the live oil is assumed constant.

   Justification: As previously mentioned, sensitivity analysis shows that the small variation (± 5%) in the live oil density (ρ), the change in the maximum objective functional in comparison to base value at 204 Darcy permeability, and air pressure of 0.514 MPa (absolute) is insignificant.

4. There are no chemical reactions in the process (please see Section 5.1.5).

5. The specific heat capacity (C_p) and the thermal conductivity coefficient (k) are assumed constant.

   Justification: Sensitivity analyses (see Section 5.2.7) show that the small variation (± 5%) in the specific heat capacity (C_p) and the thermal conductivity coefficient (k), the percentage changes in maximum objective functional in comparison to base value at 204 Darcy permeability and air pressure of 0.514 MPa (absolute) are insignificant.

Similar to the mass transfer model, the heat transfer model of the lab-scale reservoir involving heat conduction is given by Equation (32)

$$\emptyset\left(\rho C_p\right)\frac{\partial T}{\partial t} + \rho C_p\left(v\frac{\partial T}{\partial z}\right) = \emptyset k\left[\frac{1}{r}\frac{\partial}{\partial r}\left(r\frac{\partial T}{\partial r}\right) + \frac{\partial^2 T}{\partial z^2}\right] \quad (32)$$

where C_p is the specific heat capacity and k is the thermal conductivity coefficient.

Simplification the equation above, we finally obtain:

$$\frac{\partial T}{\partial t} = \left(\frac{k}{\rho C_p}\right)\left[\frac{1}{r}\frac{\partial}{\partial r}\left(r\frac{\partial T}{\partial r}\right) + \frac{\partial^2 T}{\partial z^2}\right] - \frac{v}{\emptyset}\frac{\partial T}{\partial z} \tag{33}$$

or

$$\frac{\partial T}{\partial t} = \gamma\left[\frac{1}{r}\frac{\partial T}{\partial r} + \frac{\partial^2 T}{\partial r^2}\right] + \gamma\left[\frac{\partial^2 T}{\partial z^2}\right] - \alpha\frac{\omega^2}{\emptyset}\left[\frac{\partial T}{\partial z}\right] \tag{34}$$

by letting $\gamma = \frac{k}{\rho C_p}$

Initial and Boundary Conditions for the Heat Transfer

Similar to mass transfer, we are required to apply initial and boundary conditions for heat transfer equation. The initial conditions at *t*= 0 are as follows:

$$T = \begin{cases} 0, \ \forall 0 < z < Z_o, \forall\ 0 \le r < R \\ T_{\text{int}}, \ at\ z \in \{0,\ Z_0\}\ \ \forall 0 \le r < R; \text{and at } r = R \text{ and } 0 \le z \le Z_o \end{cases} \tag{35}$$

In more detail, at the initial time, there is no air inside the packing. Although, the physical model surface has the interfacial temperature equal to its equilibrium interfacial temperature under prevailing temperature and pressure. Lastly, due to the fact that there is no production of live oil at the beginning. The initial height of the physical model of the heavy oil sample is Z_o.

The boundary conditions at t $\geq$ 0 are

$$T = T_{\text{int}}\ at\ r = R\ \ \forall 0 \le z \le Z(r,t)\ and\ \ z \in \{0, Z(r,t)\}\ \forall\ 0 \le r < R \tag{36}$$

Furthermore, due to the symmetry of the physical model:

$$\frac{\partial T}{\partial r} = 0\ \ \ \forall 0 \le z \le Z(0,t)\ and\ r = 0 \tag{37}$$

In the next step, an optimal control problem will be formulated to determine the desired interfacial temperature versus time [$T_{int}(t)$] function that minimizes the difference between the model-predicted and the experimentally measured values of the cumulative live oil produced.

The role of interfacial temperature is significant in gas EOR, particularly since air mass fraction dissolve inside heavy oil media is a strong function of temperature [$\omega_{\mathrm{int}} = \omega_{\mathrm{int}}(T_{\mathrm{int}})$].

4.3 Formulation of Optimal Control Problem

The objective of this problem is to maximize the heavy oil recovery using atmospheric air by using the interfacial temperature versus time as the control function. The latter translates to T_{int} versus time in the optimal control problem as follows

Mathematically, the problem is to maximize objective functional *I* which is written as:

$$I = \int_0^{t_f} m\, dt \tag{38}$$

where, *m* is the cumulative mass of produced live oil and t_f is the duration of the oil recovery experiment. With the help of Equation (31), the objective functional becomes;

$$I = \beta \int_0^{t_f} \int_0^{R} (Z_o - Z(r,t)) r dr dt \tag{39}$$

where $\beta = 2\pi\rho\emptyset$.

The maximum of *I* is subject to Equations (26), (30), and (34), which can be expressed as, respectively:

$$G_1(t,r,z) = -\frac{\partial T}{\partial t} + f_1 = 0 \tag{40}$$

where

$$f_1 = \gamma\left[\frac{1}{r}\frac{\partial T}{\partial r} + \frac{\partial^2 T}{\partial r^2}\right] + \gamma\left[\frac{\partial^2 T}{\partial z^2}\right] - \alpha\frac{\omega^2}{\emptyset}\left[\frac{\partial T}{\partial z}\right] \tag{41}$$

Furthermore, we have:

$$G_2(t,r,z) = -\frac{\partial \omega}{\partial t} + f_2 = 0 \tag{42}$$

where

$$f_2 = \left(\frac{\partial D}{\partial \omega}\right).\left(\frac{\partial \omega}{\partial r}\right)^2 + \frac{D}{r}\left(\frac{\partial \omega}{\partial r}\right) + D\left(\frac{\partial^2 \omega}{\partial r^2}\right) - 3\alpha\frac{\omega^2}{\phi}\left(\frac{\partial \omega}{\partial z}\right) \tag{43}$$

Lastly, we have:

$$H(t,r) = -\frac{\partial Z}{\partial t} + f_3 = 0 \tag{44}$$

where,

$$f_3 = \frac{-v(t,r,0)}{\emptyset} = \frac{-\alpha[\omega(t,r,0)]^2}{\emptyset} \tag{45}$$

The above equation was determined by substituting Equation (25) into Equation (24) for viscosity, and also knowing that $\alpha = \frac{KK_r\rho g}{\mu_o}$.

Equations (40), (42), and (44) are the constraints for the objective functional *I*. These constraints are highly non-linear partial differential equations. Therefore, to solve the optimal control problem, three unterminated costate variables $\lambda_1(t,r,z), \lambda_2(t,r,z),$ and $\lambda_3(t,r)$ are introduced into Equation (40) to obtain the following augmented objective functional:

$$J = I + \int_0^{t_f}\int_0^R\int_0^Z \lambda_1(t,r,z)G_1(t,r,z)dzdrdt + \int_0^{t_f}\int_0^R\int_0^Z \lambda_2(t,r,z)G_2(t,r,z)dzdrdt +$$

$$\int_0^{t_f}\int_0^R \lambda_3(t,r)\, H(t,r)drdt \tag{46}$$

It is important to note that in the equation above, Lagrange multipliers (sometimes called adjoint or costate variables) are used. Costate variables are used to ensure that constraints given by the equations of the simulation model are satisfied. The costate variables $\lambda_1(t,r,z), \lambda_2(t,r,z), \text{and } \lambda_3(t,r)$ are introduced to form the augmented functional by adjoining the constraining relations to *I*. Note that for any $\lambda_1, \lambda_2, \text{and } \lambda_3$, *J* = *I* if the constraints are satisfied.

The Lagrange multiplier corresponding to the heat transfer model (i.e., the constraint defined by the partial differential equation for the change in temperature) is the change in the augmented objective functional due to the relaxation in the constraint.[47] Other Lagrange multipliers can be similarly interpreted.

By substituting Equations (39), (40), (42), and (44) into Equation (46), we get:

$$J = \beta \int_0^{t_f}\int_0^R (Z_o - Z)rdrdt + \int_0^{t_f}\int_0^R\int_0^Z \lambda_1 \left[-\frac{\partial T}{\partial t} + \gamma\left[\frac{1}{r}\frac{\partial T}{\partial r} + \frac{\partial^2 T}{\partial r^2}\right] + \gamma\left[\frac{\partial^2 T}{\partial z^2}\right] -\right.$$

$$\left.\alpha\frac{\omega^2}{\emptyset}\left[\frac{\partial T}{\partial z}\right]\right] dzdrdt + \int_0^{t_f}\int_0^R\int_0^Z \lambda_2\left[-\frac{\partial \omega}{\partial t} + \left(\frac{\partial D}{\partial \omega}\right).\left(\frac{\partial \omega}{\partial r}\right)^2 + \frac{D}{r}\left(\frac{\partial \omega}{\partial r}\right) + D\left(\frac{\partial^2 \omega}{\partial r^2}\right) -\right.$$

$$\left.3\alpha\frac{\omega^2}{\phi}\left(\frac{\partial \omega}{\partial z}\right)\right] dzdrdt + \int_0^{t_f}\int_0^R \lambda_3\left[-\frac{\partial Z}{\partial t} + f_3\right] drdt \tag{47}$$

where $\lambda_1(t,r,z), \lambda_2(t,r,z), and\ \lambda_3(t,r)$ are the costate variables. The maximum of *I* subjected to constraints is equivalent to the maximization of *J*.

4.4 Necessary Conditions for the Optimal Control

The necessary conditions for the optimum of J stem from $\delta J = 0$. Therefore, we can proceed it by deriving the expression for δJ as follows:

$$\delta J = \delta I + \int_0^{t_f}\int_0^R\int_0^Z (G_1\delta\lambda_1 + \lambda_1\delta G_1)dzdrdt + \int_0^{t_f}\int_0^R\int_0^Z (G_2\delta\lambda_2 + \lambda_2\delta G_2)dzdrdt +$$

$$\int_0^{t_f}\int_0^R (H\delta\lambda_3 + \lambda_2\delta H)\, drdt \tag{48}$$

By expansion of δG_1, δG_2, and δH in the Equation above, it leads to:

$$\delta J = -\beta\int_0^{t_f}\int_0^R r\delta Z drdt - \int_0^{t_f}\int_0^R\int_0^Z \lambda_1\frac{\partial(\delta T)}{\partial t}dzdrdt + \int_0^{t_f}\int_0^R\int_0^Z \lambda_1\frac{\partial(f_1)}{\partial T}\delta T dzdrdt +$$

$$\int_0^{t_f}\int_0^R\int_0^Z \lambda_1\frac{\partial(f_1)}{\partial T_r}\delta T_r dzdrdt + \int_0^{t_f}\int_0^R\int_0^Z \lambda_1\frac{\partial(f_1)}{\partial T_{rr}}\delta T_{rr} dzdrdt + \int_0^{t_f}\int_0^R\int_0^Z \lambda_1\frac{\partial(f_1)}{\partial T_z}\delta T_z dzdrdt +$$

$$\int_0^{t_f}\int_0^R\int_0^Z \lambda_1\frac{\partial(f_1)}{\partial T_{zz}}\delta T_{zz} dzdrdt - \int_0^{t_f}\int_0^R\int_0^Z \lambda_2\frac{\partial(\delta\omega)}{\partial t}dzdrdt + \int_0^{t_f}\int_0^R\int_0^Z \lambda_2\frac{\partial(f_2)}{\partial\omega}\delta\omega dzdrdt +$$

$$\int_0^{t_f}\int_0^R\int_0^Z \lambda_2\frac{\partial(f_2)}{\partial\omega_z}\delta\omega_z dzdrdt + \int_0^{t_f}\int_0^R\int_0^Z \lambda_2\frac{\partial(f_2)}{\partial\omega_r}\delta\omega_r dzdrdt + \int_0^{t_f}\int_0^R\int_0^Z \lambda_2\frac{\partial(f_2)}{\partial\omega_{rr}}\delta\omega_{rr} dzdrdt -$$

$$\int_0^{t_f}\int_0^R \lambda_3\frac{\partial(\delta Z)}{\partial t}drdt + \int_0^{t_f}\int_0^R \lambda_3\delta f_3 drdt + \int_0^{t_f}\int_0^R\int_0^Z G_1\delta\lambda_1 dzdrdt +$$

$$\int_0^{t_f}\int_0^R\int_0^Z G_2\delta\lambda_2 dzdrdt + \int_0^{t_f}\int_0^R H\,\delta\lambda_3 drdt = 0 \tag{49}$$

where

$$T_r = \frac{\partial T}{\partial r}, T_z = \frac{\partial T}{\partial z}, T_{rr} = \frac{\partial^2 T}{\partial r^2}, T_{zz} = \frac{\partial^2 T}{\partial z^2} \tag{50}$$

and

$$\omega_r = \frac{\partial\omega}{\partial r}, \omega_z = \frac{\partial\omega}{\partial z}, \omega_{rr} = \frac{\partial^2\omega}{\partial r^2} \tag{51}$$

Simplification of δJ using Integration by Parts

Applying integration by parts of the second integral of Equation (49), it leads to:

$$\int_0^{t_f}\int_0^{R}\int_0^{Z}\lambda_1\frac{\partial(\delta T)}{\partial t}dzdrdt = \int_0^{R}\int_0^{Z}\lambda_1\delta T\,|_0^{t_f}\,dzdr - \int_0^{t_f}\int_0^{R}\int_0^{Z}\frac{\partial\lambda_1}{\partial t}\delta T dzdrdt \quad (52)$$

By applying the initial conditions into the first integral on the right hand side in Equation (52). Because the initial temperature of solvent is fixed, $\delta T(0,r,z)$is zero for all r and z. Now, if we specify:

$$\lambda_1(t_f,r,z) = 0, 0 \le r \le R \; and \; 0 \le z \le Z_0$$

Therefore, Equation (52) can be written as:

$$\int_0^{t_f}\int_0^{R}\int_0^{Z}\lambda_1\frac{\partial(\delta T)}{\partial t}dzdrdt = -\int_0^{t_f}\int_0^{R}\int_0^{Z}\frac{\partial\lambda_1}{\partial t}\delta T dzdrdt \quad (53)$$

By applying then boundary conditions into the fourth part of the integral Equation (49), we can obtain the following equation:

$$\int_0^{t_f}\int_0^{R}\int_0^{Z}\lambda_1\left(\frac{\partial f_1}{\partial T_r}\delta T_r\right)dzdrdt = \int_0^{t_f}\int_0^{Z}\lambda_1\frac{\partial f_1}{\partial T_r}\delta T|_0^R dzdt - \int_0^{t_f}\int_0^{R}\int_0^{Z}\frac{\partial}{\partial r}\left(\lambda_1\frac{\partial f_1}{\partial T_r}\delta T\right)dzdrdt \quad (54)$$

Considering that δT is arbitrary at r = 0 and the fact that all additive terms of δJ must be individually zero, it follows that:

$$\lambda_1(t,0,z) = 0 \;\; \forall\, t: 0 \le t \le t_f \; and \; 0 \le z \le Z$$

Which it yields to:

$$\int_0^{t_f}\int_0^R\int_0^Z \lambda_1\left(\frac{\partial f_1}{\partial T_r}\delta T_r\right)dzdrdt = \int_0^{t_f}\int_0^Z \lambda_1\frac{\partial f_1}{\partial T_r}\delta T(t,R,z)dzdt -$$

$$\int_0^{t_f}\int_0^R\int_0^Z \frac{\partial}{\partial r}\left(\lambda_1\frac{\partial f_1}{\partial T_r}\delta T\right)dzdrdt \quad (55)$$

Applying integration by part to the fifth integral of Equation (49), we have obtained the following equation:

$$\int_0^{t_f}\int_0^R\int_0^Z \lambda_1\left(\frac{\partial f_1}{\partial T_{rr}}\delta T_{rr}\right)dzdrdt = \int_0^{t_f}\int_0^Z \lambda_1\frac{\partial f_1}{\partial T_{rr}}\delta T_r|_0^R dzdt -$$

$$\int_0^{t_f}\int_0^R\int_0^Z \frac{\partial}{\partial r}\left(\lambda_1\frac{\partial f_1}{\partial T_{rr}}\right)\delta T_r dzdrdt \quad (56)$$

By applying integration by part to the second integral of Equation (56) with respect to r-results in:

$$\int_0^{t_f}\int_0^R\int_0^Z \lambda_1\left(\frac{\partial f_1}{\partial T_{rr}}\right)\delta T_r dzdrdt = \int_0^{t_f}\int_0^Z \lambda_1\frac{\partial f_1}{\partial T_{rr}}\delta T_r|_0^R dzdt - \int_0^{t_f}\int_0^Z \frac{\partial}{\partial r}(\lambda_1\frac{\delta f_1}{\delta T_{rr}})\delta T|_0^R dzdt +$$

$$\int_0^{t_f}\int_0^R\int_0^Z \frac{\partial^2}{\partial r^2}\left(\lambda_1\frac{\partial f_1}{\partial T_{rr}}\right)\delta T dzdrdt \quad (57)$$

Considering that δT is arbitrary at $r=R$ and the fact that all additive terms of δJ must be individually zero, it follows that

$$\lambda_1(t,R,z) = 0\ , 0 \le t \le t_f, 0 \le z \le Z \quad (58)$$

In addition, that T_r is zero at $r = 0$ because of the symmetric geometry of the physical model around the z-axis. This makes Equation (56) to be simplified further as:

$$\int_0^{t_f}\int_0^R\int_0^Z \lambda_1\left(\frac{\partial f_1}{\partial T_{rr}}\delta T_{rr}\right)dzdrdt = -\int_0^{t_f}\int_0^Z \frac{\partial\lambda_1}{\partial r}\left(\frac{\partial f_1}{\partial T_{rr}}\right)\partial T_r(t,R,z)\ dzdt +$$

$$\int_0^{t_f}\int_0^R\int_0^Z \frac{\partial^2}{\partial r^2}\left(\lambda_1\frac{\partial f_1}{\partial T_{rr}}\right)\delta T dzdrdt \quad (59)$$

Applying integration by parts of the sixth integral of Equation (49), we obtain:

$$\int_0^{t_f}\int_0^R\int_0^Z \lambda_1 \frac{\partial f_1}{\partial T_z}\delta T_z dzdrdt = \int_0^{t_f}\int_0^R \lambda_1 \frac{\partial f_1}{\partial T_z}\delta T_z|_0^Z drdt - \int_0^{t_f}\int_0^R\int_0^Z \frac{\partial}{\partial z}\left(\lambda_1 \frac{\partial f_1}{\partial T_z}\right)\partial T_z dzdrdt \quad (60)$$

By applying the boundary conditions into the first integral of Equation (60) we obtain the following equation:

$$\left(-\lambda_1 \frac{\partial f_1}{\partial T_z}\delta T|_Z + \lambda_1 \frac{\partial f_1}{\partial T_z}\delta T|_0\right) dzdt \quad (61)$$

$$T = T(t) \;\; at \;\; z = 0 \text{ and } z = Z(r,t) \; \forall 0 \le r < R$$

Therefore, Equation (61) becomes:

$$\int_0^{t_f}\int_0^R\int_0^Z \lambda_1 \frac{\partial f_1}{\partial T_z}\delta T_z dzdrdt = \int_0^{t_f}\int_0^R \lambda_1 \frac{\partial f_1}{\partial T_z}\delta T(t,r,Z)\, drdt -$$

$$\int_0^{t_f}\int_0^R \lambda_1 \frac{\partial f_1}{\partial T_z}\delta T(t,r,0)\, drdt - \int_0^{t_f}\int_0^R\int_0^Z \frac{\partial}{\partial z}\left(\lambda_1 \frac{\delta f_1}{\delta T_z}\right)\partial T dzdrdt \quad (62)$$

Applying integration by part of the <u>seventh integral of Equation (49)</u>:

$$\int_0^{t_f}\int_0^R\int_0^Z \lambda_1 \frac{\partial f_1}{\partial T_{zz}}\delta T_{zz} dzdrdt = \int_0^{t_f}\int_0^R \lambda_1 \frac{\partial f_1}{\partial T_{zz}}\delta T|_0^Z drdt - \int_0^{t_f}\int_0^R\int_0^Z \frac{\partial}{\partial z}\left(\lambda_1 \frac{\partial f_1}{\partial T_{zz}}\right)\partial T_z dzdrdt \quad (63)$$

Applying the integration by part to the second integral of Equation (63):

$$\int_0^{t_f}\int_0^R\int_0^Z \lambda_1 \left(\frac{\partial f_1}{\partial T_{zz}}\right)\partial T_z dzdrdt = \int_0^{t_f}\int_0^R \lambda_1 \frac{\partial f_1}{\partial T_{zz}}\delta T|_0^Z drdt - \int_0^{t_f}\int_0^R \frac{\partial}{\partial z}(\lambda_1 \frac{\partial f_1}{\partial T_{zz}})\delta T|_0^Z drdt +$$

$$\int_0^{t_f}\int_0^R\int_0^Z \frac{\partial^2}{\partial z^2}\left(\lambda_1 \frac{\partial f_1}{\partial T_{zz}}\right)\partial T dzdrdt \quad (64)$$

As a result, Equation (63) can be written as:

$$\int_0^{t_f}\int_0^R\int_0^Z \lambda_1 \frac{\partial f_1}{\partial T_{zz}}\delta T_{zz}dzdrdt = \int_0^{t_f}\int_0^R \lambda_1 \frac{\partial f_1}{\partial T_{zz}}\delta T(t,r,Z)drdt - \int_0^{t_f}\int_0^R \lambda_1 \frac{\partial f_1}{\partial T_{zz}}\delta T(t,r,0)drdt -$$

$$\int_0^{t_f}\int_0^R \frac{\partial}{\partial z}(\lambda_1 \frac{\partial f_1}{\partial T_{zz}})\delta T(t,r,Z)drdt + \int_0^{t_f}\int_0^R \frac{\partial}{\partial z}(\lambda_1 \frac{\partial f_1}{\partial T_{zz}})\delta T(t,r,0)drdt +$$

$$\int_0^{t_f}\int_0^R\int_0^Z \frac{\partial^2}{\partial z^2}\left(\lambda_1 \frac{\partial f_1}{\partial T_{zz}}\right)\partial T dzdrdt \quad (65)$$

Applying the eighth of integration from Equation (49):

$$\int_0^{t_f}\int_0^R\int_0^Z \lambda_2 \frac{\partial(\delta\omega)}{\partial t}dzdrdt = \int_0^R\int_0^Z \lambda_2\delta\omega|_0^{t_f}\, dzdr - \int_0^{t_f}\int_0^R\int_0^Z \frac{\partial\lambda_2}{\partial t}\delta\omega dzdrdt \quad (66)$$

Because initial mass fraction of the solvent gas $\delta\omega(0,r,z)$ is zero for all r and z. Now, if we specify:

$$\lambda_2(t_f,r,z) = 0 \quad \forall r: 0 \le r \le R \; and \quad \forall\, 0 \le z \le Z_o$$

Therefore, Equation (66) becomes:

$$\int_0^{t_f}\int_0^R\int_0^Z \lambda_2 \frac{\partial(\delta\omega)}{\partial t}dzdrdt = -\int_0^{t_f}\int_0^R\int_0^Z \frac{\partial\lambda_2}{\partial t}\delta\omega\, dzdrdt \quad (67)$$

Applying integration by parts of the tenth of Equation (49) with respect to z, we can obtain

$$\int_0^{t_f}\int_0^R\int_0^Z \lambda_2 \frac{\partial f_2}{\partial\omega_z}\delta\omega_z dzdrdt = \int_0^{t_f}\int_0^R \lambda_2 \frac{\partial f_2}{\delta\omega_z}\delta\omega|_0^Z\, drdt - \int_0^{t_f}\int_0^R\int_0^Z \frac{\partial}{\partial z}(\lambda_2 \frac{\partial f_2}{\partial\omega_z})\delta\omega dzdrdt \quad (68)$$

Or, it can be simplified into:

$$\int_0^{t_f}\int_0^R\int_0^Z \lambda_2 \frac{\partial f_2}{\partial\omega_z}\delta\omega_z dzdrdt = \int_0^{t_f}\int_0^R \lambda_2 \frac{\partial f_2}{\delta\omega_z}\delta\omega(t,r,Z)\, drdt + \int_0^{t_f}\int_0^R \lambda_2 \frac{\partial f_2}{\delta\omega_z}\delta\omega(t,r,0)\, drdt -$$

$$\int_0^{t_f}\int_0^R\int_0^Z \frac{\partial}{\partial z}(\lambda_2 \frac{\partial f_2}{\partial\omega_z})\delta\omega dzdrdt \quad (69)$$

Applying integration by parts eleventh integral of Equation (49) we obtain the following equation:

$$\int_0^{t_f}\int_0^R\int_0^Z \lambda_2\left(\frac{\partial f_2}{\partial \omega_r}\delta\omega_r\right)dzdrdt = \int_0^{t_f}\int_0^Z \lambda_2\frac{\partial f_2}{\delta\omega_r}\delta\omega|_0^R\, dzdt - \int_0^{t_f}\int_0^R\int_0^Z \frac{\partial}{\partial r}(\lambda_2\frac{\partial f_2}{\partial \omega_r})\delta\omega dzdrdt \quad (70)$$

Considering that $\delta\omega$ is arbitrary at r = 0 and the fact that all additive terms of δJ must be individually zero (Equation 49), it follows that

$$\lambda_2(t,0,z) = 0 \quad \forall t: 0 \le t \le t_f \; and \; \forall\, 0 \le z \le Z_o$$

Therefore, Equation (70) becomes:

$$\int_0^{t_f}\int_0^R\int_0^Z \lambda_2\left(\frac{\partial f_2}{\partial \omega_r}\delta\omega_r\right)dzdrdt = \int_0^{t_f}\int_0^Z \lambda_2\frac{\partial f_2}{\delta\omega_r}\delta\omega\,(t,R,z)\,dzdt -$$

$$\int_0^{t_f}\int_0^R\int_0^Z \frac{\partial}{\partial r}(\lambda_2\frac{\partial f_2}{\partial \omega_r})\delta\omega dzdrdt \quad (71)$$

Applying integration by parts to the twelfth integral of Equation (49), we can obtain the following equation:

$$\int_0^{t_f}\int_0^R\int_0^Z \lambda_2\left(\frac{\partial f_2}{\partial \omega_{rr}}\delta\omega_{rr}\right)dzdrdt = \int_0^{t_f}\int_0^Z \lambda_2\frac{\partial f_2}{\partial \omega_{rr}}\delta\omega|_0^R\, dzdt -$$

$$\int_0^{t_f}\int_0^R\int_0^Z \frac{\partial}{\partial r}(\lambda_2\frac{\partial f_2}{\partial \omega_{rr}})\delta\omega_r dzdrdt \quad (72)$$

Applying integration by parts to the second integral of Equation (72) with respect to r results in:

$$\int_0^{t_f}\int_0^R\int_0^Z (\lambda_2\frac{\partial f_2}{\partial \omega_{rr}})\delta\omega_r dzdrdt = \int_0^{t_f}\int_0^Z \lambda_2\frac{\partial f_2}{\partial \omega_{rr}}\delta\omega_r|_0^R\, dzdt - \int_0^{t_f}\int_0^Z \frac{\partial}{\partial r}(\lambda_2\frac{\partial f_2}{\partial \omega_{rr}})\delta\omega|_0^R\, dzdt +$$

$$\int_0^{t_f}\int_0^R\int_0^Z \frac{\partial^2}{\partial r^2}(\lambda_2\frac{\partial f_2}{\partial \omega_{rr}})\delta\omega dzdrdt \quad (73)$$

Considering that $\delta\omega$ is arbitrary at r = R and the fact that all the additive terms of δJ must be individually zero (Equation (49)), it follows that:

$$\lambda_2(t,R,z) = 0, 0 \le t \le t_f, 0 \le z \le Z$$

In addition, ω_r is zero at r = 0 because of symmetry around the z-axis of the cylindrical physical model that makes Equation (73) get simplified to:

$$\int_0^{t_f}\int_0^{R}\int_0^{Z}\lambda_2\left(\frac{\partial f_2}{\partial \omega_{rr}}\delta\omega_{rr}\right)dzdrdt = -\int_0^{t_f}\int_0^{Z}\frac{\partial \lambda_2}{\partial r}\left(\frac{\partial f_2}{\partial \omega_{rr}}\right)\delta\omega(t,R,z)\,dzdt +$$

$$\int_0^{t_f}\int_0^{R}\int_0^{Z}\frac{\partial^2}{\partial r^2}(\lambda_2\frac{\partial f_2}{\partial \omega_{rr}})\delta\omega dzdrdt \tag{74}$$

Applying integration by parts to the thirteenth integral of Equation (49), we obtain

$$\int_0^{t_f}\int_0^{R}\lambda_3\left(\frac{\partial(\delta z)}{\partial t}\right)drdt = \int_0^{R}\lambda_3\delta z\Big|_0^{t_f}dr - \int_0^{t_f}\int_0^{R}\frac{\partial\lambda_3}{\partial t}\delta Zdrdt \tag{75}$$

Using the fact that δZ is zero at t = 0 because the initial height is specified as:

$$\lambda_3(t_f,r) = 0 \quad \forall\, 0 \le r \le R$$

As a result, Equation (75) becomes:

$$\int_0^{t_f}\int_0^{R}\lambda_3\left(\frac{\partial(\delta z)}{\partial t}\right)drdt = -\int_0^{t_f}\int_0^{R}\frac{\partial\lambda_3}{\partial t}\delta Zdrdt \tag{76}$$

The last integral of Equation (49):

$$\int_0^{t_f}\int_0^{R}\lambda_3\delta f_3 drdt = \int_0^{t_f}\int_0^{R}\lambda_3\frac{\partial f_3}{\partial\omega}\delta\omega(t,r,0)drdt \tag{77}$$

By substituting of the simplified into Equation (49) and rearrange, we obtain the final equation of variation of δJ, which is written as:

$$\delta J = -\int_0^{t_f}\int_0^{R}\beta\, r\delta z drdt + \int_0^{t_f}\int_0^{R}\int_0^{Z}\frac{\partial\lambda_1}{\partial t}\delta T dzdrdt + \int_0^{t_f}\int_0^{R}\int_0^{Z}\lambda_1\frac{\partial f_1}{\partial T}\delta T dzdrdt +$$

$$\int_0^{R}\int_0^{Z}\lambda_1\frac{\partial f_1}{\partial T_r}\delta T(t,R,z)dzdt - \int_0^{t_f}\int_0^{R}\int_0^{Z}\frac{\delta}{\delta r}\left(\lambda_1\frac{\partial f_1}{\partial T_r}\delta T\right)dzdrdt -$$

$$\int_0^{t_f}\int_0^{Z}\frac{\partial\lambda_1}{\partial r}\left(\frac{\partial f_1}{\partial T_{rr}}\right)\partial T(t,R,z)\,dzdt + \int_0^{t_f}\int_0^{R}\int_0^{Z}\frac{\partial^2}{\partial r^2}\left(\lambda_1\frac{\partial f_1}{\partial T_{rr}}\right)\partial T dzdrdt +$$

$$\int_0^{t_f}\int_0^R \lambda_1 \frac{\partial f_1}{\partial T_z}\delta T(t,r,Z)\,drdt -$$

$$\int_0^{t_f}\int_0^R \lambda_1 \frac{\partial f_1}{\partial T_z}\delta T(t,r,0)\,drdt - \int_0^{t_f}\int_0^R\int_0^Z \frac{\partial}{\partial z}\left(\lambda_1 \frac{\partial f_1}{\partial T_z}\right)\partial T dzdrdt +$$

$$\int_0^{t_f}\int_0^R \lambda_1 \frac{\partial f_1}{\partial T_{zz}}\delta T(t,r,Z)drdt - \int_0^{t_f}\int_0^R \lambda_1 \frac{\partial f_1}{\partial T_{zz}}\delta T(t,r,0)drdt -$$

$$\int_0^{t_f}\int_0^R \frac{\partial}{\partial z}(\lambda_1 \frac{\partial f_1}{\partial T_{zz}})\delta T(t,r,Z)drdt + \int_0^{t_f}\int_0^R \frac{\partial}{\partial z}(\lambda_1 \frac{\partial f_1}{\partial T_{zz}})\delta T(t,r,0)drdt +$$

$$\int_0^{t_f}\int_0^R\int_0^Z \frac{\partial^2}{\partial z^2}\left(\lambda_1 \frac{\partial f_1}{\partial T_{zz}}\right)\partial T dzdrdt + \int_0^{t_f}\int_0^R\int_0^Z \frac{\partial \lambda_2}{\partial t}\delta\omega\, dzdrdt + \int_0^{t_f}\int_0^R\int_0^Z \lambda_2 \frac{\partial f_2}{\partial \omega}\delta\omega dzdrdt +$$

$$\int_0^{t_f}\int_0^R \lambda_2 \frac{\partial f_2}{\partial \omega_z}\delta\omega(t,r,Z)\,drdt + \int_0^{t_f}\int_0^R \lambda_2 \frac{\partial f_2}{\partial \omega_z}\delta\omega(t,r,0)\,drdt -$$

$$\int_0^{t_f}\int_0^R\int_0^Z \frac{\partial}{\partial z}(\lambda_2 \frac{\partial f_2}{\partial \omega_z})\delta\omega dzdrdt + \int_0^{t_f}\int_0^Z \lambda_2 \frac{\partial f_2}{\partial \omega_r}\delta\omega(t,R,z)\,dzdt -$$

$$\int_0^{t_f}\int_0^R\int_0^Z \frac{\partial}{\partial r}(\lambda_2 \frac{\partial f_2}{\partial \omega_r})\delta\omega dzdrdt - \int_0^{t_f}\int_0^Z \frac{\partial \lambda_2}{\partial r}(\frac{\partial f_2}{\partial \omega_{rr}})\delta\omega(t,R,z)\,dzdt +$$

$$\int_0^{t_f}\int_0^R\int_0^Z \frac{\partial^2}{\partial r^2}(\lambda_2 \frac{\partial f_2}{\partial \omega_{rr}})\delta\omega dzdrdt + \int_0^{t_f}\int_0^R \frac{\partial \lambda_3}{\partial t}\delta Z drdt + \int_0^{t_f}\int_0^R \lambda_3 \frac{\partial f_3}{\partial \omega}\delta\omega(t,r,0)drdt +$$

$$\int_0^{t_f}\int_0^R\int_0^Z G_1\delta\lambda_1 dzdrdt + \int_0^{t_f}\int_0^R\int_0^Z G_2\delta\lambda_2 dzdrdt + \int_0^{t_f}\int_0^R\int_0^Z H\delta\lambda_3 dzdrdt = 0 \qquad (78)$$

Simplification of Equation (78):

$$\delta J = \int_0^{t_f}\int_0^R \left[-\beta r + \frac{\partial \lambda_3}{\partial t}\right]\delta Z drdt + \int_0^{t_f}\int_0^R\int_0^Z \left[\frac{\partial \lambda_2}{\partial t} + \lambda_2 \frac{\partial f_2}{\partial \omega} - \frac{\partial}{\partial z}\left(\lambda_2 \frac{\partial f_2}{\partial \omega_z}\right) - \frac{\partial}{\partial r}\left(\lambda_2 \frac{\partial f_2}{\partial \omega_r}\right) +$$

$$\frac{\partial^2}{\partial r^2}\left(\lambda_2 \frac{\partial f_2}{\partial \omega_{rr}}\right)\right]\delta\omega\, dzdrdt + \int_0^{t_f}\int_0^R \lambda_2 \frac{\partial f_2}{\partial \omega_z}\delta\omega(t,r,Z)\,drdt - \int_0^{t_f}\int_0^R \left[\lambda_2 \frac{\partial f_2}{\partial \omega_z} -$$

$$\lambda_3 \frac{\partial f_3}{\partial \omega}\right]\delta\omega(t,r,0)\,drdt + \int_0^{t_f}\int_0^Z [\lambda_2 \frac{\partial f_2}{\partial \omega_r} + \frac{\partial \lambda_2}{\partial r}(\frac{\partial f_2}{\delta \omega_{rr}})]\delta\omega(t,R,z)\,dzdt + \int_0^{t_f}\int_0^R\int_0^Z [+ \frac{\delta\lambda_1}{\delta t} +$$

$$\lambda_1 \frac{\partial f_1}{\partial T} - \frac{\partial}{\partial z}\left(\lambda_1 \frac{\partial f_1}{\partial T_z}\right) + \frac{\partial^2}{\partial z^2}\left(\lambda_1 \frac{\partial f_1}{\partial T_{zz}}\right) + \frac{\partial^2}{\partial r^2}\left(\lambda_1 \frac{\partial f_1}{\partial T_{rr}}\right) - \frac{\partial}{\partial r}\left(\lambda_1 \frac{\partial f_1}{\partial T_r}\right)]\delta T\, dzdrdt + \int_0^{t_f}\int_0^R [\lambda_1 \frac{\partial f_1}{\partial T_z} +$$

$$\lambda_1 \frac{\partial f_1}{\partial T_{zz}} - \frac{\partial}{\partial z}\left(\lambda_1 \frac{\partial f_1}{\partial T_{zz}}\right)]\,\delta T(t,r,Z)\,drdt - \int_0^{t_f}\int_0^R [\lambda_1 \frac{\partial f_1}{\partial T_z} + \lambda_1 \frac{\partial f_1}{\partial T_{zz}} -$$

$$\frac{\partial}{\partial z}\left(\lambda_1 \frac{\partial f_1}{\partial T_{zz}}\right)]\ \delta T(t,r,0)\ drdt + \int_0^{t_f}\int_0^{Z}[\lambda_1 \frac{\partial f_1}{\partial T_r} + \frac{\partial \lambda_1}{\partial r}\left(\frac{\partial f_1}{\partial T_{rr}}\right)]\ \delta T(t,R,z)dzdt +$$

$$\int_0^{t_f}\int_0^{R}\int_0^{Z} G_1 \delta\lambda_1 dzdrdt + \int_0^{t_f}\int_0^{R}\int_0^{Z} G_2 \delta\lambda_2 dzdrdt + \int_0^{t_f}\int_0^{R}\int_0^{Z} H\delta\lambda_3 dzdrdt = 0 \quad (79)$$

Note that

$$\delta\omega(t,R,z) = \delta\omega(t,r,0) = \delta\omega(t,r,Z) = \delta\omega_{\text{int}}(t) \quad (80)$$

$$\delta T(t,R,z) = \delta T(t,r,0) = \delta T(t,r,Z) = \delta T_{\text{int}}(t) \quad (81)$$

Lastly, since the interfacial air mass fraction is a strong function of temperature (T_{int}) with time, we can write the following condition (Pleas see Section 3.5):

$$\omega_{\text{int}} = \omega_{\text{int}}(T_{\text{int}}) \quad (82)$$

which represent the functionality of interfacial concentration to temperature at $r = R$. As a result, the equation above can be written as:

$$\delta\omega_{\text{int}} = \frac{\partial\omega_{\text{int}}}{\partial T_{\text{int}}} \times \delta T_{\text{int}} \quad (83)$$

By applying Equations (80) and (81), we can re-write Equation (79) as:

$$\delta J = \int_0^{t_f}\int_0^{R}\left[-\beta r + \frac{\partial\lambda_3}{\partial t}\right]\delta Z dr dt + \int_0^{t_f}\int_0^{R}\int_0^{Z}\left[\frac{\partial\lambda_2}{\partial t} + \lambda_2\frac{\partial f_2}{\partial\omega} - \frac{\partial}{\partial z}\left(\lambda_2\frac{\partial f_2}{\partial\omega_z}\right) - \frac{\partial}{\partial r}\left(\lambda_2\frac{\partial f_2}{\partial\omega_r}\right) +$$

$$\frac{\partial^2}{\partial r^2}\left(\lambda_2\frac{\partial f_2}{\partial\omega_{rr}}\right)\Big]\delta\omega\ dzdrdt\ + \int_0^{t_f}\int_0^{R}\lambda_2\frac{\partial f_2}{\partial\omega_z}\delta\omega_{int}\ drdt - \int_0^{t_f}\int_0^{R}\left[\lambda_2\frac{\partial f_2}{\partial\omega_z} - \lambda_3\frac{\partial f_3}{\partial\omega}\right]\delta\omega_{int}\ drdt +$$

$$\int_0^{t_f}\int_0^{Z}[\lambda_2\frac{\partial f_2}{\partial\omega_r} + \frac{\partial\lambda_2}{\partial r}(\frac{\partial f_2}{\delta\omega_{rr}})]\delta\omega_{int}\ dzdt + \int_0^{t_f}\int_0^{R}\int_0^{Z}[\ + \frac{\delta\lambda_1}{\delta t} + \lambda_1\frac{\partial f_1}{\partial T} - \frac{\partial}{\partial z}\left(\lambda_1\frac{\partial f_1}{\partial T_z}\right) +$$

$$\frac{\partial^2}{\partial z^2}\left(\lambda_1\frac{\partial f_1}{\partial T_{zz}}\right) + \frac{\partial^2}{\partial r^2}\left(\lambda_1\frac{\partial f_1}{\partial T_{rr}}\right) - \frac{\partial}{\partial r}\left(\lambda_1\frac{\partial f_1}{\partial T_r}\right)]\delta T\ dzdrdt + \int_0^{t_f}\int_0^{R}[\lambda_1\frac{\partial f_1}{\partial T_z} + \lambda_1\frac{\partial f_1}{\partial T_{zz}} -$$

$$\frac{\partial}{\partial z}\left(\lambda_1\frac{\partial f_1}{\partial T_{zz}}\right)]\ \delta T_{int}\ drdt - \int_0^{t_f}\int_0^{R}[\lambda_1\frac{\partial f_1}{\partial T_z} + \lambda_1\frac{\partial f_1}{\partial T_{zz}} - \frac{\partial}{\partial z}\left(\lambda_1\frac{\partial f_1}{\partial T_{zz}}\right)]\ \delta T_{int}\ drdt + \int_0^{t_f}\int_0^{Z}[\lambda_1\frac{\partial f_1}{\partial T_r} +$$

$$\frac{\partial \lambda_1}{\partial r}\left(\frac{\partial f_1}{\partial T_{rr}}\right)]\,\delta T_{int} dzdt + \int_0^{t_f}\int_0^R\int_0^Z G_1 \delta\lambda_1 dzdrdt +$$

$$\int_0^{t_f}\int_0^R\int_0^Z G_2 \delta\lambda_2 dzdrdt + \int_0^{t_f}\int_0^R\int_0^Z H\delta\lambda_3 dzdrdt = 0 \tag{84}$$

By rearranging Equation (84), it leads to:

$$\delta J = \underbrace{\left(\int_0^{t_f}\int_0^R\left[-\beta r + \frac{\partial \lambda_3}{\partial t}\right]\delta Z dr dt\right)}_{\delta J1} +$$

$$\underbrace{\left(\int_0^{t_f}\int_0^R\int_0^Z\left[\frac{\partial \lambda_2}{\partial t} + \lambda_2\frac{\partial f_2}{\partial \omega} - \frac{\partial}{\partial z}\left(\lambda_2\frac{\partial f_2}{\partial \omega_z}\right) - \frac{\partial}{\partial r}\left(\lambda_2\frac{\partial f_2}{\partial \omega_r}\right) + \frac{\partial^2}{\partial r^2}\left(\lambda_2\frac{\partial f_2}{\partial \omega_{rr}}\right)\right]\delta\omega\, dzdrdt\right)}_{\delta J2} +$$

$$\underbrace{\begin{pmatrix}\int_0^{t_f}\int_0^R \lambda_2\frac{\partial f_2}{\partial \omega_z}\delta\omega_{int}\, drdt - \int_0^{t_f}\int_0^R\left[\lambda_2\frac{\partial f_2}{\partial \omega_z} - \lambda_3\frac{\partial f_3}{\partial \omega}\right]\delta\omega_{int}\, drdt \\ + \int_0^{t_f}\int_0^Z[\lambda_2\frac{\partial f_2}{\partial \omega_r} + \frac{\partial \lambda_2}{\partial r}(\frac{\partial f_2}{\delta \omega_{rr}})]\delta\omega_{int}\, dzdt\end{pmatrix}}_{\delta J3} +$$

$$\underbrace{\begin{pmatrix}\int_0^{t_f}\int_0^R\int_0^Z + \frac{\delta\lambda_1}{\delta t} + \lambda_1\frac{\partial f_1}{\partial T} - \frac{\partial}{\partial z}\left(\lambda_1\frac{\partial f_1}{\partial T_z}\right) + \frac{\partial^2}{\partial z^2}\left(\lambda_1\frac{\partial f_1}{\partial T_{zz}}\right) \\ + \frac{\partial^2}{\partial r^2}\left(\lambda_1\frac{\partial f_1}{\partial T_{rr}}\right) - \frac{\partial}{\partial r}\left(\lambda_1\frac{\partial f_1}{\partial T_r}\right)\delta T\, dzdrdt\end{pmatrix}}_{\delta J4} +$$

$$\underbrace{\begin{pmatrix}\int_0^{t_f}\int_0^R[\lambda_1\frac{\partial f_1}{\partial T_z} + \lambda_1\frac{\partial f_1}{\partial T_{zz}} - \frac{\partial}{\partial z}\left(\lambda_1\frac{\partial f_1}{\partial T_{zz}}\right)]\,\delta T_{int}\, drdt - \int_0^{t_f}\int_0^R[\lambda_1\frac{\partial f_1}{\partial T_z} + \lambda_1\frac{\partial f_1}{\partial T_{zz}} - \frac{\partial}{\partial z}\left(\lambda_1\frac{\partial f_1}{\partial T_{zz}}\right)]\,\delta T_{int}\, drdt + \\ \int_0^{t_f}\int_0^Z[\lambda_1\frac{\partial f_1}{\partial T_r} + \frac{\partial \lambda_1}{\partial r}\left(\frac{\partial f_1}{\partial T_{rr}}\right)]\,\delta T_{int} dzdt\end{pmatrix}}_{\delta J5} +$$

$$\underbrace{\left(\int_0^{t_f}\int_0^R\int_0^Z G_1\delta\lambda_1 dzdrdt\right)}_{\delta J6} + \underbrace{\left(\int_0^{t_f}\int_0^R\int_0^Z G_2\delta\lambda_2 dzdrdt\right)}_{\delta J7} + \underbrace{\left(\int_0^{t_f}\int_0^R\int_0^Z H\delta\lambda_3 dzdrdt\right)}_{\delta J8} = 0 \tag{85}$$

Assuming that the involved function is sufficiently differentiable, δJ is zero if all the individual in Equation (85) is zero.

The elimination of the first, second, and fourth terms by defining the variational derivative with respect to T_{int} and ω_{int}:

$$\frac{\partial \lambda_3}{\partial t} = \beta r = 2\pi\rho\emptyset r \tag{86}$$

$$0 \le t \le t_f \; and \; 0 \le r \le R$$

Next, we obtain:

$$\frac{\partial \lambda_2}{\partial t} = -\lambda_2 \frac{\partial f_2}{\partial \omega} + \frac{\partial}{\partial z}\left(\lambda_2 \frac{\partial f_2}{\partial \omega_z}\right) + \frac{\partial}{\partial r}\left(\lambda_2 \frac{\partial f_2}{\partial \omega_{rr}}\right) - \frac{\partial^2}{\partial r^2}\left(\lambda_2 \frac{\partial f_2}{\partial \omega_{rr}}\right) \quad (87)$$

where

$$f_2 = \left(\frac{\partial D}{\partial \omega}\right).\left(\frac{\partial \omega}{\partial r}\right)^2 + \frac{D}{r}\left(\frac{\partial \omega}{\partial r}\right) + D\left(\frac{\partial^2 \omega}{\partial r^2}\right) - 3\alpha \frac{\omega^2}{\phi}\left(\frac{\partial \omega}{\partial z}\right)$$

Thus, Equation (87) can be written as:

$$\frac{\partial \lambda_2}{\partial t} = -\frac{3\alpha}{\emptyset}\omega^2 \frac{\partial \lambda_2}{\partial z} + \frac{\partial \lambda_2}{\partial r}\frac{D}{r} - \lambda_2 \frac{D}{r^2} - \frac{\partial^2 \lambda_2}{\partial r^2} \quad (88)$$

$$0 \le t \le t_f\ , 0 \le r \le R,, 0 \le z \le Z$$

Lastly, we have:

$$\frac{\partial \lambda_1}{\partial t} = -\lambda_1 \frac{\partial f_1}{\partial T} + \frac{\partial}{\partial z}\left(\lambda_1 \frac{\partial f_1}{\partial T_z}\right) - \frac{\partial^2}{\partial z^2}\left(\lambda_1 \frac{\partial f_1}{\partial T_{zz}}\right) - \frac{\partial^2}{\partial r^2}\left(\lambda_1 \frac{\partial f_1}{\partial T_{rr}}\right) + \frac{\partial}{\partial r}\left(\lambda_1 \frac{\partial f_1}{\partial T_r}\right) \quad (89)$$

where

$$f_1 = \gamma\left[\frac{1}{r}\frac{\partial T}{\partial r} + \frac{\partial^2 T}{\partial r^2}\right] + \gamma\left[\frac{\partial^2 T}{\partial z^2}\right] - \alpha\frac{\omega^2}{\emptyset}\left[\frac{\partial T}{\partial z}\right]$$

As a result,

$$\frac{\partial \lambda_1}{\partial t} = \frac{\partial \lambda_1}{\partial z}\left[-\alpha\frac{\omega^2}{\emptyset}\right] - \frac{\partial^2 \lambda_1}{\partial z^2}[\gamma] - \frac{\partial^2 \lambda_1}{\partial r^2}[\gamma] + \frac{\partial \lambda_1}{\partial r}\left[\frac{\gamma}{r}\right] \quad (90)$$

$$0 \le t \le t_f\ , 0 \le r \le R,, 0 \le z \le Z$$

We also need to eliminate the rest of terms in Equation (85), i.e.,

$$\int_0^R [\,\lambda_2 \frac{\partial f_2}{\partial \omega_z}]_Z - \left[\lambda_2 \frac{\partial f_2}{\partial \omega_z} - \lambda_3 \frac{\partial f_3}{\partial \omega}]_{z=0}\right] dr + \int_0^Z \left[\lambda_2 \frac{\partial f_2}{\partial \omega_r} - \frac{\partial \lambda_2}{\partial r}\frac{\partial f_3}{\partial \omega_{rr}}\right]_{r=R} dz = \frac{\partial J}{\partial \omega_{int}} \quad (91)$$

The above term needs to be zero to make ∂J zero. The above equation is the stationarity condition, and the term is called the variation derivative of *J* with respect to ω_{int}.

Equation (91) can be simplified by using Equations (43) and (45)

$$\frac{\partial J}{\partial \omega_{int}} = \int_0^R \left[-3\alpha\lambda_2 \frac{\omega^2}{\emptyset}\right]_{z=Z} - \left[-3\alpha\lambda_2 \frac{\omega^2}{\emptyset} + \frac{2\lambda_3 \alpha\omega}{\emptyset}\right]_{z=0}] \, dr + \int_0^Z \left[\lambda_2 \frac{\partial D}{\partial \omega}\frac{\partial \omega}{\partial r} + \lambda_2 \frac{D}{r} - \frac{\partial \lambda_2}{\partial r} D\right]_{r=R} dz = 0 \quad (92)$$

$$0 \leq t \leq t_f$$

similarly:

$$\frac{\partial J}{\partial T_{int}} = \int_0^R \left[\lambda_1 \frac{\partial f_1}{\partial T_z} + \lambda_1 \frac{\partial f_1}{\partial T_{zz}} - \frac{\partial}{\partial z}\left(\lambda_1 \frac{\partial f_1}{\partial T_{zz}}\right)\right]_{z=Z} - \left[\lambda_1 \frac{\partial f_1}{\partial T_z} + \lambda_1 \frac{\partial f_1}{\partial T_{zz}} - \frac{\partial}{\partial z}\left(\lambda_1 \frac{\partial f_1}{\partial T_{zz}}\right)\right]_{z=0} dr + \int_0^Z \left[\lambda_1 \frac{\partial f_1}{\partial T_r} + \frac{\partial \lambda_1}{\partial r}\left(\frac{\partial f_1}{\partial T_{rr}}\right)\right]_{r=R} dz \quad (93)$$

Equation (93) can be simplified by using Equation (41)

$$\int_0^R \left[\lambda_1(-\alpha \frac{\omega^2}{\emptyset}) + \lambda_1(\gamma) - \frac{\partial \lambda_1}{\partial z}(\gamma)\right]_{z=Z} - \left[\lambda_1\left(-\alpha \frac{\omega^2}{\emptyset}\right) + \lambda_1(\gamma) - \frac{\partial \lambda_1}{\partial z}(\gamma)\right]_{z=0} dr + \int_0^Z \left[\lambda_1\left(\frac{\gamma}{r}\right) + \frac{\partial \lambda_1}{\partial r}(\gamma)\right]_{r=R} dz = \frac{\partial J}{\partial T_{int}} \quad (94)$$

$$0 \leq t \leq t_f$$

Parallel to Equation (91), Equation (94) needs to be zero to help make ∂J zero. The equation above is the stationarity condition, and the term is called the variation derivative of *J* with respect to T_{int}.

Therefore, $\frac{\partial J}{\partial \omega_{\text{int}}}$ is the variational derivative J with respect to ω_{int} resulting to:

$G_2 = 0$ and $H = 0$

Similarly, $\frac{\partial J}{\partial T_{\mathrm{int}}(t)}$ is the variational derivative J with respect to $T_{\mathrm{int}}(t)$ resulting to:

$G_1 = 0$

Lastly, according to Equation (83), we can combine the Equations (92) and (94). Therefore:

$$\frac{\partial J}{\partial T_{int}} = \left[\int_0^R \left[\lambda_1\left(-\alpha\frac{\omega^2}{\emptyset}\right) + \lambda_1(\gamma) - \frac{\partial\lambda_1}{\partial z}(\gamma)\right]_{z=Z} - \left[\lambda_1\left(-\alpha\frac{\omega^2}{\emptyset}\right) + \lambda_1(\gamma) - \frac{\partial\lambda_1}{\partial z}(\gamma)\right]_{z=0} dr + \int_0^Z \left[\lambda_1\left(\frac{\gamma}{r}\right) + \frac{\partial\lambda_1}{\partial r}(\gamma)\right]_{r=R} dz + \int_0^R [\left[-3\alpha\lambda_2\frac{\omega^2}{\emptyset}\right]_{z=Z} - \left[-3\alpha\lambda_2\frac{\omega^2}{\emptyset} + 2\alpha\lambda_3\frac{\omega}{\emptyset}\right]_{z=0}] dr + \int_0^Z \left[\lambda_2\frac{\partial D}{\partial\omega}\frac{\partial\omega}{\partial r} + \lambda_2\frac{D}{r} - \frac{\partial\lambda_2}{\partial r}D\right]_{r=R} dz\right] = 0 \quad (95)$$

For the *J* function to be optimal, the necessary conditions given by Equation (95) must be satisfied along with Equations (26), (30), (34), and the costate equations. If the *J* function is not optimal, then a correction in the gradient direction ensures an improvement in the objective function. It worth to mention that discretization of [$T_{\mathrm{int}}(t)$], and cubic splines were used to obtain [$T_{\mathrm{int}}(t)$] when solving the mathematical modeling.

4.5 Implementation of the Improvement Method

The search direction was set by the variation derivative $J_{T\mathrm{int}}$ given by:

$$\frac{\partial J}{\partial T_{int}} = J_{T_{int}} = \left[\int_0^R \left[\lambda_1\left(-\alpha\frac{\omega^2}{\emptyset}\right) + \lambda_1(\gamma) - \frac{\partial\lambda_1}{\partial z}(\gamma)\right]_{z=Z} - \left[\lambda_1\left(-\alpha\frac{\omega^2}{\emptyset}\right) + \lambda_1(\gamma) - \frac{\partial\lambda_1}{\partial z}(\gamma)\right]_{z=0} dr + \int_0^Z \left[\lambda_1\left(\frac{\gamma}{r}\right) + \frac{\partial\lambda_1}{\partial r}(\gamma)\right]_{r=R} dz + \int_0^R [\left[-3\alpha\lambda_2\frac{\omega^2}{\emptyset}\right]_{z=Z} - \left[-3\alpha\lambda_2\frac{\omega^2}{\emptyset} + \frac{2\lambda_3\alpha\omega}{\emptyset}\right]_{z=0}] dr + \int_0^Z \left[\lambda_2\frac{\partial D}{\partial\omega}\frac{\partial\omega}{\partial r} + \lambda_2\frac{D}{r} - \frac{\partial\lambda_2}{\partial r}D\right]_{r=R} dz\right] = 0 \quad (96)$$

The gradient correction $J_{T_{\text{int}}}$ was expressed in a finite-difference form along *r* and *z* directions to be utilized in the simulation. The values of differential changes are time-averaged before their usage for the gradient correction in (T_{int}) by the Broyden–Fletcher–Goldfarb–Shanno (BFGS) method. The iterative improvement in the value of (T_{int}) is given by:

$$T_{\text{int},i+1} = T_{\text{int},i} - \beta_i \,.\, J_{T_{\text{int}}} \tag{97}$$

where β_i is the optimal step length along the search direction in the i^{th} iteration determined by the BFGS algorithm.

4.5.1 The Gradient Improvement Method

A gradient method was adopted for the iterative solution of this optimal control problem. In more detail, the maximum local rate of increase in the value of a function with respect to its variables is in the direction to its gradient. This progress is called the steepest ascent direction. Equation (48) is used to set the search path to find the maximum of *J*.[48,49]

Quasi-Newton methods are the most favored of the methods that use a gradient of a function. These methods compute a search direction utilizing first order gradient information. Newton's methods make use of the second order information (Hessian matrix) of a function. Hessian matrix is calculated numerically, which involves a significant amount of computations.[48,49]

Quasi-Newton methods avoid the calculation of exact Hessian by generating approximate Hessian matrix using an appropriate updating technique. Among different Quasi-Newton methods, the BFGS method is consider as one of the most efficient method.[48,49] In more detail, BFGS method

is a computational algorithm to find an optimal solution for unconstrained nonlinear problems. It utilizes first order gradient information to generate the approximate Hessian matrix.[48]

4.6 The Optimal Control Algorithm

Figure 6 shows the schematic of the computational algorithm that was utilized to determine T_{int} versus time. Programmed in C++ language, the developed algorithm was implemented on Itanium 2/ Intel Itanium processor (64 bit, 1.5 GHz, 15.9 GB of RAM) with Intel C++ compiler.

Lastly, we reduced the computation time from 2 weeks to 5 days by scaling the dependent variables of the differential equations. The following are the steps of the computational algorithm, which improves [$T_{int}(t)$] in order to maximize J or I, i.e., oil production:

(i) Provide the initial guess for interface temperature function [$T_{int}(t)$] as vector of discrete values is the time domain, 0-t_f.

   a. Initial guess of T_{int} is very important, and it needs a considerable attention (Please see Section 5.2.3)

(ii) Integrate the mass, heat, and change of height equations, respectively, i.e., Equations (26), (30), and (34) use the initial and control function to obtain the values of state variables $T(t,r,z)$, $\omega(t,r,z)$, and $Z(t,r)$ at each node(t,r,z). Remember to save the values of state variables at the discretized points.

(iii) Evaluate the objective functional use the values of control functions, and state variables. Again save the objective functional value.

(iv) Integrate costate equations backward using final conditions, i.e., Equations (86), (88), and (90) using final condition, the control function, and saved values of state variables. Save the values of costate variables at the discretized point.

(v) Improve of [T_{int}(t)] by using the gradient correction [$J_{T_{int}}$(t)] given by Equation (95).

(vi) Repeat computation, and by updating T_{int}(t), until there is no further improvement in the objective functional value. At this point, the control function has reached its local optimal condition.

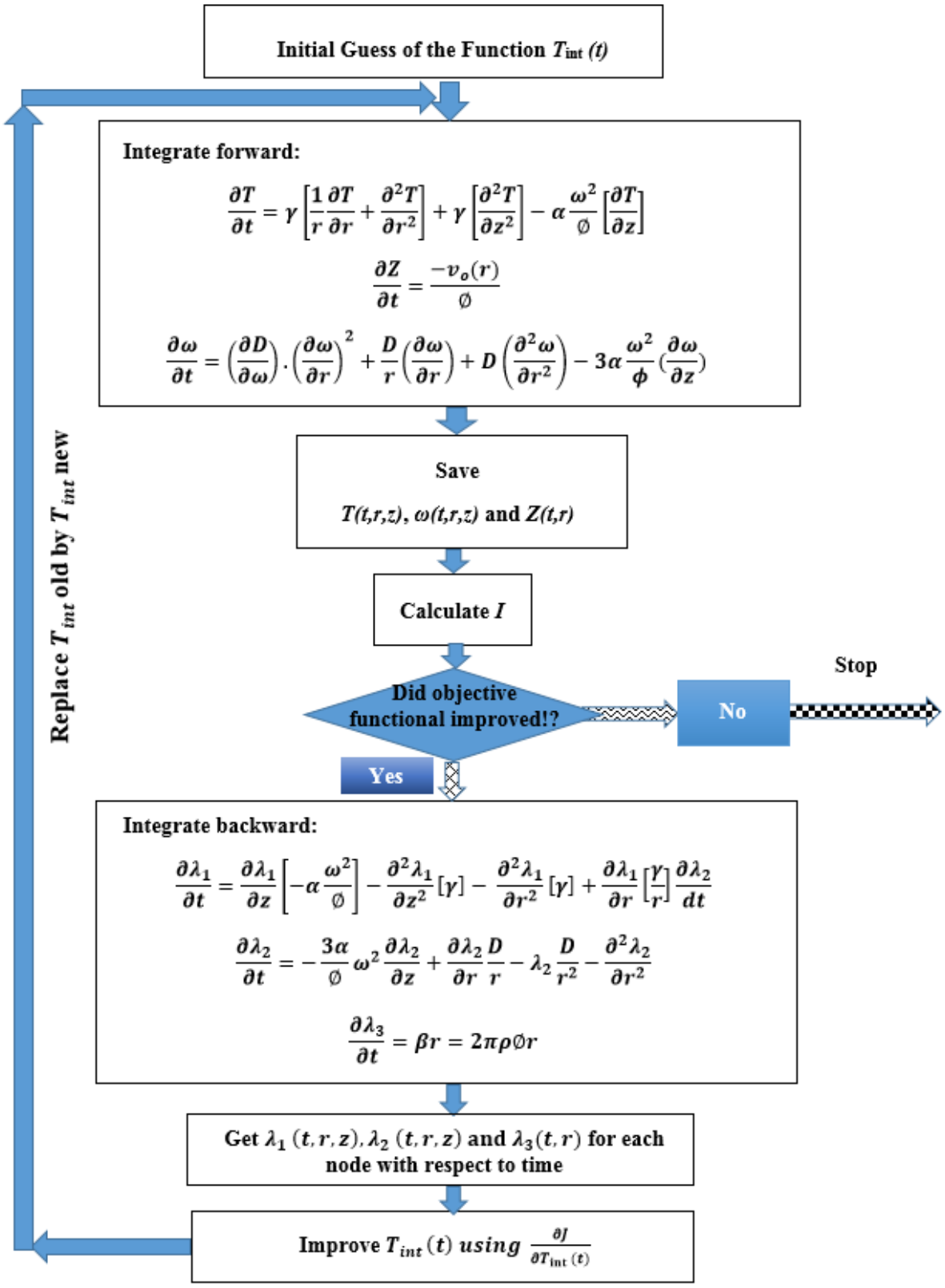

Figure 6: The Optimal Control Algorithm

4.7 Discretized Mathematical Model

Given that Equations (26), (30), and (34) are partial differential equations (PDEs), there finite-differenced forms along *r* and *z* directions were obtained, which were sets of ordinary differential equations (ODEs). As it can be seen in Figure 5, the cylindrical model is divided into equi-spaced grid points of numbers N_r and N_z, respectively, along the *r* and *z* directions. An adaptive step size control method is used in the algorithm to achieve the accuracy in the solution with minimum computational effort.[48,49]

4.7.1 Finite Difference for conversion of PDE to ODE for Heat Transfer

$$\frac{\partial T}{\partial t} = \gamma\left[\frac{1}{r}\frac{\partial T}{\partial r} + \frac{\partial^2 T}{\partial r^2}\right] + \gamma\left[\frac{\partial^2 T}{\partial z^2}\right] - \alpha\frac{\omega^2}{\emptyset}\left[\frac{\partial T}{\partial z}\right] \tag{34}$$

For Intermediate Grid Points:

for $0 < i < (N_i - 1)$ and $0 < j < (N_j - 1)$

$$\frac{\partial T_{i,j}}{\partial t} = (\gamma)\left[\frac{1}{r_i}\frac{T_{i+1,j} - T_{i-1,j}}{2\Delta r} + \frac{T_{i+1,j} - 2T_{i,j} + T_{i-1,j}}{\Delta r^2}\right] + \gamma\left[\frac{T_{i,j+1} - 2T_{i,j} + T_{i,j-1}}{\Delta z^2}\right] - \alpha\frac{\omega^2}{\emptyset}\left[\frac{T_{i,j+1} - T_{i,j-1}}{2\Delta z}\right] \tag{98}$$

For Axial Grid Points:

When $i = 0$ for $0 < j < (N_j - 1)$

$$\frac{\partial T_{0,j}}{\partial t} = \gamma\left[\frac{T_{0,j+1} - 2T_{0,j} + T_{0,j-1}}{\Delta z^2}\right] - \alpha\frac{\omega^2}{\emptyset}\left[\frac{T_{0,j+1} - T_{0,j-1}}{2\Delta z_i}\right] \tag{99}$$

When $i = 0$ and $j = 0$;

$$\frac{\partial T_{0,0}}{\partial t} = \gamma\left[\frac{T_{0,1} - 2T_{0,0} + T_{int}}{\Delta z^2}\right] - \alpha\frac{\omega^2}{\emptyset}\left[\frac{T_{0,1} - T_{\mathrm{int}}}{2\Delta z_0}\right] \tag{100}$$

When $i = 0$ and $j = (N_j\text{-}1)$

$$\frac{\partial T_{0,Nj-1}}{\partial t} = \gamma\left[\frac{T_{\mathrm{int}} - 2T_{0,Nj-1} + T_{0,Nj-2}}{\Delta z^2}\right] - \alpha\frac{\omega^2}{\emptyset}\left[\frac{T_{\mathrm{int}} - T_{0,Nj-2}}{2\Delta z_0}\right] \tag{101}$$

For Right Most Grid Points:

When $i = (N_i\text{-}1)$ and $j = 0$

$$\frac{\partial T_{Ni-1,0}}{\partial t} = (\gamma)\left[\frac{1}{r_{Ni-1}}\frac{T_{int}-T_{Ni-2,0}}{2\Delta r} + \frac{T_{(t)}-2T_{Ni-1,0}+T_{Ni-2,0}}{\Delta r^2}\right] + \delta\left[\frac{T_{Ni-1,1}-2T_{Ni-1,0}+T_{int}}{\Delta z^2}\right] - \alpha\frac{\omega^2}{\emptyset}\left[\frac{T_{Ni-1,1}-T_{int}}{2\Delta z_{Ni-1}}\right] \quad (102)$$

When $i = (N_i\text{-}1)$

$$\frac{\partial T_{Ni-1,j}}{\partial t} = (\gamma)\left[\frac{1}{r_{Ni-1}}\frac{T_{int}-T_{Ni-2,j}}{2\Delta r} + \frac{T_{(t)}-2T_{Ni-1,j}+T_{Ni-2,j}}{\Delta r^2}\right] + \gamma\left[\frac{T_{Ni-1,j+1}-2T_{Ni-1,j}+T_{Ni-1,j-1}}{\Delta z^2}\right] - \alpha\frac{\omega^2}{\emptyset}\left[\frac{T_{Ni-1,j+1}-T_{Ni-1,j-1}}{2\Delta z_{Ni-1}}\right] \quad (103)$$

When $i = (N_i\text{-}1)$ & $j = (N_j\text{-}1)$

$$\frac{\partial T_{Ni-1,Nj-1}}{\partial t} = (\gamma)\left[\frac{1}{r_{Ni-1}}\frac{T_{int}-T_{Ni-2,Nj-1}}{2\Delta r} + \frac{T_{int}-2T_{Ni-1,Nj-1}+T_{Ni-2,Nj-1}}{\Delta r^2}\right] + \gamma\left[\frac{T_{int}-2T_{Ni-1,nj-1}+T_{Ni-1,Nj-2}}{\Delta z^2}\right] - \alpha\frac{\omega^2}{\emptyset}\left[\frac{T_{int}-T_{Ni-1,Nj-2}}{2\Delta z_{Ni-1}}\right] \quad (104)$$

For Lower Most Intermediate Grid Points:

When $0<i<(N_r\text{-}1)$ and $j = 0$

$$\frac{\partial T_{i,0}}{\partial t} = (\gamma)\left[\frac{1}{r_i}\frac{T_{i+1,0}-T_{i-1,0}}{2\Delta r} + \frac{T_{i+1,0}-2T_{i,0}+T_{i-1,0}}{\Delta r^2}\right] + \gamma\left[\frac{T_{i,1}-2T_{i,0}+T_{int}}{\Delta z^2}\right] - \alpha\frac{\omega^2}{\emptyset}\left[\frac{T_{i,1}-T_{int}}{2\Delta z_i}\right] \quad (105)$$

For Upper Most Intermediate Grid Points:

When $0<i<(N_r\text{-}1)$ and $j = N_z\text{-}1$

$$\frac{\partial T_{i,Nj-1}}{\partial t} = (\gamma)\left[\frac{1}{r_i}\frac{T_{i+1,Nj-1}-T_{i-1,Nj-1}}{2\Delta r} + \frac{T_{i+1,Nj-1}-2T_{i,Nj-1}+T_{i-1,Nj-1}}{\Delta r^2}\right] + \gamma\left[\frac{T_{int}-2T_{i,Nj-1}+T_{i,Nj-2}}{\Delta z^2}\right] - \alpha\frac{\omega^2}{\emptyset}\left[\frac{T_{int}-T_{i,Nj-2}}{2\Delta z_i}\right] \quad (106)$$

where $T_{i,j}$ is the temperature of air at the node, *(i, j)* corresponding to the coordinate, *r* and *z*. The distance between grid points are Δr and Δz_i respectively along *r* and *z* directions. Δr is constant and given by:

$$\Delta r = \frac{R}{N_r}$$

But Δz_i varies with time along *r* direction, and is given by:

$$\Delta z_i = \frac{z_i}{N_z + 1}$$

4.7.2 The Costate Equations for Heat Transfer

The ordinary differential equations of costate equations for each corresponding grid point can be written as:

For Intermediate Grid Points:

for $0 < i < (N_i - 1)$ and $0 < j < (N_j - 1)$

$$\frac{\partial \lambda_{i,j}}{\partial t} = (\gamma)\left[\frac{1}{r_i}\frac{\lambda_{i+1,j}-\lambda_{i-1,j}}{2\Delta r} + \frac{\lambda_{i+1,j}-2\lambda_{i,j}+\lambda_{i-1,j}}{\Delta r^2}\right] + \gamma\left[\frac{\lambda_{i,j+1}-2\lambda_{i,j}+\lambda_{i,j-1}}{\Delta z^2}\right] - \alpha\frac{\omega^2}{\emptyset}\left[\frac{\lambda_{i,j+1}-\lambda_{i,j-1}}{2\Delta z}\right] \quad (107)$$

For Axial Grid Points:

When $i = 0$ for $0 < j < (N_j - 1)$

$$\frac{\partial \lambda_{0,j}}{\partial t} = 0 \quad (108)$$

When $i = 0$ and $j = 0$;

$$\frac{\partial \lambda_{0,0}}{\partial t} = 0 \quad (109)$$

When $i = 0$ and $j = (N_j\text{-}1)$

$$\frac{\partial \lambda_{0,\mathrm{Nj}-1}}{\partial t} = 0 \quad (110)$$

For Right Most Grid Points:

When $i = (N_i\text{-}1)$ and $j = 0$

$$\frac{\partial \lambda_{Ni-1,0}}{\partial t} = (\gamma)\left[\frac{1}{r_{Ni-1}}\frac{-\lambda_{Ni-2,0}}{2\Delta r} + \frac{-2\lambda_{Ni-1,0}+\lambda_{Ni-2,0}}{\Delta r^2}\right] + \gamma\left[\frac{\lambda_{Ni-1,1}-2\lambda_{Ni-1,0}}{\Delta z^2}\right] - \alpha\frac{\omega^2}{\emptyset}\left[\frac{\lambda_{Ni-1,1}}{2\Delta z_{Ni-1}}\right] \quad (111)$$

When i = (N_i-1)

$$\frac{\partial \lambda_{Ni-1,j}}{\partial t} = (\gamma)\left[\frac{1}{r_{Ni-1}}\frac{-\lambda_{Ni-2,j}}{2\Delta r} + \frac{-2\lambda_{Ni-1,j}+\lambda_{Ni-2,j}}{\Delta r^2}\right] + \gamma\left[\frac{\lambda_{Ni-1,j+1}-2\lambda_{Ni-1,j}+\lambda_{Ni-1,j-1}}{\Delta z^2}\right] - \alpha\frac{\omega^2}{\emptyset}\left[\frac{\lambda_{Ni-1,j+1}-\lambda_{Ni-1,j-1}}{2\Delta z_{Ni-1}}\right] \quad (112)$$

When i = (N_i-1) and j = (N_j-1)

$$\frac{\partial \lambda_{ni-1,nj-1}}{\partial t} = (\gamma)\left[\frac{1}{r_{Ni-1}}\frac{-\lambda_{Ni-2,Nj-1}}{2\Delta r} + \frac{-2\lambda_{Ni-1,Nj-1}+\lambda_{Ni-2,Nj-1}}{\Delta r^2}\right] + \gamma\left[\frac{-2\lambda_{Ni-1,Nj-1}+\lambda_{Ni-1,Nj-2}}{\Delta z^2}\right] - \alpha\frac{\omega^2}{\emptyset}\left[\frac{-\lambda_{Ni-1,Nj-2}}{2\Delta z_{Ni-1}}\right] \quad (113)$$

<u>For Lower Most Intermediate Grid Points:</u>

When 0<i<(N_r-1) and j = 0

$$\frac{\partial \lambda_{i,0}}{\partial t} = (\gamma)\left[\frac{1}{r_i}\frac{\lambda_{i+1,0}-\lambda_{i-1,0}}{2\Delta r} + \frac{\lambda_{i+1,0}-2\lambda_{i,0}+\lambda_{i-1,0}}{\Delta r^2}\right] + \gamma\left[\frac{\lambda_{i,1}-2\lambda_{i,0}}{\Delta z^2}\right] - \alpha\frac{\omega^2}{\emptyset}\left[\frac{\lambda_{i,1}}{2\Delta z_i}\right] \quad (114)$$

<u>For Upper Most Intermediate Grid Points:</u>

When 0<i<(N_r-1) and j = N_z-1

$$\frac{\partial \lambda_{i,Nj-1}}{\partial t} = (\gamma)\left[\frac{1}{r_i}\frac{\lambda_{i+1,Nj-1}-\lambda_{i-1,Nj-1}}{2\Delta r} + \frac{\lambda_{i+1,Nj-1}-2\lambda_{i,Nj-1}+\lambda_{i-1,Nj-1}}{\Delta r^2}\right] + \gamma\left[\frac{-2\lambda_{i,Nj-1}+\lambda_{i,Nj-2}}{\Delta z^2}\right] - \alpha\frac{\omega^2}{\emptyset}\left[\frac{-\lambda_{i,Nj-2}}{2\Delta z_i}\right] \quad (115)$$

4.7.3 Finite Difference for conversion of PDE to ODE for Mass Transfer

$$\frac{\partial \omega}{\partial t} = \left(\frac{\partial D}{\partial \omega}\right).\left(\frac{\partial \omega}{\partial r}\right)^2 + \frac{D}{r}\left(\frac{\partial \omega}{\partial r}\right) + D\left(\frac{\partial^2 \omega}{dr^2}\right) - 3\alpha\frac{\omega^2}{\phi}\left(\frac{\partial \omega}{\partial z}\right) \quad (26)$$

For Intermediate Grid Points:

for $0 < i < (N_i - 1)$ and $0 < j < (N_j - 1)$

$$\frac{\partial \omega_{i,j}}{\partial t} = D\left[\frac{1}{r_i}\frac{\omega_{i+1,j}-\omega_{i-1,j}}{2\Delta r} + \frac{\omega_{i+1,j}-2\omega_{i,j}+\omega_{i-1,j}}{\Delta r^2}\right] + \frac{\partial D}{\partial \omega}\left[\frac{\omega_{i+1,j}-\omega_{i-1,j}}{2\Delta r}\right]^2 - \frac{\alpha}{\emptyset}3{\omega_{i,j}}^2\left[\frac{\omega_{i,j+1}-\omega_{i,j-1}}{2\Delta z_i}\right] \quad (116)$$

For Axial Grid Points:

When i =0 and $0 < j < (N_j - 1)$

$$\frac{\partial \omega_{o,j}}{\partial t} = -\frac{\alpha}{\emptyset}3{\omega_{0,j}}^2\left[\frac{\omega_{0,j+1}-\omega_{0,j-1}}{2\Delta z_i}\right] \quad (117)$$

When i = 0 and j = 0

$$\frac{\partial \omega_{0,0}}{\partial t} = -\frac{\alpha}{\emptyset}3{\omega_{0,0}}^2\left[\frac{\omega_{0,1}-\omega_{int}}{2\Delta z_0}\right] \quad (118)$$

When i = 0 and j = (N_j-1)

$$\frac{\partial \omega_{0,Nj-1}}{\partial t} = -\frac{\alpha}{\emptyset}3{\omega_{0,Nj-1}}^2\left[\frac{\omega_{int}-\omega_{0,Nj-2}}{2\Delta z_0}\right] \quad (119)$$

For Right Most Grid Points:

When i = (N_i-1) and j = 0

$$\frac{\partial \omega_{Ni-1,0}}{\partial t} = D\left[\frac{1}{r_{Ni-1}}\frac{\omega_{int}-\omega_{Ni-2,0}}{2\Delta r} + \frac{\omega_{int}-2\omega_{Ni-1,0}+\omega_{Ni-2,0}}{\Delta r^2}\right] + \frac{\partial D}{\partial \omega}\left[\frac{\omega_{int}-\omega_{Ni-2,0}}{2\Delta r}\right]^2 - \frac{\alpha}{\emptyset}3{\omega_{Ni-1,0}}^2\left[\frac{\omega_{Ni-1,1}-\omega_{int}}{2\Delta z_{Ni-1}}\right] \quad (120)$$

When i = (N_i-1)

$$\frac{\partial \omega_{Ni-1,j}}{\partial t} = D\left[\frac{1}{r_{Ni-1}}\frac{\omega_{int}-\omega_{Ni-2,j}}{2\Delta r}+\frac{\omega_{int}-2\omega_{Ni-1,j}+\omega_{Ni-2,j}}{\Delta r^2}\right]+\frac{\partial D}{\partial \omega}\left[\frac{\omega_{int}-\omega_{Ni-2,j}}{2\Delta r}\right]^2 - \frac{\alpha}{\emptyset}3\omega_{Ni-1,j}{}^2\left[\frac{\omega_{Ni-1,j+1}-\omega_{ni-1,j-1}}{2\Delta z_{Ni-1}}\right] \quad (121)$$

When i = (N_i-1) and j = (N_j-1)

$$\frac{\partial \omega_{Ni-1,Nj-1}}{\partial t} = D\left[\frac{1}{r_{ni-1}}\frac{\omega_{int}-\omega_{Ni-2,Nj-1}}{2\Delta r}+\frac{\omega_{int}-2\omega_{Ni-1,Nj-1}+\omega_{Ni-2,Nj-1}}{\Delta r^2}\right]+\frac{\partial D}{\partial \omega}\left[\frac{\omega_{int}-\omega_{Ni-2,Nj-1}}{2\Delta r}\right]^2 - \frac{\alpha}{\emptyset}3\omega_{Ni-1,Nj-1}{}^2\left[\frac{\omega_{int}-\omega_{Ni-1,Nj-2}}{2\Delta z_{Ni-1}}\right] \quad (122)$$

<u>For Lower Most Intermediate Grid Points:</u>

When 0<i<(N_r-1) and j = 0

$$\frac{\partial \omega_{i,0}}{\partial t} = D\left[\frac{1}{r_i}\frac{\omega_{i+1,0}-\omega_{i-1,0}}{2\Delta r}+\frac{\omega_{i+1,0}-2\omega_{i,0}+\omega_{i-1,0}}{\Delta r^2}\right]+\frac{\partial D}{\partial \omega}\left[\frac{\omega_{i+1,0}-\omega_{i-1,0}}{2\Delta r}\right]^2 - \frac{\alpha}{\emptyset}3\omega_{i,0}{}^2\left[\frac{\omega_{i,1}-\omega_{int}}{2\Delta z_i}\right] \quad (123)$$

<u>For Upper Most Intermediate Grid Points:</u>

When 0<i<(N_r-1) and j = N_z-1

$$\frac{\partial \omega_{i,Nj-1}}{\partial t} = D\left[\frac{1}{r_i}\frac{\omega_{i+1,Nj-1}-\omega_{i-1,Nj-1}}{2\Delta r}+\frac{\omega_{i+1,Nj-1}-2\omega_{i,Nj-1}+\omega_{i-1,Nj-1}}{\Delta r^2}\right]+\frac{\partial D}{\partial \omega}\left[\frac{\omega_{i+1,Nj-1}-\omega_{i-1,Nj-1}}{2\Delta r}\right]^2 - \frac{\alpha}{\emptyset}3\omega_{i,Nj-1}{}^2\left[\frac{\omega_{int}-\omega_{i,Nj-2}}{2\Delta z_i}\right] \quad (124)$$

where $\omega_{i,j}$ is the mass fraction of atmospheric air at the node, *(i, j)* corresponding to the coordinate, *r* and *z*.

4.7.4 The Costate Mass Transfer Equations

The ordinary differential equations of costate equations written for the corresponding grid points are as follows:

For Intermediate Grid points:

for $0 < i < (N_i - 1)$ and $0 < j < (N_j - 1)$

$$\frac{\partial \lambda_{i,j}}{\partial t} = D\left[\frac{1}{r_i}\frac{\lambda_{i+1,j}-\lambda_{i-1,j}}{2\Delta r} - \frac{\lambda_{i+1,j}-2\lambda_{i,j}+\lambda_{i-1,j}}{\Delta r^2}\right] + D\left[\frac{\lambda_{i,j}}{r_i^2}\right] - \frac{\alpha}{\emptyset}3{\omega_{i,j}}^2\left[\frac{\lambda_{i,j+1}-\lambda_{i,j-1}}{2\Delta z_i}\right] \quad (125)$$

For Axial Grid Points:

When i =0 and $0 < j < (N_j - 1)$

$$\frac{\partial \lambda_{0,0}}{\partial t} = \frac{\partial \lambda_{0,j}}{\partial t} = \frac{\partial \lambda_{0,Nz-1}}{\partial t} = 0 \quad (126)$$

For the Right Most Grid Points:

When i = (N_i-1) and j = 0

$$\frac{\partial \lambda_{Ni-1,0}}{\partial t} = D\left[\frac{1}{r_{Ni-1}}\frac{-\lambda_{Ni-2,0}}{2\Delta r} - \frac{-2\lambda_{Ni-1,0}+\lambda_{Ni-2,0}}{\Delta r^2}\right] - D\left[\frac{\lambda_{Ni-1,0}}{r_{Ni-1}^2}\right] - \frac{\alpha}{\emptyset}3{\lambda_{Ni-1,0}}^2\left[\frac{\lambda_{Ni-1,1}}{2\Delta z_{Ni-1}}\right] \quad (127)$$

When i = (N_i-1) and $0 < j <$ *(N_z-1)*

$$\frac{\partial \lambda_{Ni-1,j}}{\partial t} = D\left[\frac{1}{r_{Ni-1}}\frac{-\lambda_{Ni-2,j}}{2\Delta r} - \frac{-2\lambda_{Ni-1,j}+\lambda_{Ni-2,j}}{\Delta r^2}\right] - D\left[\frac{\lambda_{Ni-1,0}}{r_{Ni-1}^2}\right] - \frac{\alpha}{\emptyset}3{\omega_{Ni-1,j}}^2\left[\frac{\lambda_{Ni-1,j}-\lambda_{Ni-1,j-1}}{2\Delta z_{Ni-1}}\right] \quad (128)$$

When i = (N_i-1) and j = (N_j-1)

$$\frac{\partial \lambda_{Ni-1,Nz-1}}{\partial t} = D\left[\frac{1}{r_{Ni-1}}\frac{-\lambda_{Ni-2,Nj-1}}{2\Delta r} - \frac{-2\lambda_{Ni-1,Nj-1}+\omega_{Ni-2,Nj-1}}{\Delta r^2}\right] - D\left[\frac{\lambda_{Ni-1,Nj-1}}{r_{Ni-1}^2}\right] -$$
$$\frac{\alpha}{\emptyset}3{\lambda_{Ni-1,Nj-1}}^2\left[\frac{-\lambda_{Ni-1,Nj-2}}{2\Delta z_{Ni-1}}\right] \quad (129)$$

For Lower Most Intermediate Grid Points:

When $0<i<$(N_r-1) and j = 0

$$\frac{\partial \lambda_{i,0}}{\partial t} = D\left[\frac{1}{r_i}\frac{\lambda_{i+1,0}-\lambda_{i-1,0}}{2\Delta r} + \frac{\lambda_{i+1,0}-2\lambda_{i,0}+\lambda_{i-1,0}}{\Delta r^2}\right] - D\left[\frac{\lambda_{i,0}}{r_i^2}\right] \quad -\frac{\alpha}{\emptyset}3{\lambda_{i,0}}^2\left[\frac{\lambda_{i,1}}{2\Delta z_i}\right] \tag{130}$$

For Upper Most Intermediate Grid Points:

When $0<i<(N_r\text{-}1)$ and $j = N_z\text{-}1$

$$\frac{\partial \lambda_{i,Nj-1}}{\partial t} = D\left[\frac{1}{r_i}\frac{\lambda_{i+1,Nj-1}-\lambda_{i-1,Nj-1}}{2\Delta r} + \frac{\lambda_{i+1,Nj-1}-2\lambda_{i,Nj-1}+\lambda_{i-1,Nj-1}}{\Delta r^2}\right] - D\left[\frac{\lambda_{i,Nj-1}}{r_i^2}\right] -$$
$$\frac{\alpha}{\emptyset}3{\lambda_{i,Nj-1}}^2\left[\frac{-\lambda_{i,Nj-2}}{2\Delta z_i}\right] \tag{131}$$

4.7.5 Change in Height of Physical Model

Change in the height of the physical model at any time instance was calculated by averaging the mass fraction value for the exposed nodes to solve gas at the bottom of the model.

The second set of ordinary differential equations were written as:

The change in height for $0 \leq i < (N_r\text{-}1)$ is given by:

$$\frac{\partial Z_i}{\partial t} = \frac{-v_{i,0}}{\emptyset} = -3\frac{\alpha}{\emptyset}\left[\frac{\omega_{i,0}-\omega_{i+1,0}+2\omega_{\text{int}}}{4}\right]^2 \tag{132}$$

For $i = N_r\text{-}1$

$$\frac{\partial Z_{Ni-1}}{\partial t} = \frac{-v_{Ni-1,0}}{\emptyset} = -3\frac{\alpha}{\emptyset}\left[\frac{\omega_{Ni-1,0}+3\omega_{int}}{4}\right]^2 \tag{133}$$

Chapter 5: Results and Discussion

This chapter presents the results obtained from the experiments carried out using the experimental setups. We examine the impact of permeability, pressure, and temperature of atmospheric air injection on heavy oil recovery. Next, the results obtained from the application of optimal control are assessed, and the optimal control policy is experimentally validated.

5.1 Preliminary Results

The sections below present the results of different experiments carried out to recover heavy oil from the physical reservoir models using atmospheric air injection. First, we did experiments with four different reservoir model permeabilities of 40, 87, 204 and 427 Darcy. Next, we performed experiments with four different pressures of 0.169, 0.286, 0.403 and 0.514 MPa absolute at 25^{o}C and with 204 Darcy model permeability. Lastly, we did experiments with various air temperatures in the range 25-90^{o}C with (i) constant air temperature, and (ii) periodic air temperature variations with time. The maximum temperature of the air was 90^{o}C in the experiments. No chemical reaction took place in the experiments according to the analysis of effluent air, reservoir model temperature, and live oil viscosity (please see Section 5.1.5). We have also carried experiments using injection of pure nitrogen gas (please see Appendix C-F)

5.1.1 Effect of Permeability on Heavy Oil Recovery

To determine the effect of permeability on oil recovery, experiments were carried out at air temperature and pressure of 25^{o}C and 0.514 MPa, respectively, and different permeability values of 40, 87, 204, and 427 Darcy. The results are shown in Figure 7. It is observed that the recovery increases with permeability. This result is in close agreement with what is reported in the

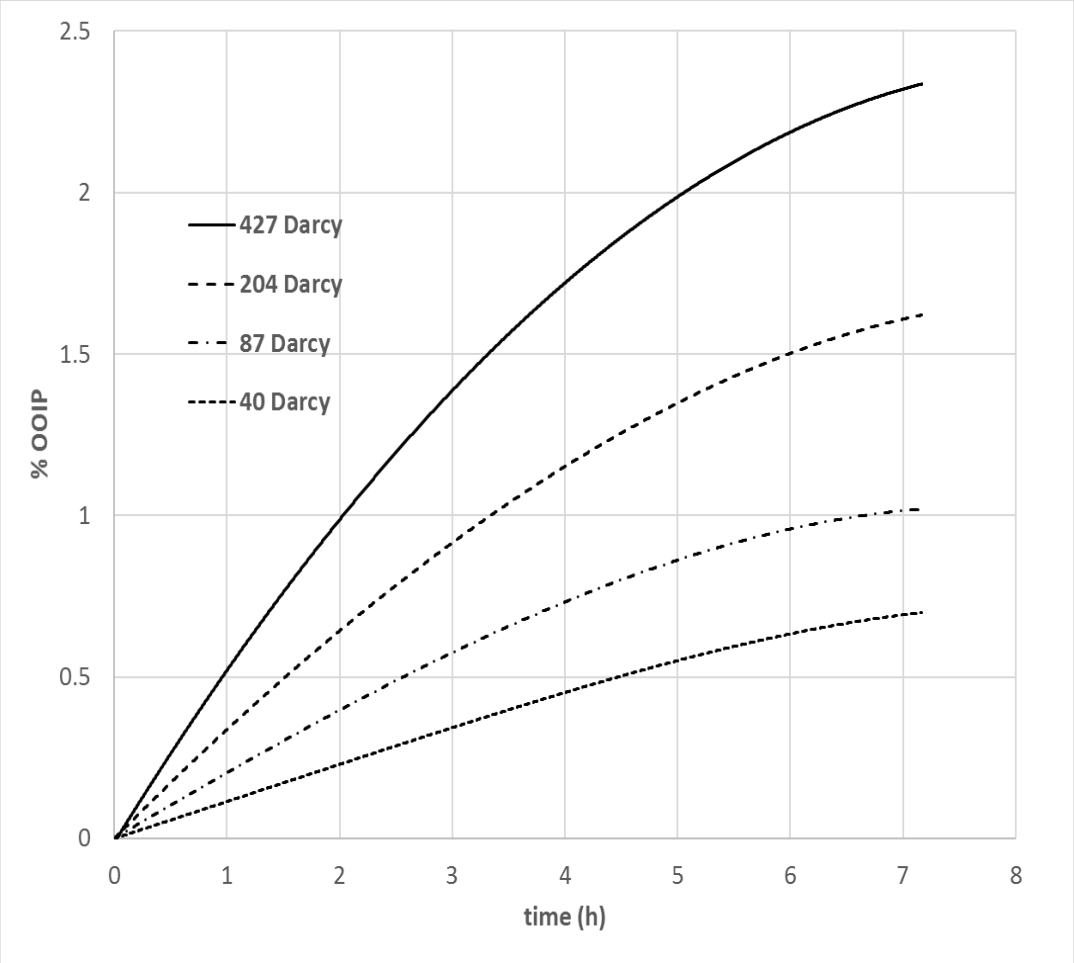

Figure 7: Oil recovery of air injection versus time for different permeabilities at 0.514 MPa absolute and 25ºC.

literature[52,53] and is attributed to the fact that the diluted oil can drain due to gravity more easily through the physical model of higher permeability.[26] The overall oil recovery in these experiments was found to increase from 0.70 to 2.33% of the OOIP as the permeability increased from 40 to 427 Darcy. Furthermore, the correlation between the production rate and permeability is shown in Figure 8 with the r^2 value of 0.9995. The production rate [$\dot{m}\times10^3$(gram/min)] and the physical model permeability K (Darcy) is given by the following equation:

$$\dot{m} = 0.5251K^{0.5133} \tag{134}$$

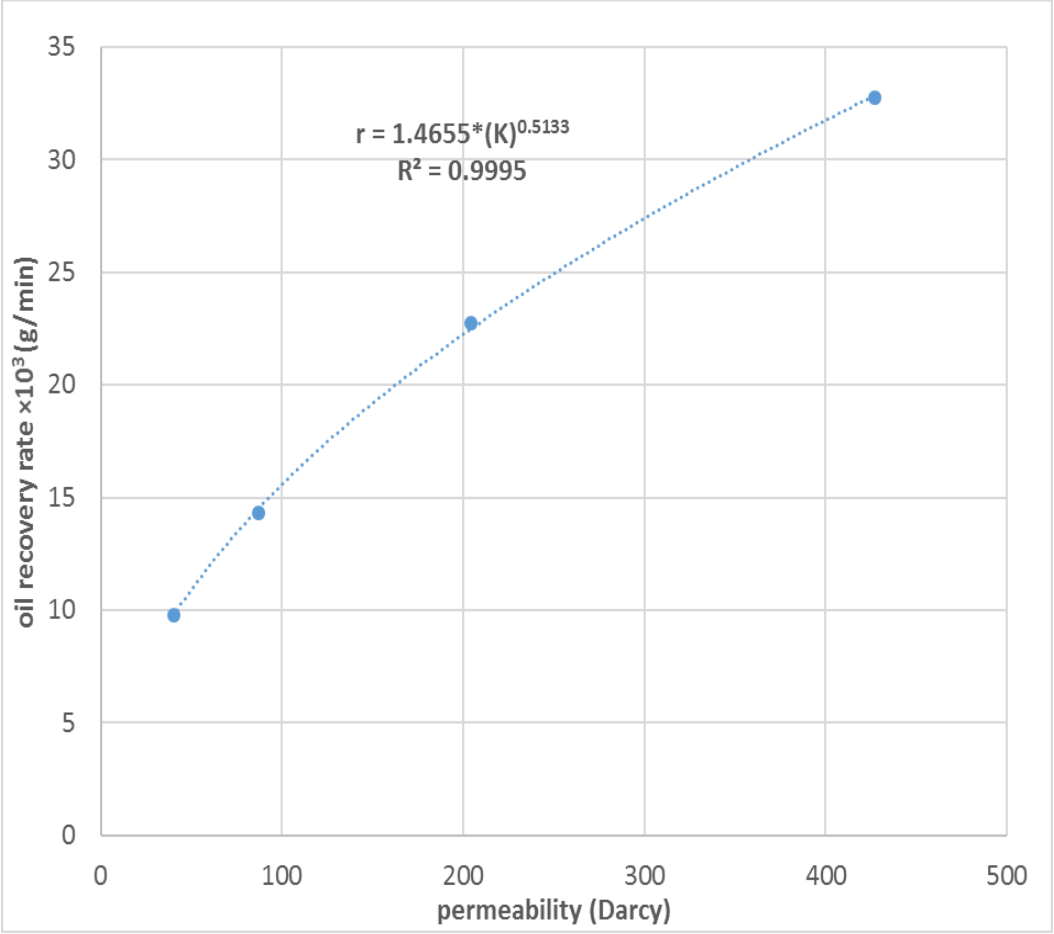

Figure 8: Variation of production rate of air injection with model permeability at 0.514 MPa absolute and 25°C

It is observed that the correlation between heavy oil production rate and the physical model permeability is neatly fitted by the power function. This result is in close agreement with what is reported in the literature.[52,53]

5.1.2 Effect of Pressure on Heavy Oil Recovery

Figure 9 shows the effect of air pressure on heavy oil recovery at a constant air temperature of 25ºC and 204 Darcy model permeability. The results show that the heavy oil recovery increased with air pressure. The overall oil recovery rose from 0.77% to 1.60% of the OOIP as pressure was

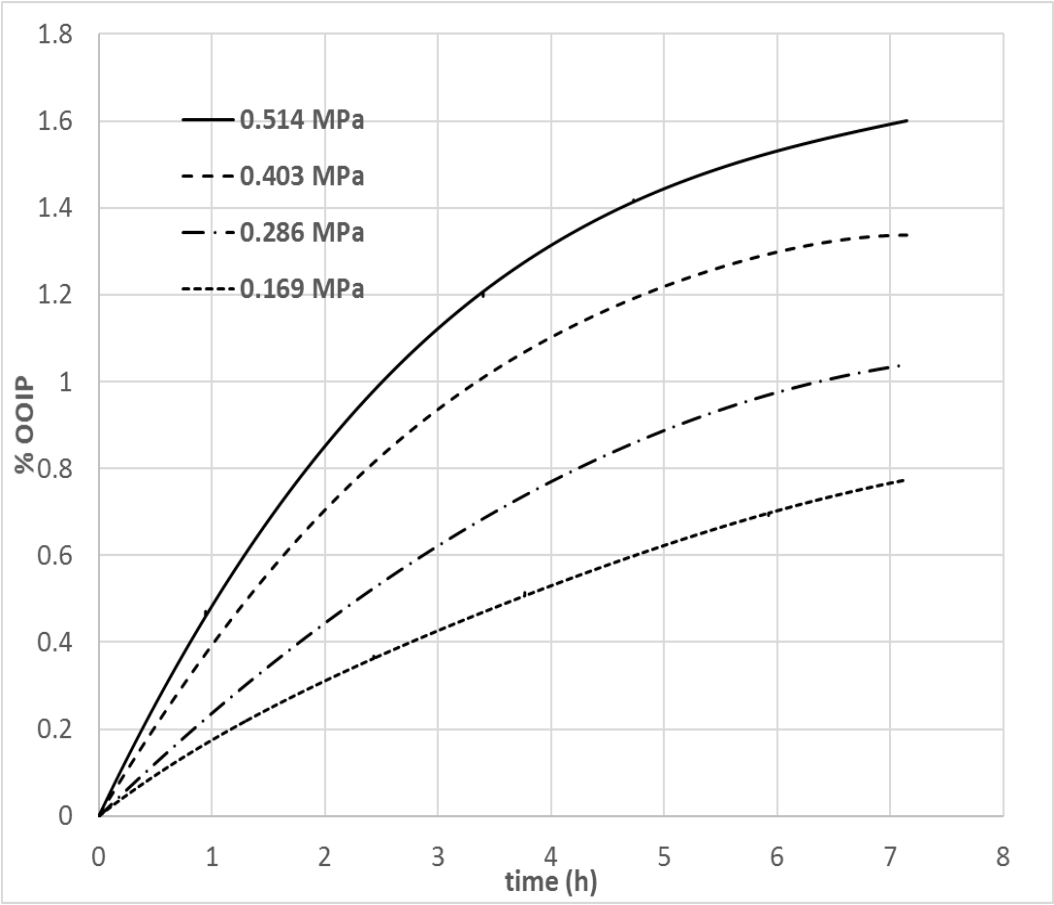

Figure 9: Oil recovery versus time at 25ºC air temperature, 204 Darcy model permeability, and different air pressures (absolute)

increased from 0.169 to 0.514 MPa absolute. The likely reason is the increase in the solubility of the injected air in heavy oil with pressure. It may be noted that the higher proportion of the air in the oil reduces the oil viscosity and facilitates its drainage from the reservoir.

A similar experiment was conducted by using propane as a solvent and found that the oil recovery increased with pressure.[50] Table 7 shows that the mass fraction of air dissolved in the heavy oil increased with pressure.

Table 7: Dissolved air in heavy oil at constant temperature (25°C) and different pressures

pressure (MPa absolute)	**dead oil mass** (g)	**collected air mass** (g)	**dissolved air mass fraction**
0.169	4.6710	0.035010	0.0074370
0.286	6.2632	0.064030	0.010115
0.403	8.0610	0.10601	0.012979
0.514	9.6402	0.15302	0.015620

5.1.3 Effect of Temperature on Oil Recovery

To evaluate the impact of temperature on heavy oil recovery, we performed a number of experiments keeping the air temperature **(i)** constant, and **(ii)** periodically varying with time.

5.1.3.1 Effect of Air Temperature in Isothermal Experiments

Four experiments were carried out at constant air temperatures of 25, 50, 75 and 90°C at 0.514 MPa absolute air pressure with 204 Darcy permeability of the physical model. The results shown in Figure 10 indicate that the final oil recovery increased with temperature to a maximum of 41.2% of the OOIP at 90°C.

Apart from the decrease in the oil viscosity with temperature, the increase in the oil recovery may be attributed to the increase in the diffusivity of air (mostly nitrogen) in heavy oil with

temperature.[19] Higher diffusivity causes greater uptake of air in the oil and brings about a considerable reduction in the oil viscosity,[55] which promotes oil recovery. The phenomenon mentioned above is supported by the data in Table 8. According to the table, the increase in temperature from 25°C to 90°C and the associated increase in the amount of dissolved air bring

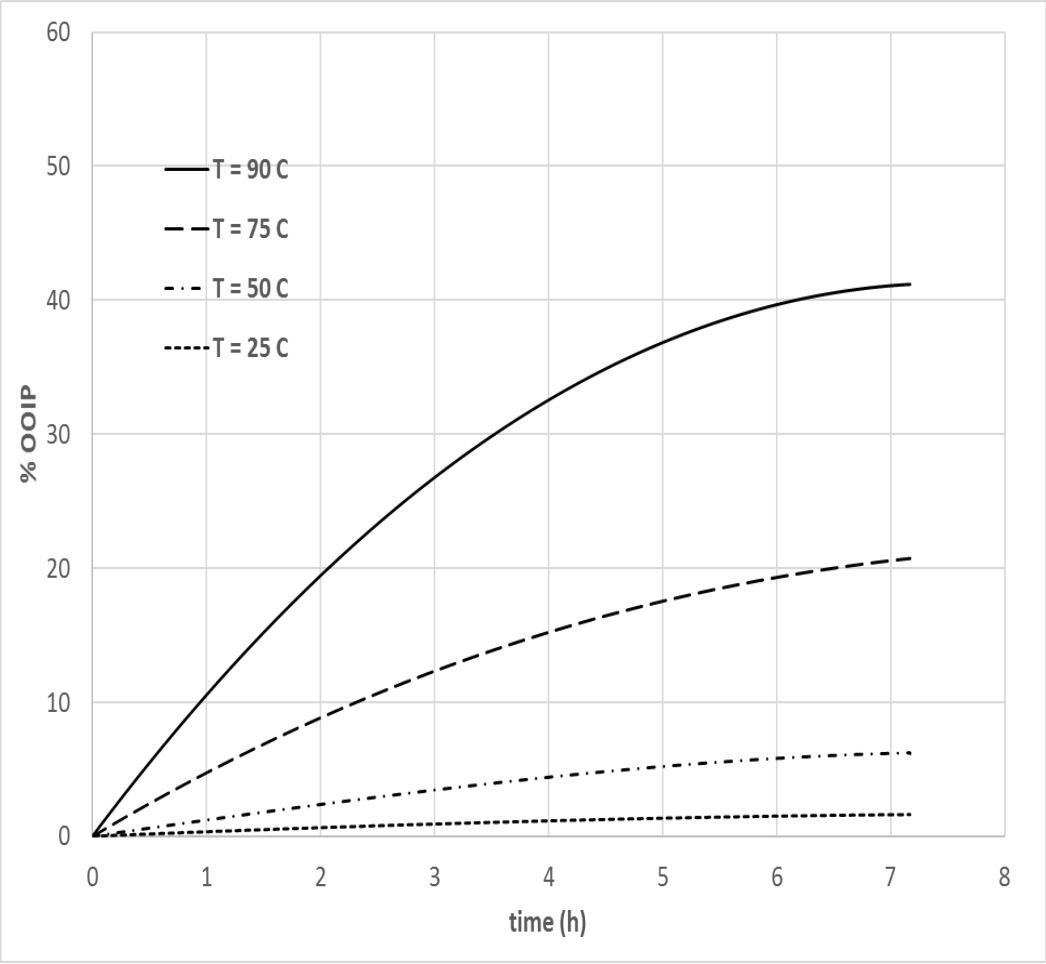

Figure 10: Oil recovery versus time at 0.514 MPa absolute air pressure, 204 Darcy model permeability, and different air temperatures

Table 8: Live oil viscosity and dissolved air fraction in oil at constant pressure of 0.514 MPa and different temperatures

temperature (^{o}C)	**viscosity** (mPa.s)	**dissolved air mass fraction**
25	11,500.00	0.015601
50	642.00	0.061102
75	86.800	0.166030
90	11.200	0.463010

about considerable viscosity reduction from 11,500 to 11.2 mPa.s. The oil viscosity is related to the dissolved air mass fraction as (Figure 11):

$$\mu = 2.2451(\omega)^{-2.0} \quad (135)$$

with the r^2 value of 0.9998. A similar trend has been reported earlier for the dissolution of nitrogen and carbon dioxide in heavy oil.[55] This correlation is used in the modeling simulation in this study.

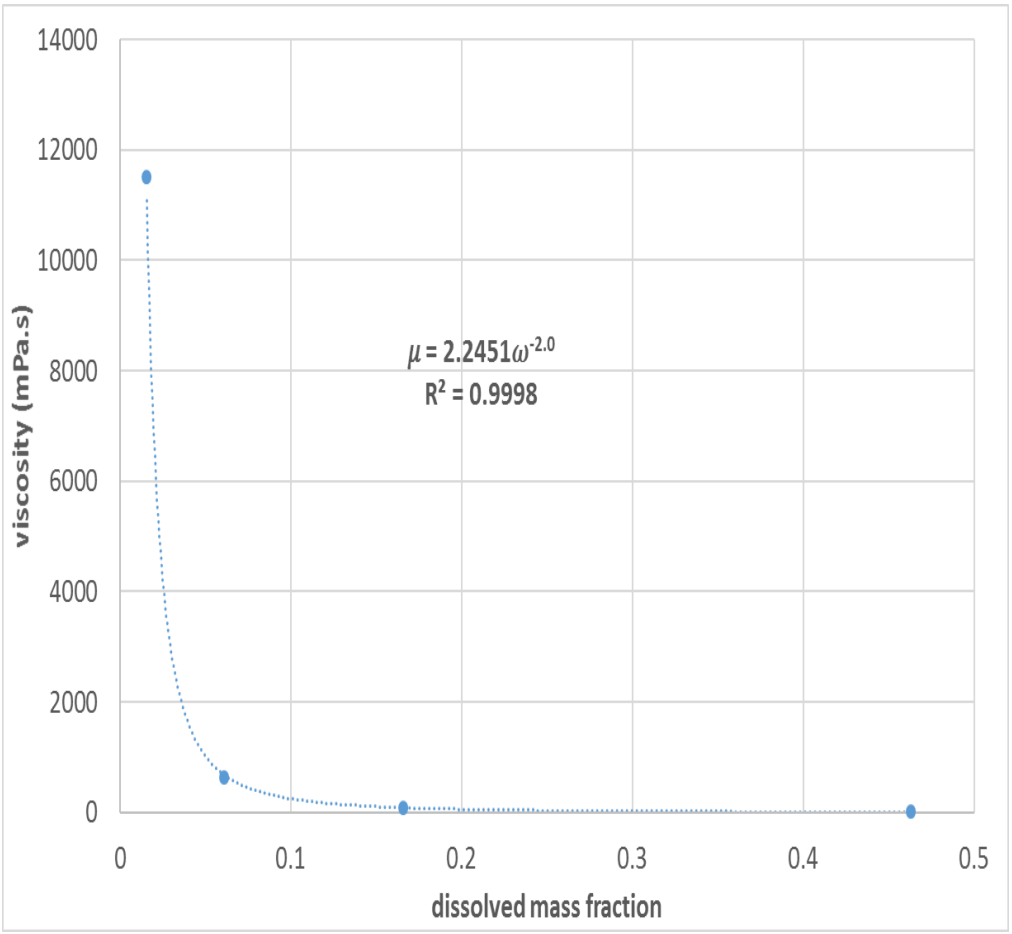

Figure 11: Correlation between viscosity and dissolved air mass fraction at 0.514 MPa absolute and 204 Darcy permeability of the physical model

A comparison of Figures 9 and 10 shows that the increase in air temperature is significantly more conducive to heavy oil recovery than the increase in air pressure. This may be explained by the mass fraction of air found in the produced oil as listed in Tables 7 and 8, respectively, for different pressures and temperatures.

The rise in the dissolved air mass fraction is steeper with temperature than pressure. While the maximum value of the dissolved air mass fraction is 0.0156 at the maximum pressure, that value at the maximum temperature is 0.463, which is about 30 times higher. The larger amount of air in

the oil helps to reduce its viscosity to a greater extent and thus enhances its recovery. In addition to reducing the oil viscosity, the increase in temperature is expected to cause the gas-oil mixture to expand and help improve the oil recovery further.[3,14]

5.1.3.2 Effect of Variation in the Air Temperature

To study the effect of variation in the air temperature with time on oil recovery, we performed experiments with periodic variation of air temperature between 50°C and 90°C. Figure 12 shows oil recovery at a constant air temperature of 90°C as well as with the periodic temperature variation having an average of 67°C.

As seen from the figure, the periodic variation of air temperature enhances the recovery in comparison to constant air temperature (90°C) by 8% with the final recovery of 44.5% of the OOIP. Compared to the recovery with constant air temperature, the recovery with the periodic air temperature variation is lower initially but eventually surpasses the former after six h at a "cross-over point" as shown in the figure.

To further examine the impact of the periodic temperature variations with a higher minimum temperature, we performed experiments with periodic variation of air temperature between 75°C and 90°C as shown in Figure 13. As observed from the figure, in comparison to constant air temperature, the periodic air temperature variation enhanced oil recovery even more by 17.6% with the final value of 48.4% of the OOIP.

It is interesting to note that the oil recovery corresponding to the periodic air temperature crossed over the constant temperature curve at a much earlier time (about four h earlier) than that in Figure 12. This may be attributed to the overall higher average air temperature of 78^{o}C in Figure 13 compared to 67^{o}C in Figure 12.

The increase in oil recovery with periodic air temperature may be ascribed to the corresponding periodic change in surface temperature of the physical model and the associated periodic reversal in the temperature gradient as well as the concentration gradient of air (through similar diffusivity and solubility changes[19,42]) within the model. This alteration of gradients boosts dispersion and leads to better mixing of air with the oil, thereby promoting its recovery.[42]

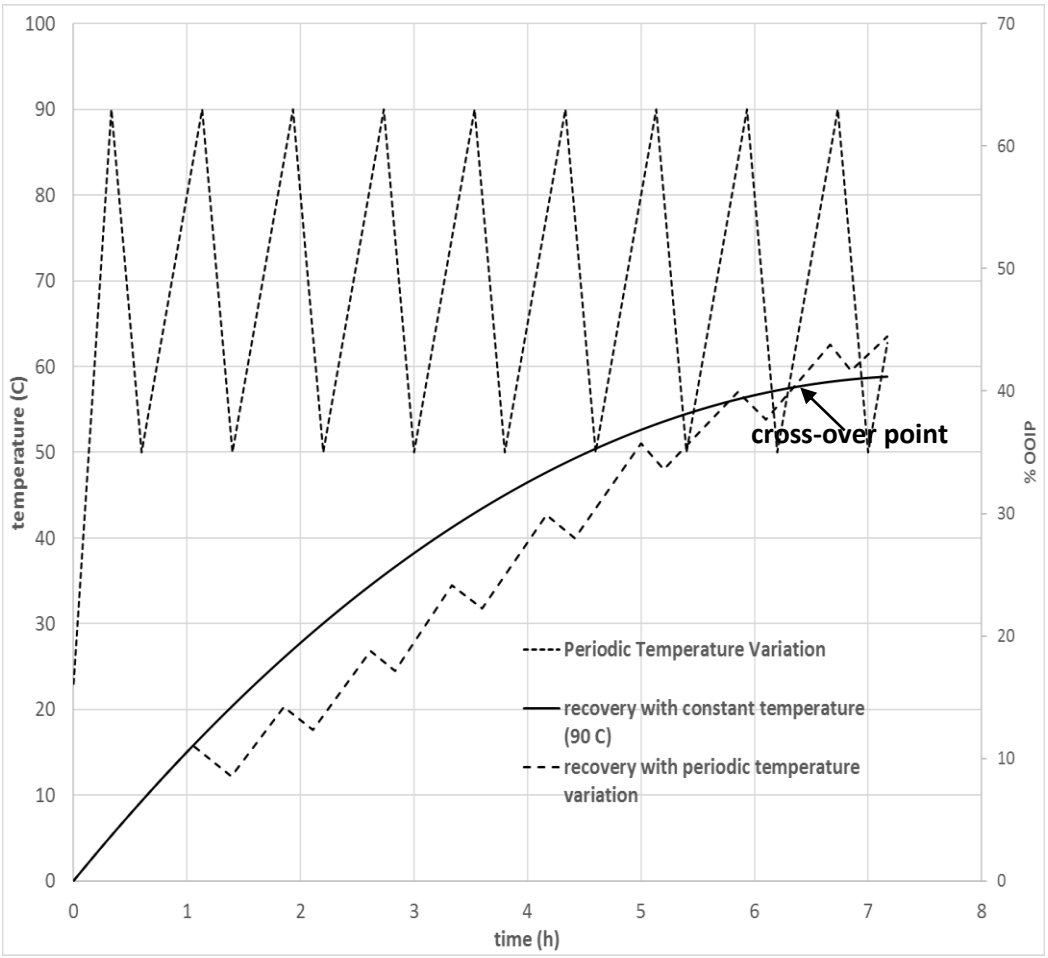

Figure 12: Oil recovery versus time at 0.514 MPa absolute air pressure, 204 Darcy model permeability, and constant (90^{o}C) as well as periodically varying air temperature in the range, 50-90^{o}C.

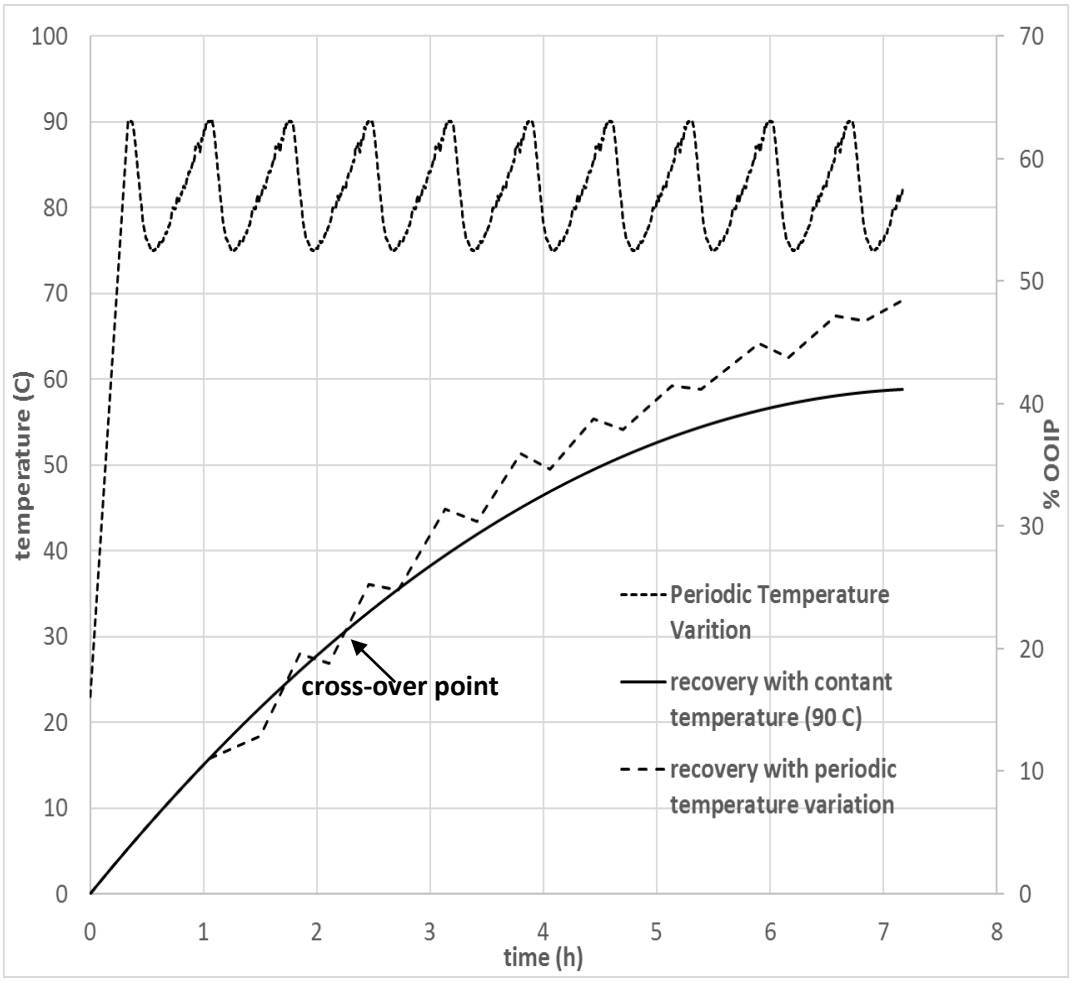

Figure 13: Oil recovery versus time at 0.514 MPa absolute air pressure, 204 Darcy model permeability, and constant (90^{o}C) as well as periodically varying air temperature in the range, 75-90^{o}C

It is important to note that to enable a better understanding of the impact of periodic temperature variation on heavy oil recovery, instantaneous recovery is plotted against cumulative recovery at the constant temperature of 90^{o}C in Figures 12 and 13.

5.1.4 Effect of Varying Temperature with Different Permeabilities

The effect of periodic temperature variations between 75^{o}C to 90^{o}C on oil recovery was examined for different permeability values of 40, 87 and 427 Darcy. Figures 14-16 show the oil recovery

versus time with periodic air temperature variations compared to a constant temperature (90°C) at different physical model permeability. The results indicate that in all experiments, the oil recovery increased in periodic temperature variations compared to that at the constant temperature. As the permeability rose from 40 to 427 Darcy, the OOIP improved from 14.8% to 18.6%, to the

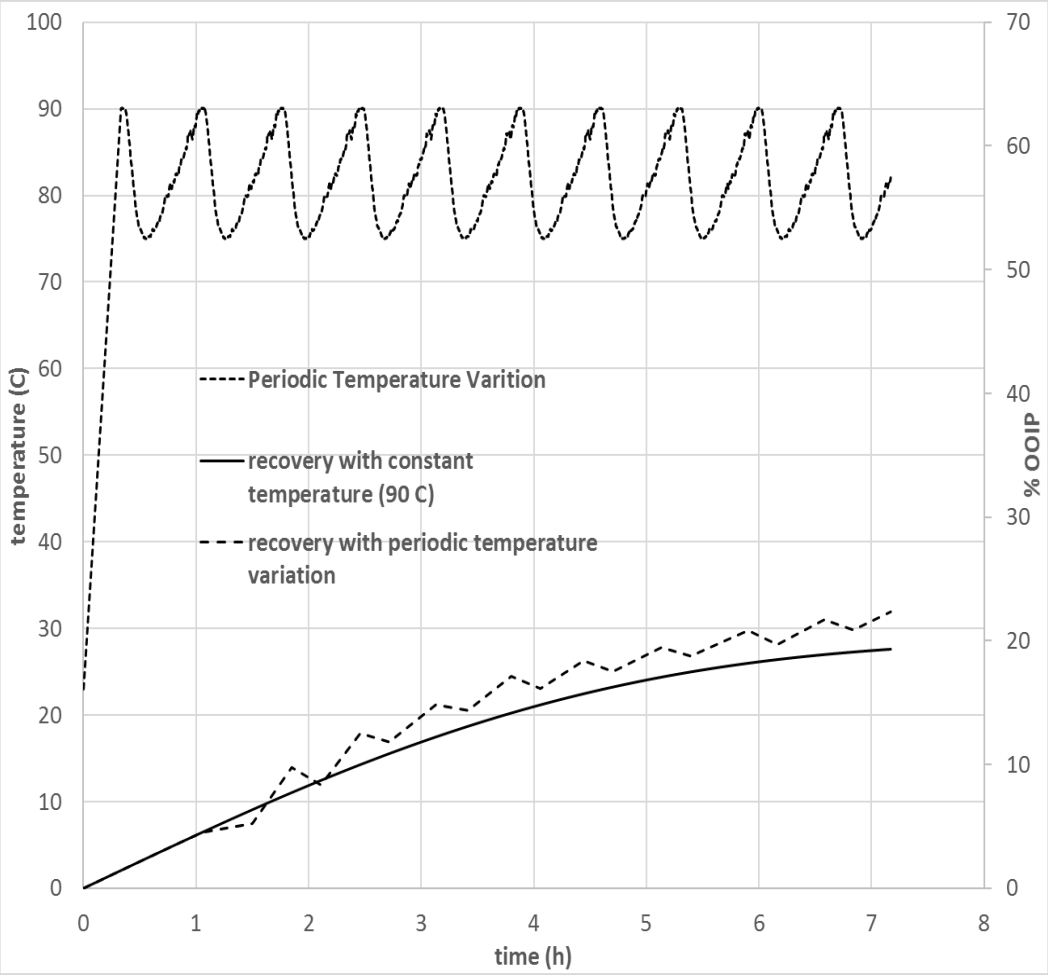

Figure 14: Oil recovery versus time at 0.514 MPa absolute air pressure, constant (90°C) as well as periodically varying air temperature in the range, 75-90°C, and 40 Darcy model permeability

maximum of 69.1% OOIP. The oil recovery curves corresponding to periodic temperatures are observed to cross over the constant temperature oil recovery curves at about 2.2 h, i.e. after one full cycle of temperature variation with time.

Even though the permeability of the physical model increased tremendously, the oil recovery increased marginally. These results indicate that periodic temperature variation has a significantly influence on oil recovery than permeability.

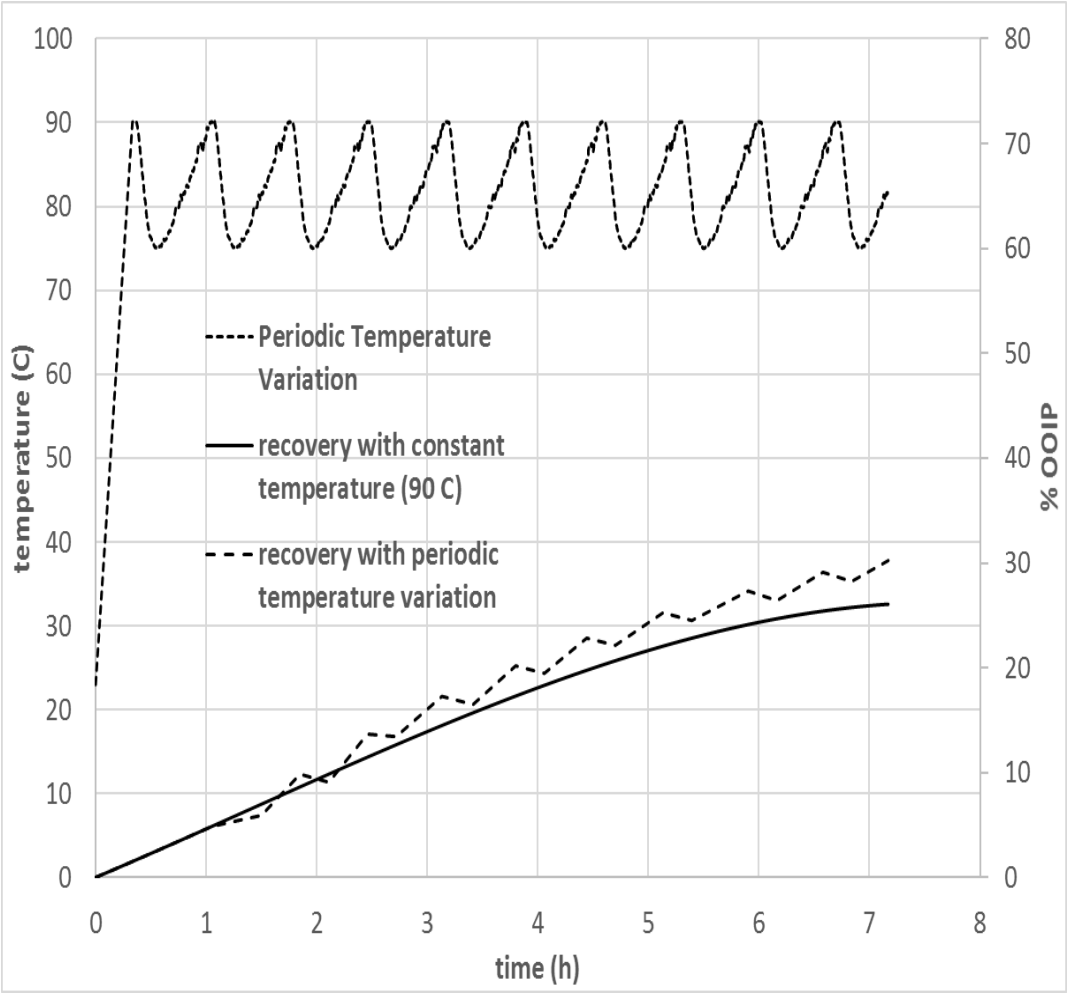

Figure 15: Oil recovery versus time at 0.514 MPa absolute air pressure, constant (90^{o}C) as well as periodically varying air temperature in the range, 75-90^{o}C, and 87 Darcy model permeability

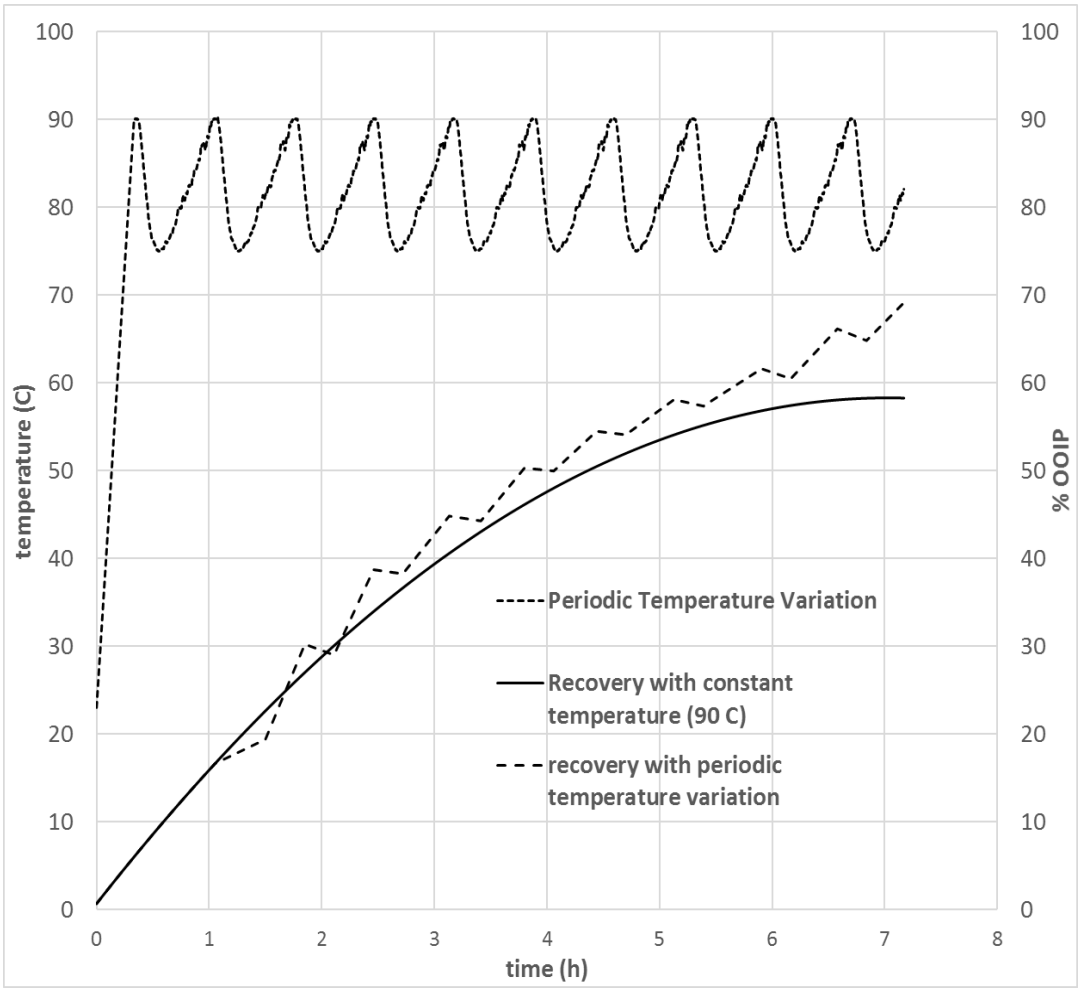

Figure 16: Oil recovery versus time at 0.514 MPa absolute air pressure, constant (90^{o}C) as well as periodically varying air temperature in the range, 75-90^{o}C, and 427 Darcy model permeability

In summary, the results above indicate that the heavy oil recovery up to 69.1% of the OOIP can be achieved by utilizing freely available air under moderate temperature and pressure conditions in a non-reactive environment. The results at 0.514 MPa air pressure show a considerable improvement in heavy oil recovery from 1.6% of the OOIP at 25^{o}C air temperature to 69.1% of the OOIP with the periodic variation of air temperature between 75^{o}C and 90^{o}C.

These findings are therefore very promising for heavy oil recovery using freely available air at low temperatures and pressures.

5.1.5 Absence of Chemical Reactions

As previously mentioned, oxygen in the air reacts with hydrocarbons during in-situ combustion and generates carbon dioxide, water, and energy. To determine whether any reaction took place during the experiments of this study, we analyzed several gas effluent samples (using Perkin Elmer GCMS/TCD equipment for gas analysis) from experiments carried out at different constant temperatures, 0.514 MPa absolute air pressure with 204 Darcy permeability of the physical model. In all cases, the air composition was found to be the same as that of the fresh air. Table 9 presents the air composition for the experiment at 90^{o}C. Furthermore, no sudden increase in the reservoir temperature was observed throughout the experiments. Lastly, the viscosity of the live oil decreased with temperature. As a result, it may be concluded that no chemical reactions occurred in the experiments done in this study. Lastly, the percentage errors between the component of air analysis from the repeated experiments were found to be in the range of 0.2-0.5%.

Table 9: Analysis of air for the experiment done at 90^{o}C

Component of air	**mass fraction**	
	fresh air	**effluent air**
oxygen	0.21201	0.21201
nitrogen	0.77502	0.77502
carbon dioxide	4.6011×10^{-4}	4.6011×10^{-4}

Until now, we have proved the concept that the heavy oil recovery can be achieved by utilizing freely available air under moderate temperature and pressure conditions in a non-reactive environment. In the following sections, the results of an extensive simulation study of atmospheric air injection will be described and discussed.

5.2 Optimal Control Results

One of the primary objectives of this study is to formally develop and utilize a tool to obtain optimal control policy. As mentioned earlier, experiments were conducted using laboratory-scale physical model at different pressures (0.169, 0.286, 0.403 and 0.514 MPa absolute) and temperatures in the range, 25-90^{o}C. Reservoirs of four different permeabilities (40, 87, 204, and 427 Darcy) are used in the experiments.

In this computational simulation, some parameters were measured experimentally, such as live oil viscosity, live oil density, the interfacial air temperature, and the interfacial mass fraction to increase the confidence in the results of the computational simulation.

5.2.1 Execution and Formalization of the Concept

To formalize the concept that the variation of air interfacial temperature versus time enhances the heavy oil recovery in our lab-scale system, we needed to accomplish the following steps:

1. theoretically determine optimal policy for air interfacial temperature versus time, which maximize heavy oil recovery
2. experimentally validate the optimal policy

It is important to note that the first step requires the knowledge on the correlation between dispersion coefficient and concentration and temperature that is used in the mathematical model of the process.

5.2.2 Determination of Dispersion Coefficient

As previously mentioned, the gas dispersion coefficient is an important property used in the mathematical model utilized in the optimal control of gas EOR. The dispersion coefficient of air was determined using the technique developed earlier. This technique uses optimal control to determine optimal solvent dispersion versus concentration function.[46]

The optimal [$D(\omega,T)$] of atmospheric air is plotted in Figure 17 at the injection pressure of 0.514 MPa, temperature of 25^{o}C, and physical model permeability of 204 Darcy. It shows that the optimally determined [$D(\omega,T)$] rises to a maximum value, and then drops toward the end. The highest value of atmospheric air dispersion is 2.5310×10^{-5} (m^2/s) at the corresponding air mass fraction of 0.33600.

It is observed that the calculated dispersion value is about 37.47% lower compared to that with propane.[46] This is due to the fact that propane has a higher diffusivity in comparison to atmospheric air, but this is still very encouraging given that air is freely available while hydrocarbon solvents, such as propane are costly and their use for oil recovery is almost impractical at present.

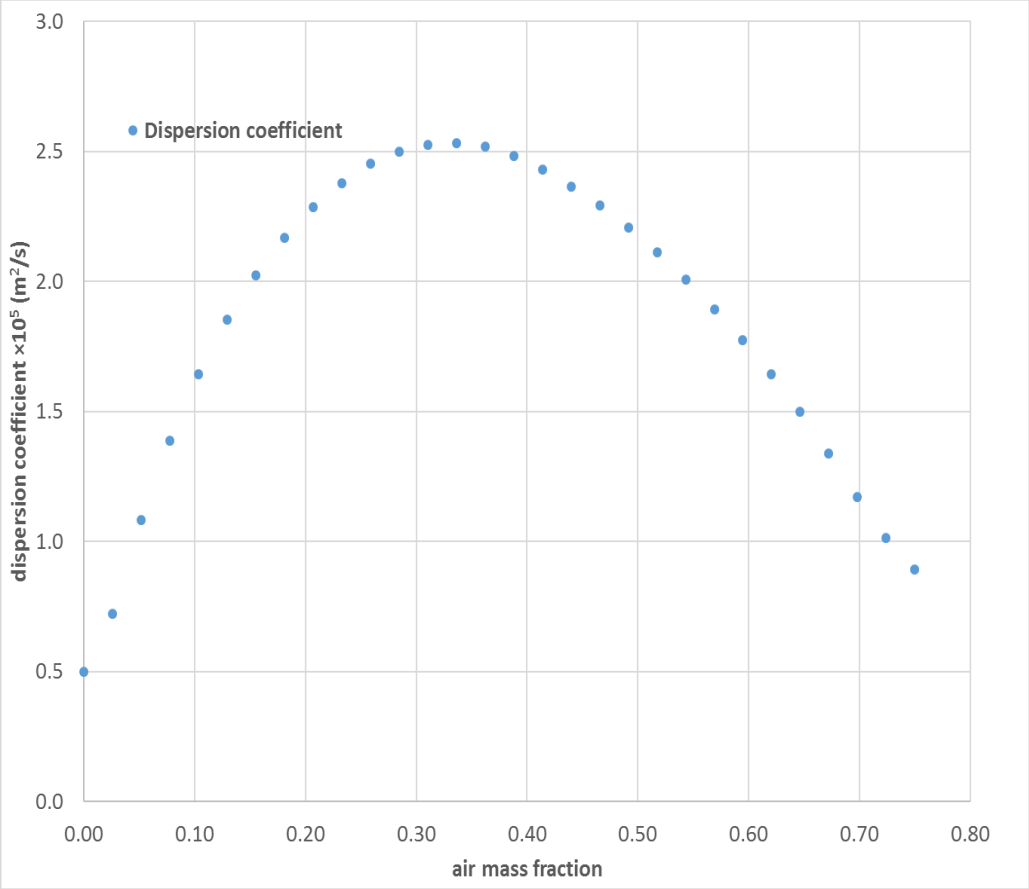

Figure 17: Dispersion coefficient function of air injection in heavy oil (Pressure 0.514 MPa; Temperature 25^{o}C; Permeability 204 Darcy)

The change in optimal dispersion coefficient with air mass fraction may be due to the fact that initially when higher concentration gradients are present in the heavy oil, the dispersion of air molecules is higher. It decreases later on with a gradual reduction in the concentration gradients as more and more air molecules enter the porous medium because of dispersion. When this happens, the motion of air molecules is restricted by their abundance, thus decreasing the overall air dispersive flux. When the air diffusion flux and the convective flux are at their maximum, the dispersion coefficient value gains the highest value. Thus, at some intermediate stage, the dispersion coefficient is at its maximum.[49]

Moreover, under the set operational conditions, the objective functional decreased monotonically to the minimum as shown in Figure 18. The change was significant at the beginning, but the rate of improvement slowed down at final iterations. The final optimal function [$D(\omega,T)$] was obtained in 31 iterations after which no further increase was observed.

We also determined the dispersion coefficient at different air temperatures of 50^{o}C, 75^{o}C, and 90^{o}C. Figure 19 shows the optimally obtained dispersion coefficient of atmospheric air at different temperatures of 25^{o}C, 50^{o}C, 75^{o}C, and 90^{o}C. Similar to Figure 17, the value of [$D(\omega,T)$] with respect to 50^{o}C, 75^{o}C, and 90^{o}C increase to a maximum value, and then drops toward the end. Lastly, the plot of maximum dispersion coefficient at different temperatures is shown in Figure 20.

It is important to note that the optimal dispersion coefficient values at different temperatures were used to compute the optimal control policy for atmospheric air injection versus time in this process.

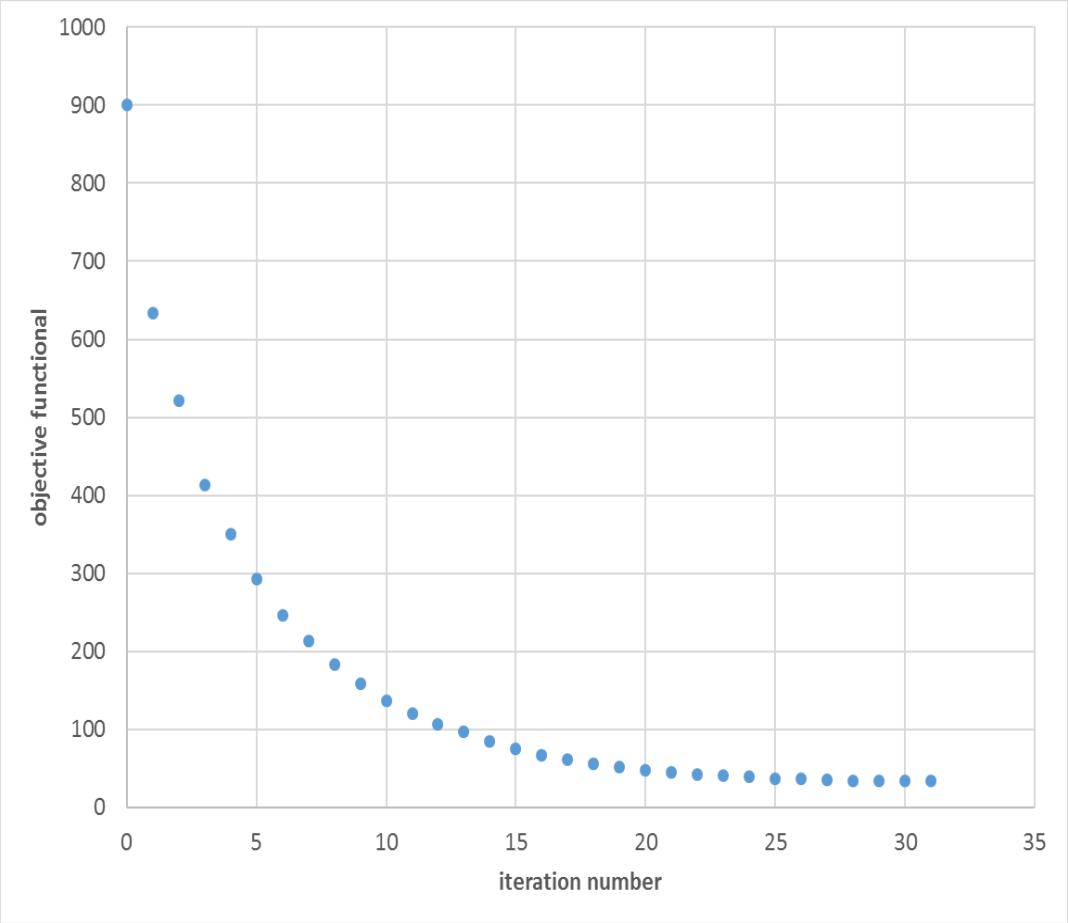

Figure 18: Objective functional versus iteration number for dispersion coefficient at air pressure 0.514 MPa, temperature 25^{o}C, and permeability 204 Darcy

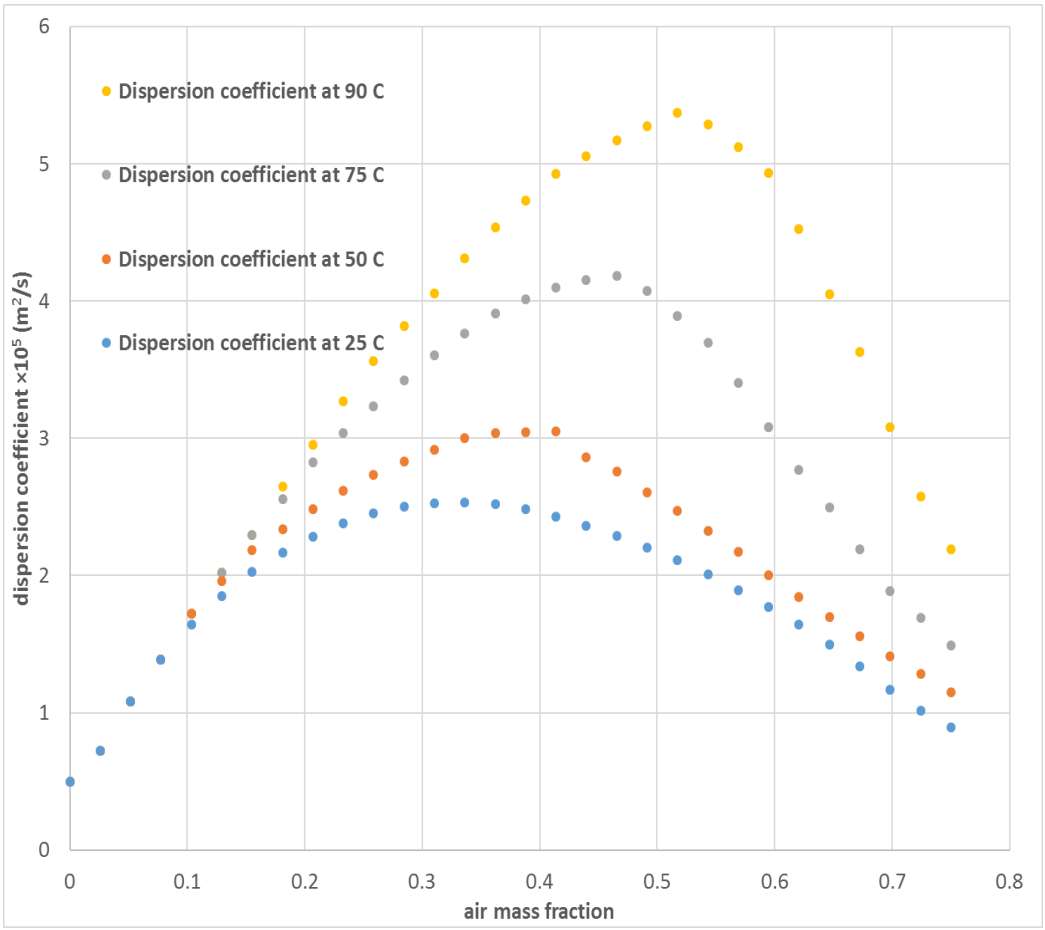

Figure 19: Dispersion coefficient function of air injection in heavy oil at different temperatures (25ºC, 50ºC, 75ºC, and 90ºC) (Pressure 0.514 MPa; Permeability 204 Darcy)

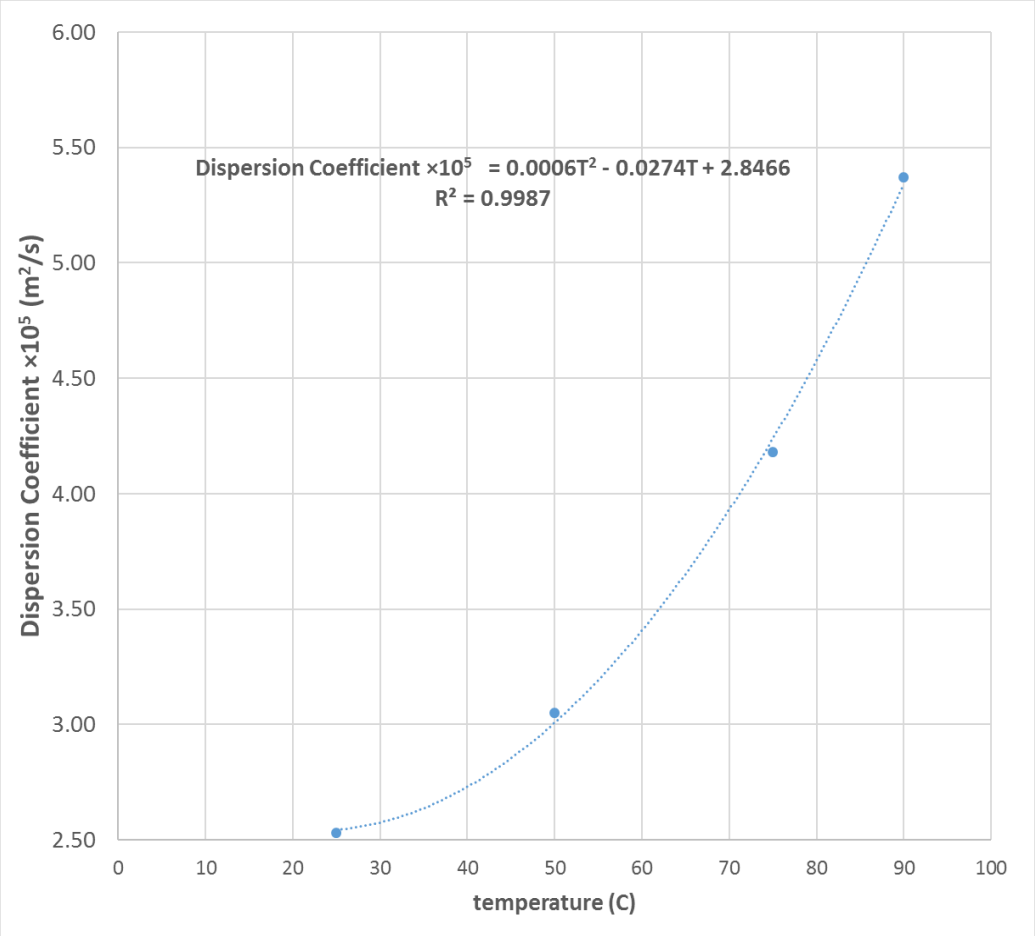

Figure 20: Maximum dispersion coefficient of air at different temperatures

5.2.3 Optimal Control Policy for Air Interfacial Temperature

The optimal control policy was obtained from the optimal control algorithm (See Section 4.6), where the interfacial temperature versus time, $[T_{int}(t)]$ is the control function of the process.

For a given set of operational conditions, the optimal air interfacial temperature policy is associated with the maximum heavy oil recovery calculated for the atmospheric air gas EOR. This policy is expected to yield enhanced experimental heavy oil recovery in agreement with a calculated

counterpart. This agreement is cross-checked in the experimental validation in the second step as laid out earlier in Section 5.2.1.

Figure 21 shows the air interfacial temperature versus time policy for different iteration based on an initial guess of the constant interfacial temperature of 90^{o}C at the pressure of 0.514 MPa and physical media permeability of 204 Darcy for 165 minutes of operational time. It can be seen that as iterative increases, the interfacial temperature after 1-hour periodically starts decreasing from 90^{o}C to 82^{o}C. It results in an iterative increasing of the objective functional companies to the maximum improvement in [$T_{int}(t)$]. The objective functional increases monotonically to the highest value of 175.55 (Figure 22). The change is significant at the beginning, but the rate of improvement slows down at final iteration. The final optimal function [$T_{int}(t)$] is obtained in 15 iterations. Table 10 lists the parameters used in the simulation of the mathematical model for the physical model of 204 Darcy permeability and the pressure of 0.514 MPa.

Lastly, the objective functional improvement over the constant temperature (90^{o}C) is about 20.66%. Finally, we can see that after 60 min the air production with oscillations in interfacial temperature is much better than the steady maximum interfacial temperature (Figure 21). As it was stated in preliminary results, this result may be ascribed to the corresponding periodic change in surface temperature of the physical model and the associated periodic reversal in the temperature gradient as well as the concentration gradient of air (through corresponding diffusivity and solubility changes[19,40]) within the physical model. This alteration of gradients boosts dispersion and leads to better mixing of air with the oil, thereby promoting its recovery.[42]

Table 10: Simulation model parameters of the mathematical model (Pressure 0.514 MPa, 204 Darcy permeability)

parameter	description	value
K_r	relative permeability	1
K	permeability	2.0130×10^{-6} (cm^2)
ρ	live oil density	0.78450 (g/cm^3)
g	gravity	3531600 (cm/min^2)
$\emptyset$	porosity	0.38
μ_o	live oil viscosity coefficient	1.3471 (g/cm.min)
k	thermal conductivity coefficient	0.055800 (J/cm.min.^{o}C)*
C_p	specific heat capacity	2.1300 (J/g.^{o}C)**
N_r	number of nodes in r direction	20
N_z	number of nodes in z direction	10
h_i	initial step size	10^{-5}
h_{max}	maximum step size	1
esp	accuracy of integration	10^{-6}
R	radius of physical model	3 (cm)
Z	height of physical model	25 (cm)
ITMAX	maximum number of iteration	200
STPMX	maximum step length for line search	10^{-2}

*, ** data provided from Saskatchewan Research Council, Alberta, Canada

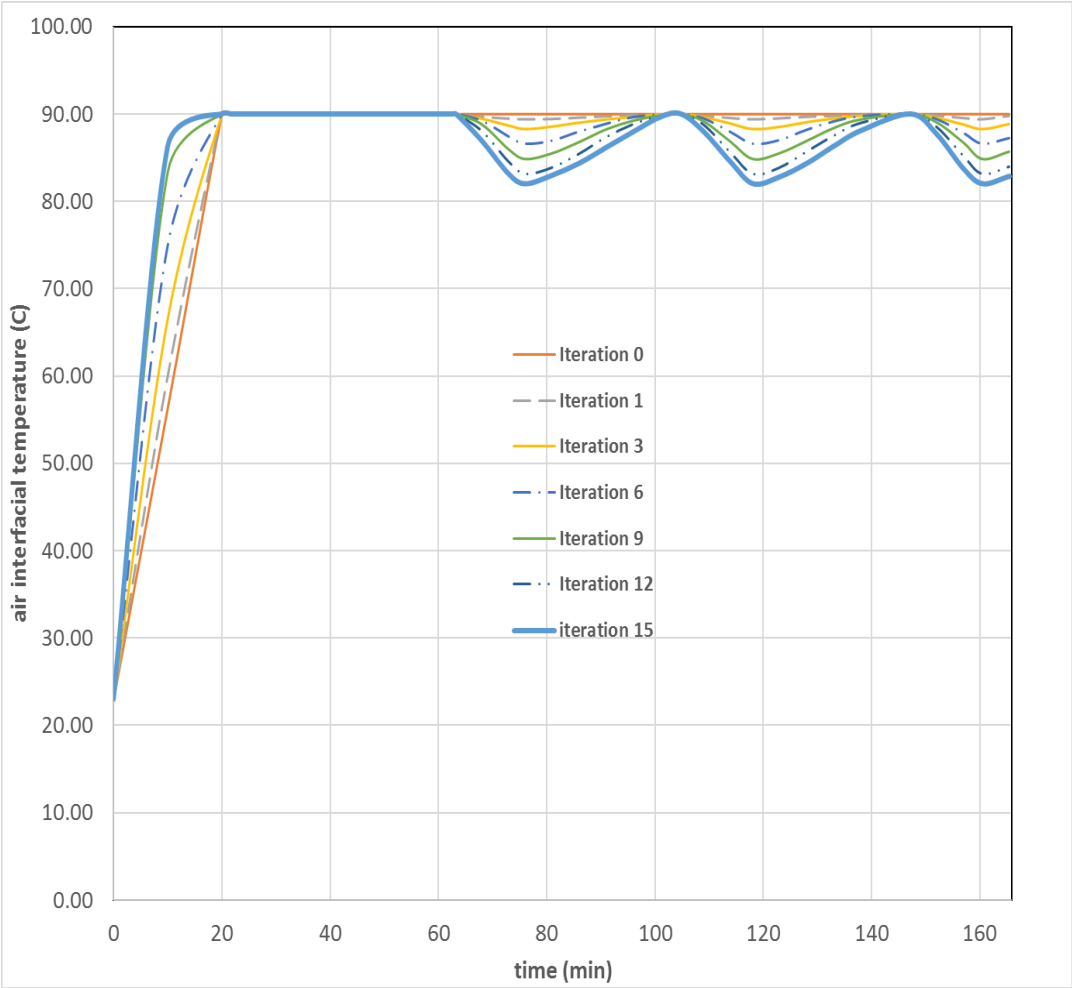

Figure 21: The interfacial air temperature $T_{int}(t)$ at different iterations on an initial guess of the constant interfacial temperature of 90°C

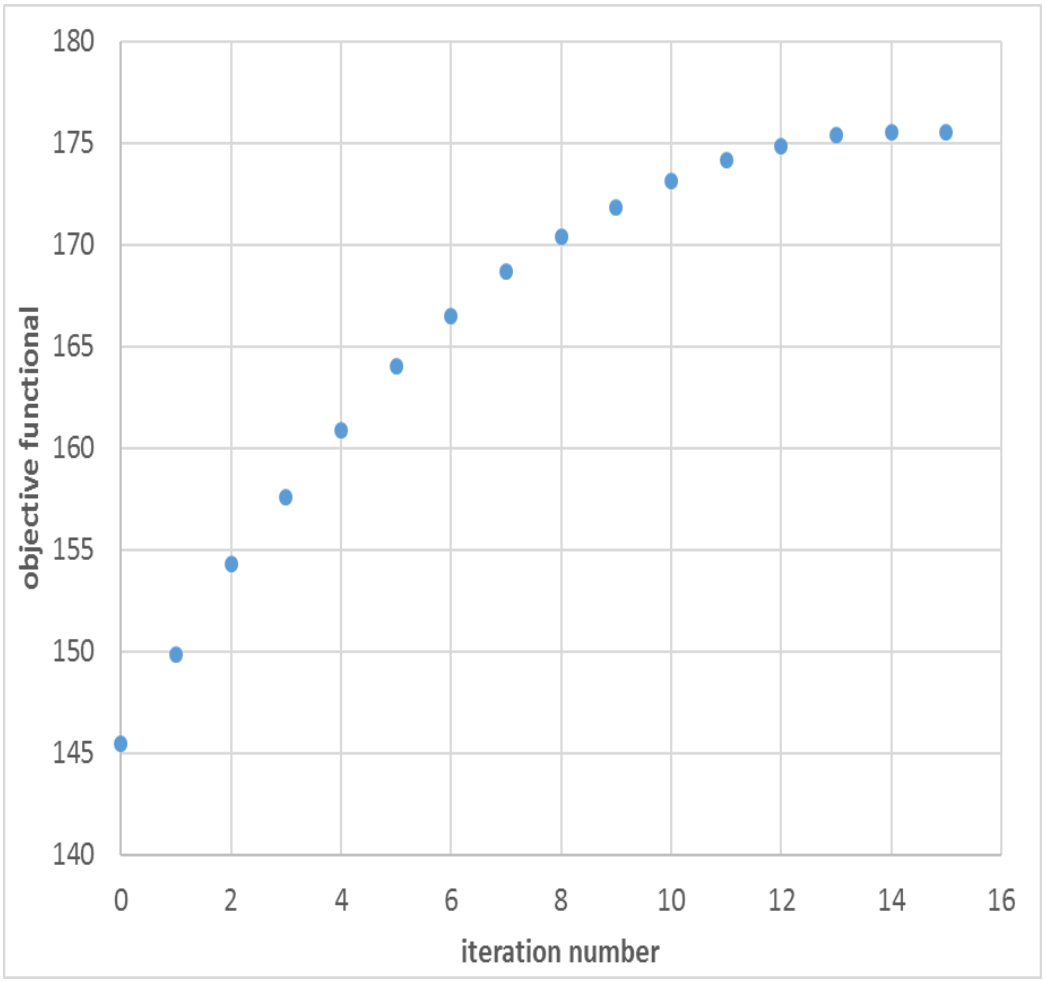

Figure 22: Objective functional versus iteration number for air injection (204 Darcy and Pressure 0.514 MPa)

For a better understanding the impact of initial T_{int} guess, we run the computation with a different initial guess to investigate its effect on the optimal objective functional. For a second trial, we have initiated a periodic temperature variation between 90°C to 75°C (Similar to Figure 13) as our initial guess of interfacial temperature [$T_{int}(t)$]. Figure 23 shows the air interfacial temperature versus time policy on an initial guess of periodic temperature variation. According to the figure, for the first hour, the [$T_{int}(t)$] iteratively increased to 90°C, while after one hour the [$T_{int}(t)$] iteratively periodically increased from 75°C to 82°C. This resulted in an iterative increasing of the objective functional to the maximum value of 175.55. Also, Figure 24 shows the objective function versus

the iteration number with the highest value of 175.55. The final optimal function [$T_{int}(t)$] was obtained in 12 iterations.

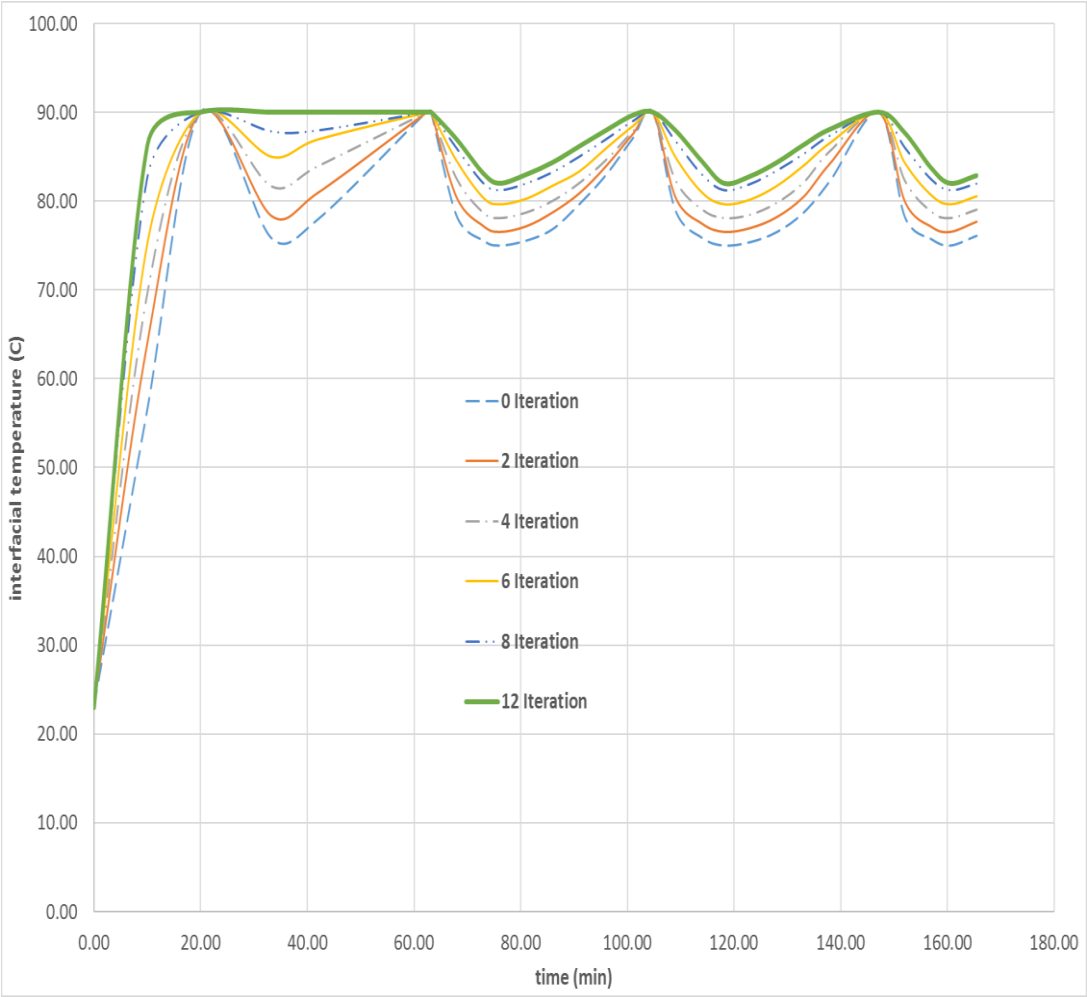

Figure 23: The interfacial solvent temperature $T_{int}(t)$ at different iterations on initial guess of periodic temperature variation between 90°C and 75°C after 20 min

It is interesting to note that the comparison of Figures 21 and 23 shows that there is no oscillation in the optimal interfacial temperature before 60 min. This indicates that the optimal oil production by that time was achieved at the maximum temperature of 90°C. To double-check this observation, we performed a computational run for 60 min only at an initial guess of periodic temperature variation between 90°C and 75°C. We observed the same pattern (Figure 23) that as iterative

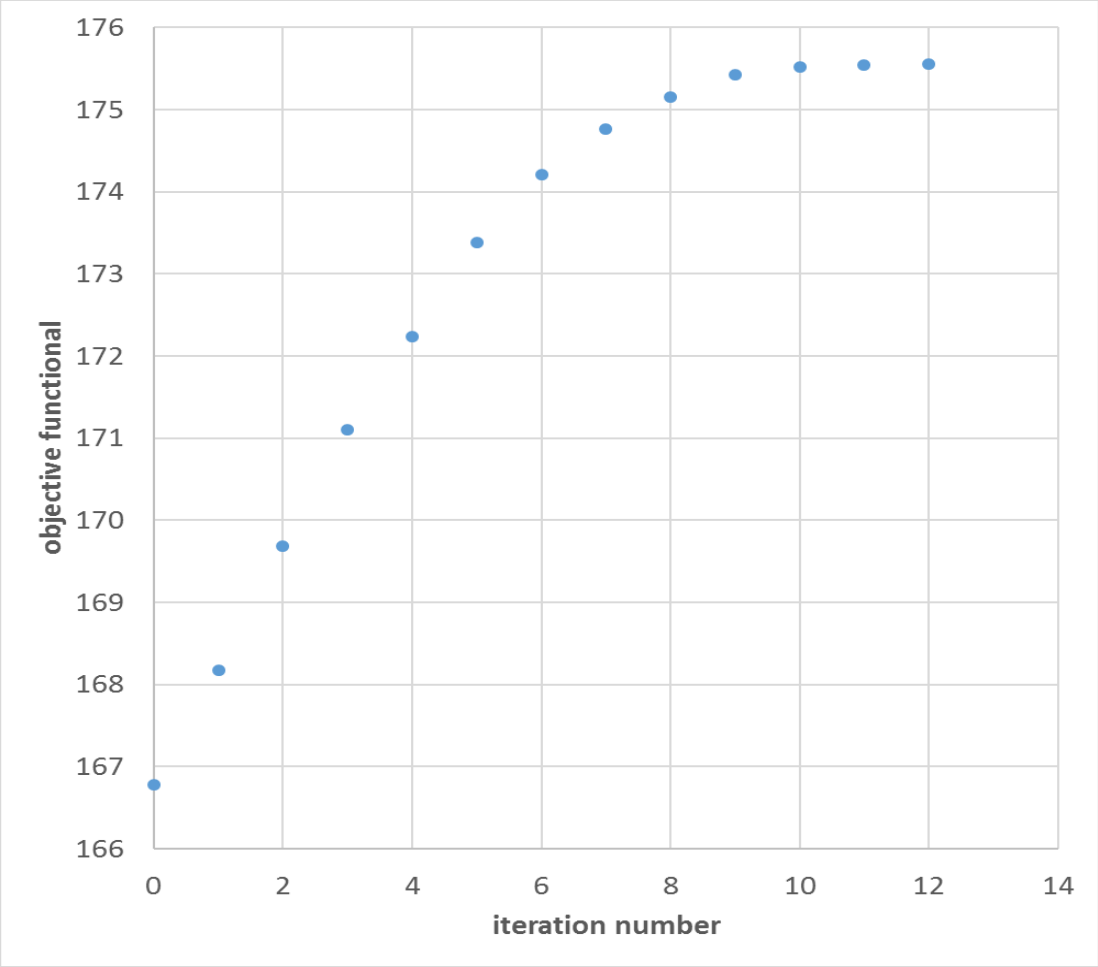

Figure 24: Objective functional versus iteration number for air injection (204 Darcy and Pressure 0.514 MPa)

increased, the interfacial temperature started to reach maximum 90^{o}C.

Table 11 shows the final objective functional at five different initial interfacial temperatures. As it can be seen, by choosing the constant temperature of 25^{o}C as an initial interfacial temperature guess, the maximum objective functional was 5.57 after 200 iterations.

Table 11: Comparison of maximum objective functional obtained from different initial interfacial temperature

initial interfacial temperature	iteration #	final optimal function [$T_{int}(t)$]	maximum objective functional
Periodic temperature variation between 90°C to 75°C (after 20 min)	12	- first hour: constant 90°C - afterward: periodic temperature variation of 90°C to 82°C	175.55
Constant temperature of 90°C (after 20 min)	15	- first hour: constant 90°C - afterward: periodic temperature variation of 90°C to 82°C	175.55
Constant temperature of 25°C	200	- constant T_{int} of 32°C	5.5700
Periodic temperature variation between 90°C to 50°C (after 20 min)	30	- first hour: constant 90°C - afterward: periodic temperature variation of 90°C to 82°C	175.55
20 minutes separation between each periodic variation of 90°C and 82°C (after 20 min)	13	- first hour: constant 90°C - afterward: 20 min pulse periodic temperature variation of 90°C to 75°C	160.77

Therefore, the optimal interfacial air temperature is to maintain T_{int} at 90°C (after 20 min) for 60 min, followed by periodic temperature variation between 90°C and 82°C with time (please see Figures 21 and 23). The maximum calculated objective functional is 175.55.

5.2.4 Validation of Optimal Control Policy

To validate the optimal injection temperature policy, the predicted objective functional corresponding to the optimal [$T_{int}(t)$] was compared to the experimental counterpart utilizing the same [$T_{int}(t)$]. In more detail, the simulated production rates were compared with the experimental ones obtained from another data set of an experiment conducted for the same physical model (set permeability) at the same operating conditions (optimal interfacial temperature [$T_{int}(t)$]).

Figure 25 shows that the experimental and calculated heavy oil recovery agree very well for the same optimal [$T_{int}(t)$]. The results indicate that the predicted heavy oil recovery was 175.55 g, and heavy oil recovered from the experimental work was 180.01 g. Thus, the average of relative errors at all sample times in the mass of heavy oil recovered was 1.82%. Furthermore, this figure shows the difference between the experimental optimal interfacial temperature and simulated interfacial temperature is very small with the average relative error less than 2%. Therefore, the

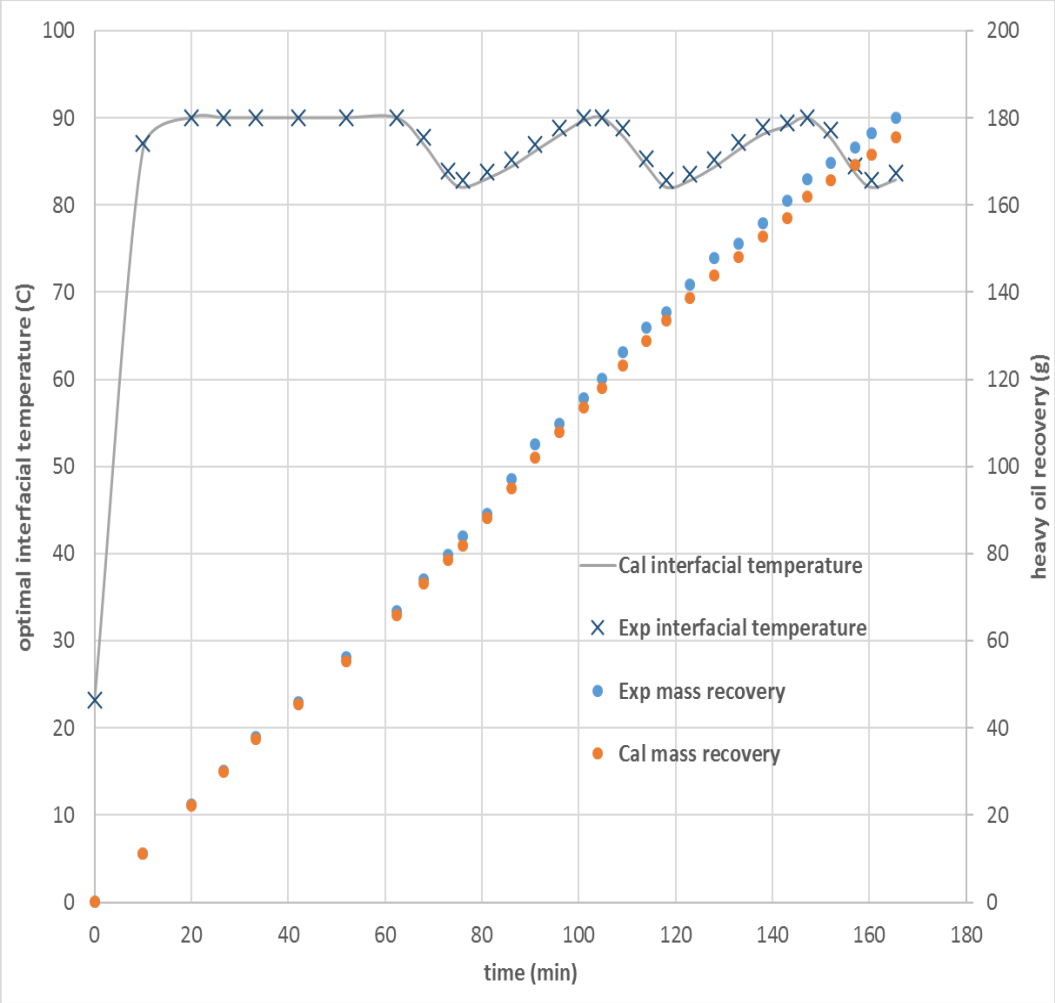

Figure 25: Experimental and calculated mass of live oil produced with time for air injection (Pressure 0.514 MPa, 204 Darcy)

small relative error demonstrates the confident of the optimal control strategy based on the developed process model.

5.2.5 Enhancement of Heavy Oil Recovery

The results in Table 11 shows that optimal [$T_{int}(t)$] policy was achieved at periodic interfacial temperature variation between 90^{o}C and 82^{o}C (see Figures 21 and 22). The optimal [$T_{int}(t)$] policy

enhances the heavy oil recovery by 20.660% in comparison to that at the constant temperature of 90^{o}C.

5.2.6 Permeability Effect on Optimal Policy

In this section, we examine the impact of physical model permeability (40, 87, and 427 Darcy) on optimal [$T_{int}(t)$] policy, as well as validation the model at different physical model permeability.

Figure 26 shows the air interfacial temperature versus time policy at the pressure of 0.514 MPa and physical media permeability of 427 Darcy for 165 minutes of operational time. According to the figure, permeability has minor or no impact on optimal [$T_{int}(t)$]. The objective functional improved upon increasing the permeability value to the maximum value of 260.19 (Figure 27).

The improvement of the objective functional at 427 Darcy (Figure 27) in comparison to computational run at 204 Darcy (Figure 22) may be attributed to the fact that the air can easier diffuse inside the physical model at a higher permeability.[26]

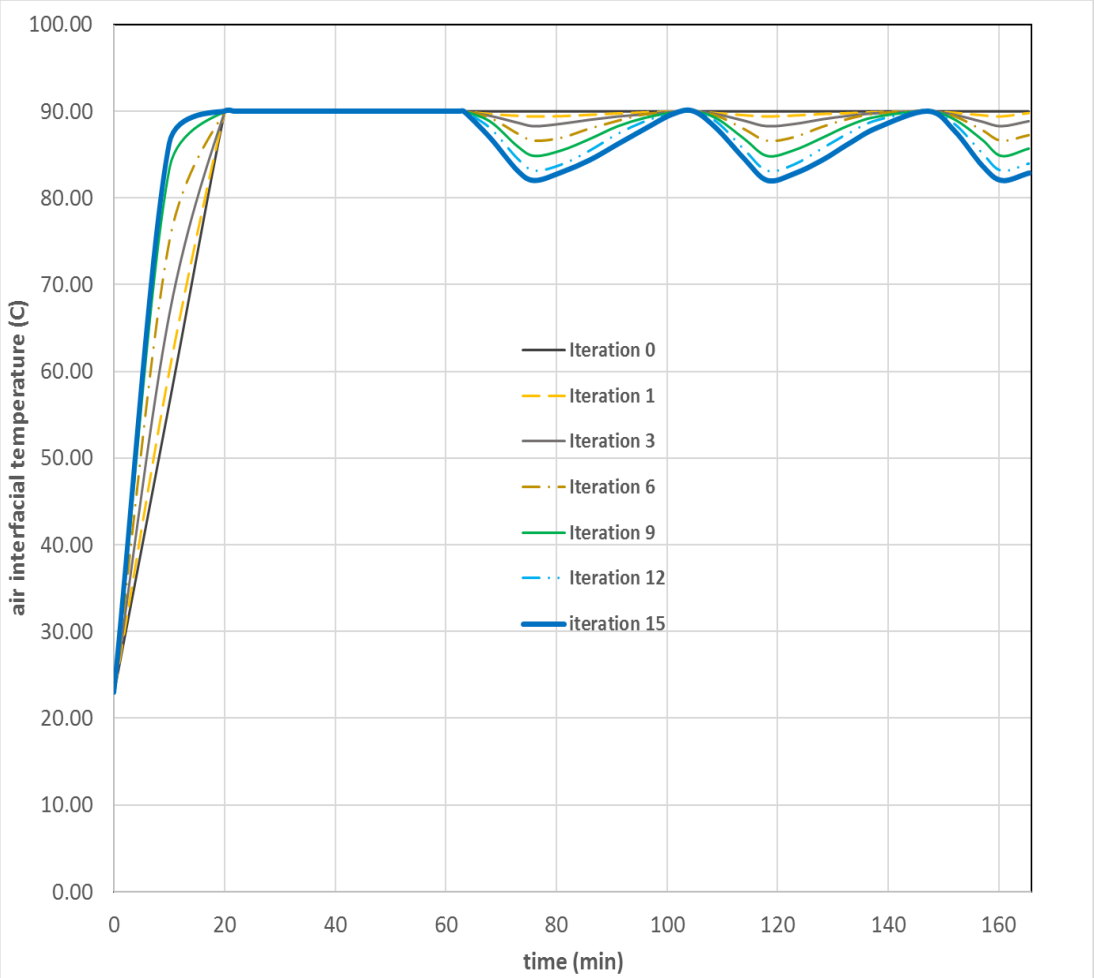

Figure 26: The interfacial air temperature $T_{int}(t)$ at physical model permeability of 427 Darcy and air pressure of 0.514 MPa

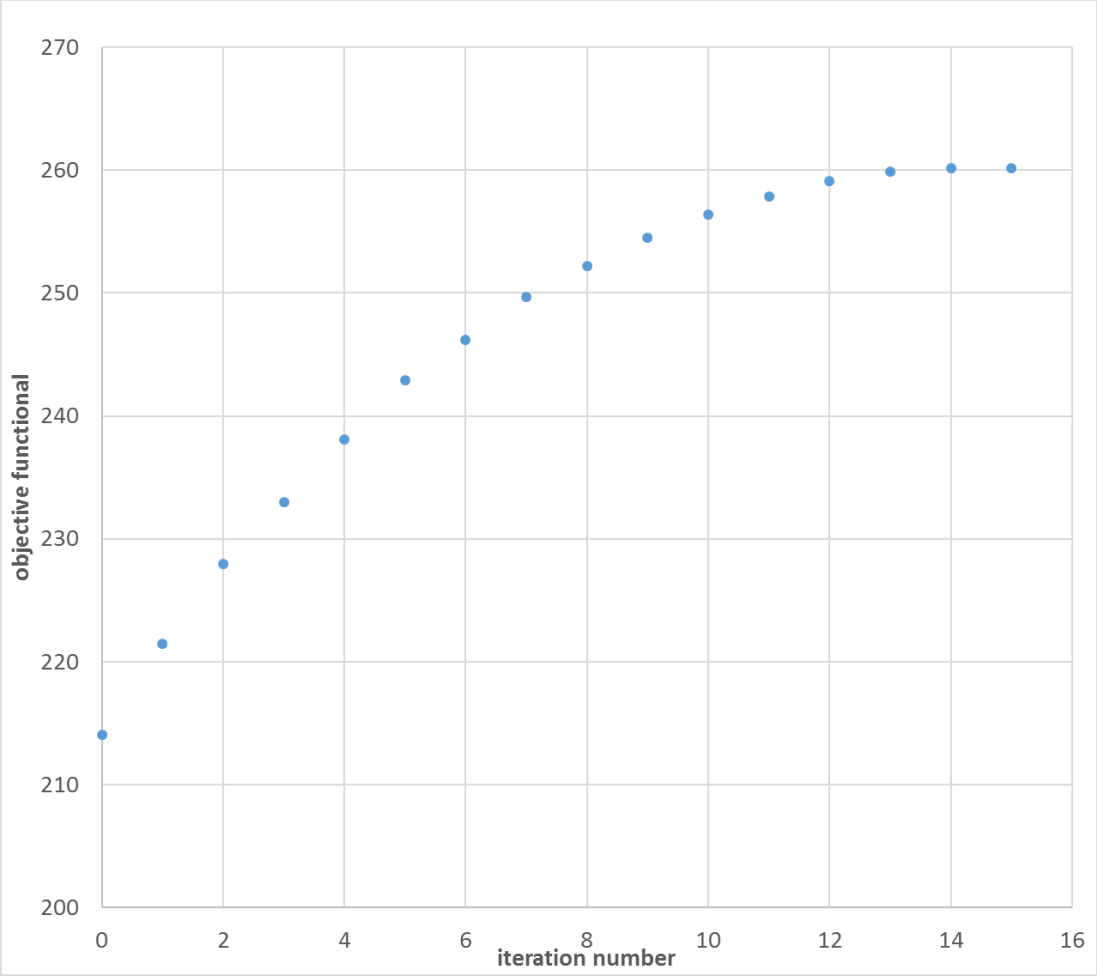

Figure 27: Objective functional versus iteration number for air injection (427 Darcy and Pressure 0.514 MPa)

Figures 28 and 29 show the objective functional versus iteration number at 40 Darcy and 87 Darcy, respectively. Similar to Figure 24, the change was significant at the beginning, but the rate of improvement slowed down at final iteration.

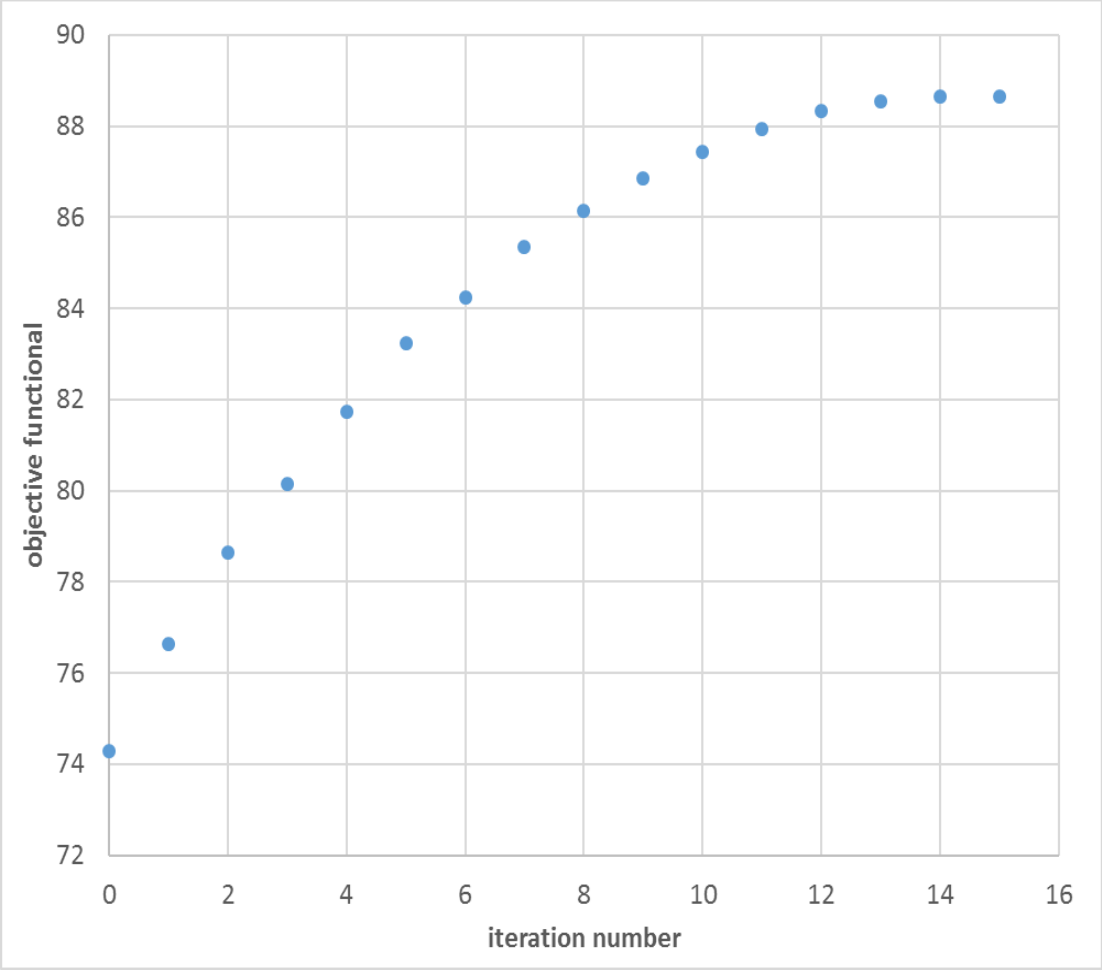

Figure 28: Objective functional versus iteration number for air injection (87 Darcy and Pressure 0.514 MPa)

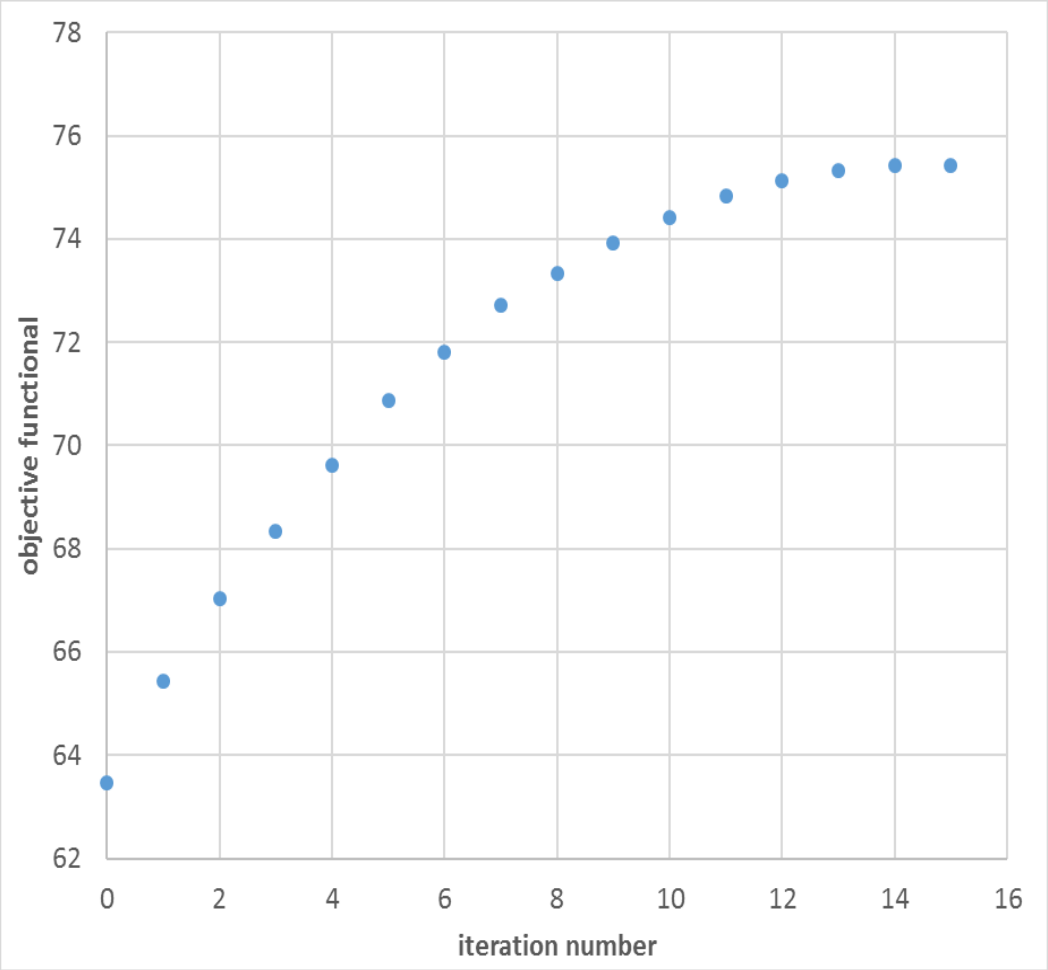

Figure 29: Objective functional versus iteration number for air injection (40 Darcy and Pressure 0.514 MPa)

Lastly, it is required to validate the optimal control policy with experimental results for the computational runs above. Figure 30 shows the comparison between the calculated objective functional versus the experimental value at three different packs of permeability of 40, 87, and 427 Darcy. The average of relative errors for 40, 87, and 427 Darcy at all sample times in the mass of heavy oil recovered were found to be 2.1%, 2.8%, and 3.6%, respectively. Therefore, the low relative errors demonstrate that the optimal control developed in this study can be confidently applied to enhance oil recovery at different permeability as well.

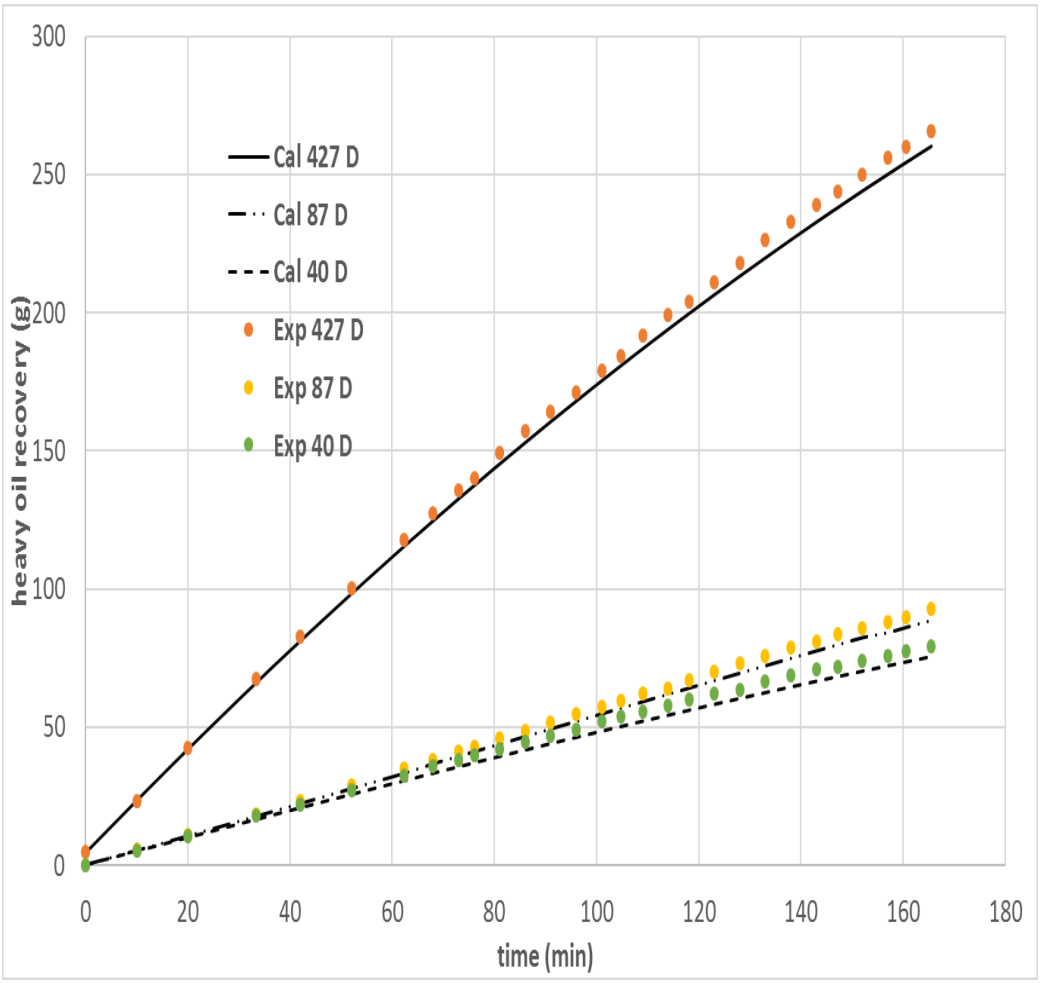

Figure 30: Experimental and calculated heavy oil recovery at three different medium permeability

5.2.7 Sensitivity Analyses of the Model Parameters

A sensitivity analysis of the model parameters on the calculated objective functional value was undertaken by varying live oil density (ρ), live oil viscosity coefficient (μ), specific heat capacity (C_p), thermal conductivity coefficient (k), grids number, dispersion coefficient [$D(\omega,T)$], and interfacial mass fraction [$\omega_{int}(t)$].

The results of the sensitivity analyses were compared with the based final iteration objective functional value for 204 Darcy permeability, and 0.514 MPa (absolute) injection pressure. The

sensitivity analyses were also experimentally validated. Table 12 shows the percentage change in the objective functional value.

- For a $\pm$ 5% variation in live oil density (ρ), the change in the maximum objective functional is about 0.54% of the based value.
- For a $\pm$ 5% variation in viscosity coefficient (μ), the change in the maximum objective functional is about 1.16% of the based value.
- For a $\pm$ 5% variation in specific heat capacity (C_p), the change in the maximum objective functional is about 0.55% of the based value
- For a $\pm$ 5% variation in thermal conductivity coefficient (k), the change in the maximum objective functional is about 0.48% of the based value
- The change in the maximum objective functional is about 1.3% of the based value when changing the number of grids in the radial direction. However, the change in maximum objective functional is about 0.7% of the based value when changing the number of grids in the vertical direction. The set modeling value for N_z and N_r are 20 and 10, respectively (Table 12).
- For a $\pm$ 5% variation in the dispersion coefficient [$D(\omega,T)$], the change in the maximum objective functional is about 2.2% of the base value.
- For a $\pm$ 5% variation in the air interfacial concentration [$\omega_{int}(t)$] value, the change in the maximum objective functional is about 7.01% of the based value.

Thus, the objective functional is less sensitive to variation in live oil density, specific heat capacity, thermal conductivity coefficient, and grid numbers in comparison to viscosity coefficient (μ_o),

dispersion coefficient [$D(\omega,T)$], and interfacial solvent concentration [$\omega_{int}(t)$]. Also, the initial [$T_{int}(t)$] guess is very important to determine the maximum objective functional (Table 11).

Lastly, we examined the sensitivity of initial dispersion [$D(\omega,T)$] compared to optimal dispersion coefficient for 204 Darcy permeability, and 0.514 MPa (absolute) injection pressure. For a ±5% variation in the initial dispersion coefficient, the change in dispersion value is about 0.2% of the base value.

Table 12: Change in maximum objective functional by variation in parameters

parameter	**variation in parameter**	**% change in maximum** I
live oil density	+ 5%	-0.54
	- 5%	0.54
viscosity coefficient	+ 5%	1.16
	- 5%	-1.16
specific heat capacity	+ 5%	-0.55
	- 5%	0.55
thermal conductivity	+ 5%	-0.48
coefficient	- 5%	0.48
grid numbers	$N_r = 25$, $N_z = 10$	-1.29
	$N_r = 15$, $N_z = 10$	1.29
	$N_r = 20$, $N_z = 12$	-0.70
	$N_r = 20$, $N_z = 7$	0.70
dispersion coefficient	+ 5%	-2.20
	- 5%	2.20
interfacial concentration	+ 5%	-7.01
	- 5%	7.01

5.2.8 Potential for Field Scale

In field scale heavy oil reservoirs that are more than a few kilometers thick, the temperature and pressure would exceed the limits of this study. There is a possibility of minor oxidation reactions upon air injection into such reservoirs for more than a year.[58,59]

Given this caveat, the results of this experimental study are pertinent to heavy oil recovery from shallow reservoirs at low temperature and pressure conditions that are conducive to non-reactive environments. For those circumstances, this study demonstrates a concept that air injection with periodic temperature variation has the potential to enable significant oil recovery.

Table 13 shows heavy oil recoveries reported in previous investigations, which used different gas solvents with physical models similar to the ones in this study. It is observed that the recovery of 69.1% OOIP obtained with air in this study is, on an average, about 16% lower compared to that with propane or butane.[49,50,61]

This is very encouraging given the fact that air is freely available while hydrocarbon solvents are costly and their use for oil recovery is therefore almost impractical at present.[22,57]

Table 13: Oil recoveries obtained in previous studies with different solvents

reservoir model	solvent	heavy oil	*T*(ºC)	*P*(MPa)	% OOIP	ref. no.
cylindrical sand packed model with glass beads. Physical model permeability: 44.4, 97.4, 220, and 439.2 Darcy	butane	Fort Kent (14,500 mPa·s)	21	0.09-0.112	80	49
cylindrical sand packed model with glass beads. Physical model permeability: 44.4, 97.4, 220, and 439.2 Darcy	propane	Fort Kent (14,500 mPa·s)	21	0.413-0.68	92	50
cylindrical sand packed model with glass beads. Physical model permeability: 51, 102, and 204 Darcy	propane	Athabasca (225,000 MPa.s)	21	0.790	89	48
cylindrical sand packed model with glass beads. Physical model permeability: 110 Darcy	butane	Fort Kent (14,500 mPa·s)	23	0.11	85	57

Chapter 6: Conclusions

In this work, air injection was considered for the first time to recover heavy oil at low temperature and pressure conditions under a non-reactive environment in a solvent-assisted gravity drainage process. The effect of constant as well as periodic air temperatures was examined in lab-scale experiments. The air was injected at 0.169, 0.286, 0.403 and 0.514 MPa absolute and temperatures in the range 25^{o}C-90^{o}C into lab-scale physical models of 40, 87, 204, and 427 Darcy permeability and 38% porosity. The maximum heavy oil recovery of 58.2% of the OOIP was achieved using air at the constant temperature of 90^{o}C and 0.514 MPa pressure with 427 Darcy permeability of the physical model. The periodic variation of the air temperature between 75^{o}C and 90^{o}C boosted that recovery to 69.1% of the OOIP, which is an improvement by 18.6%. Overall, the results showed that the utilization of freely available air at low pressures and periodically varying low temperatures was promising for oil recovery from shallow reservoirs under non-reactive conditions.

In the next step, a rigorous mathematical model of the lab-scale recovery process was developed with interfacial air temperature versus time as a control function. The conditions necessary for optimal control were derived and utilized in a computational algorithm to determine the optimal control.

Following are the salient contributions stemming from the mathematical and computational part of this work:

1. The optimal interfacial temperature versus time (control policy) was determined between 90^{o}C and 82^{o}C, which registered 20.66% increase in the oil recovery in comparison to the constant temperature of 90^{o}C.
2. The control policy was successfully validated using experiments. The heavy oil recovery with the optimal [$T_{int}(t)$] was found to be within 1.82% of that predicted by the optimal control algorithm.
3. The computation time reduced from 2 weeks to 5 days by scaling the dependent variables of the differential equations.

The recommendations for future work are as follows:

1. Optimal control algorithm used in this study is open loop. Investigate the performance of a close-loop optimal control for the system.
2. Improve the heavy oil experimental setup to enable quicker heating and cooling of the system, and explore better temperature policies.
3. Carry out similar investigations using different gases (i.e., carbon dioxide, propane, and butane) to gain deeper understanding of the effect of solvent temperature oscillations on oil production.

Appendix A: Porous Medium Permeability Calculation

Sample calculation of porous media of 40 Darcy:

The permeability (K) was calculated by applying the following equation (Dullien, 1992)

$$K = \frac{Q\mu\Delta x}{A\Delta P} \times 1.01325 \times 10^{12}$$

where Q is the volumetric fluid flow rate through the media, A is the cross-section area of fluid flow through the medium, μ is the dynamic viscosity of the fluid, and ΔP is the pressure difference across the medium of thickness Δx. The values of these parameters are listed in Table 4 for glass beads of size in the range 0.248-0.210 mm.

$$K = \frac{(1.66001 \times 10^{-5})(1.8401 \times 10^{-5})(0.21)}{(2.82 \times 10^{-3})(577)} \times 1.01325 \times 10^{12}$$

$$K = 40 \text{ Darcy}$$

Appendix B: Solubility and Live Oil Density

Sample calculation of air solubility (or dissolved mass fraction) and live oil density.

To calculate the atmospheric air solubility and live oil density, substitute in Equations (13) and (14) for all the parameters from Table 14:

$$\text{Air dissolved mass fraction} = \frac{0.15302}{9.6421+0.15302} = 0.015620 \quad (13)$$

$$\text{Live oil density} = \frac{9.6421+0.15302}{11.731} = 0.83481 \quad (14)$$

Table 14: Calculated air solubility and live oil density at 25°C and 204 Darcy

pressure (MPa absolute)	**dead oil mass** (g)	**live oil volume (cm^3)**	**collected air mass** (g)	**live oil density (g/cm^3)**	**dissolved air mass fraction**
0.169	4.6710	5.8105	0.035010	0.80941	0.0074370
0.286	6.2632	7.7601	0.064030	0.81482	0.010115
0.403	8.0610	9.9411	0.10601	0.82144	0.012979
0.514	9.6402	11.731	0.15302	0.83481	0.015620

Also, Table 15 shows the air solubility, live oil density, and viscosity at different temperatures.

Table 15: The result of live oil viscosity, live oil density, and air solubility at different temperatures

temperature (°C)	**viscosity** (mPa.s)	**live oil density (g/cm^3)**	**dissolved air mass fraction**
25	11,500	0.83481	0.015601
50	642.00	0.81510	0.061102
75	86.800	0.79582	0.16603
90	11.200	0.78452	0.46301

Lastly, Figure 31 shows the correlation between air temperature and viscosity in this study.

$$\mu = 2 \times 10^{11}(T)^{-5.118} \tag{136}$$

with the r^2 value of 0.9671.

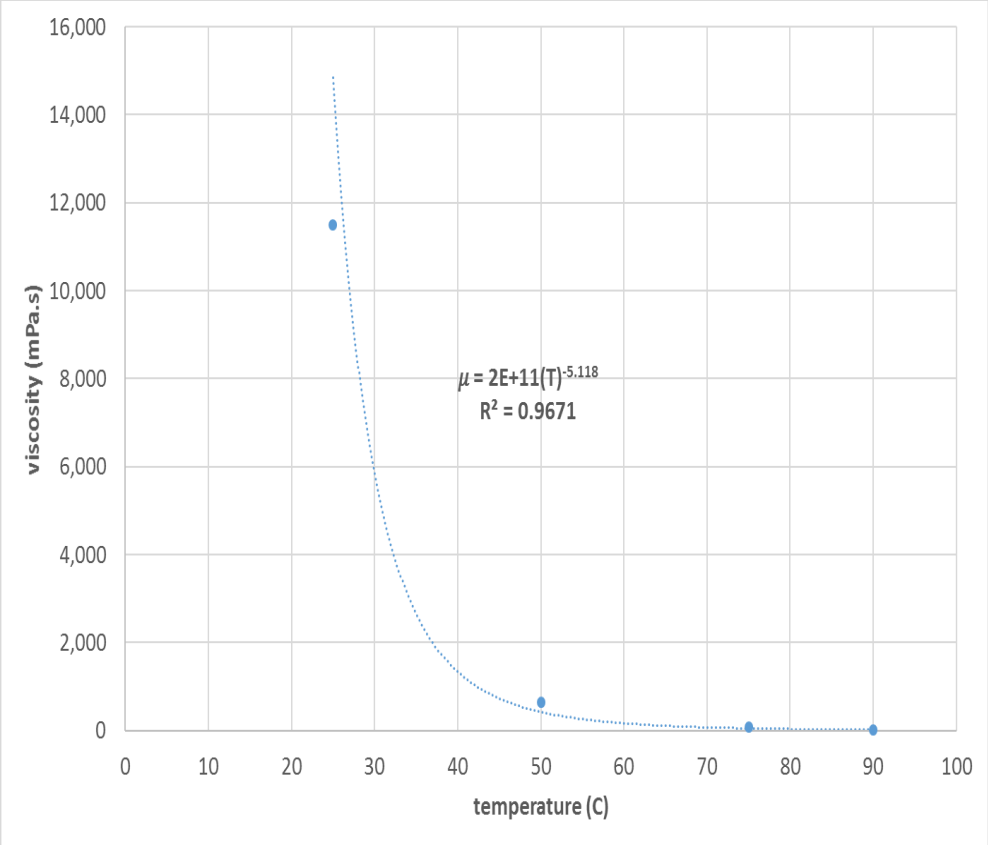

Figure 31: Variation of viscosity with air temperature at 0.514 MPa absolute and 204 Darcy permeability of the physical model

Appendix C: Preliminary Experimental Results for Nitrogen Injection

This appendix presents the impacts of permeability, pressure, and temperature on heavy oil recovery using nitrogen gas. In all the preliminary experiments, the experimental conditions are exactly same as atmospheric air injection, except in this part we have used pure nitrogen as a solvent (purity 99.9%)

Impact of Permeability

According to Figure 32, the heavy oil recovery increased marginally higher than atmospheric air injection (0.71 to 2.36% of the OOIP) (Figure 7). This may be because unlike injection pure nitrogen gas, the atmospheric air injected has about 78% nitrogen gas.

Lastly, Figure 33 shows the correlation between the production rate and permeability. In both cases (air and nitrogen), the correlation has the same pattern.

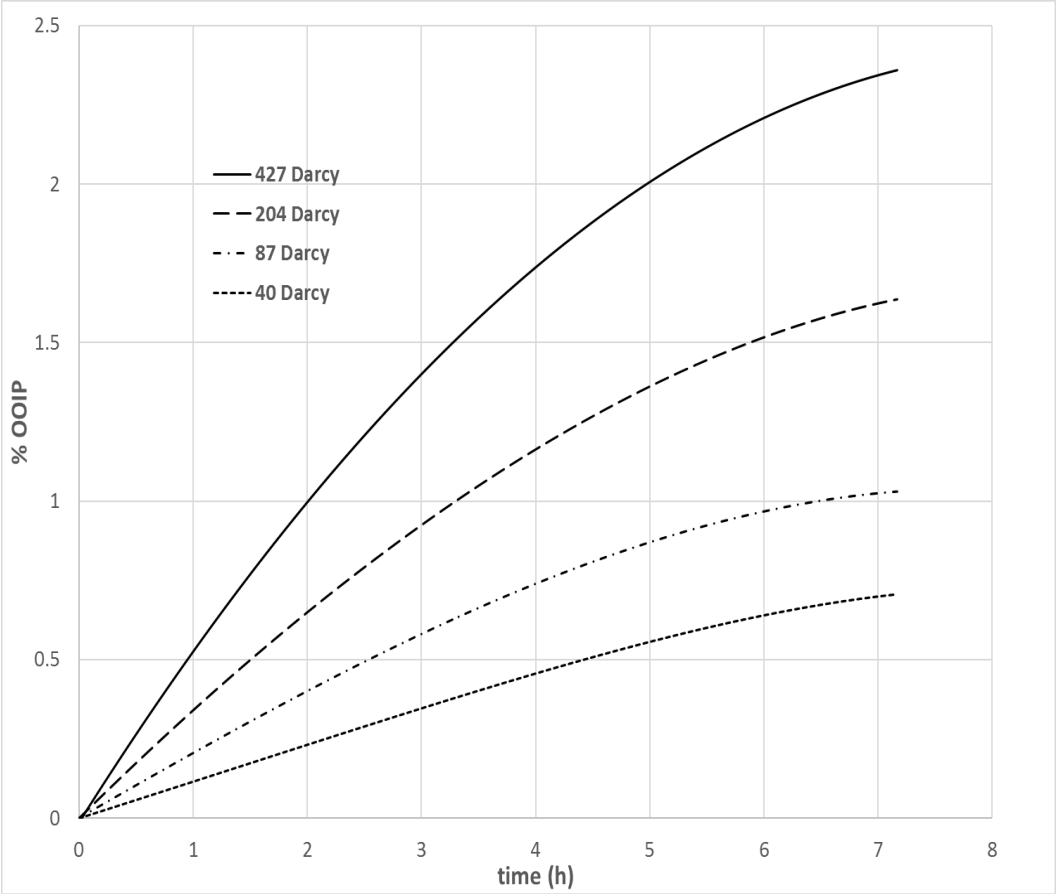

Figure 32: Oil recovery versus time for different permeabilities at 0.514 MPa absolute and 25ºC. (Solvent: Nitrogen)

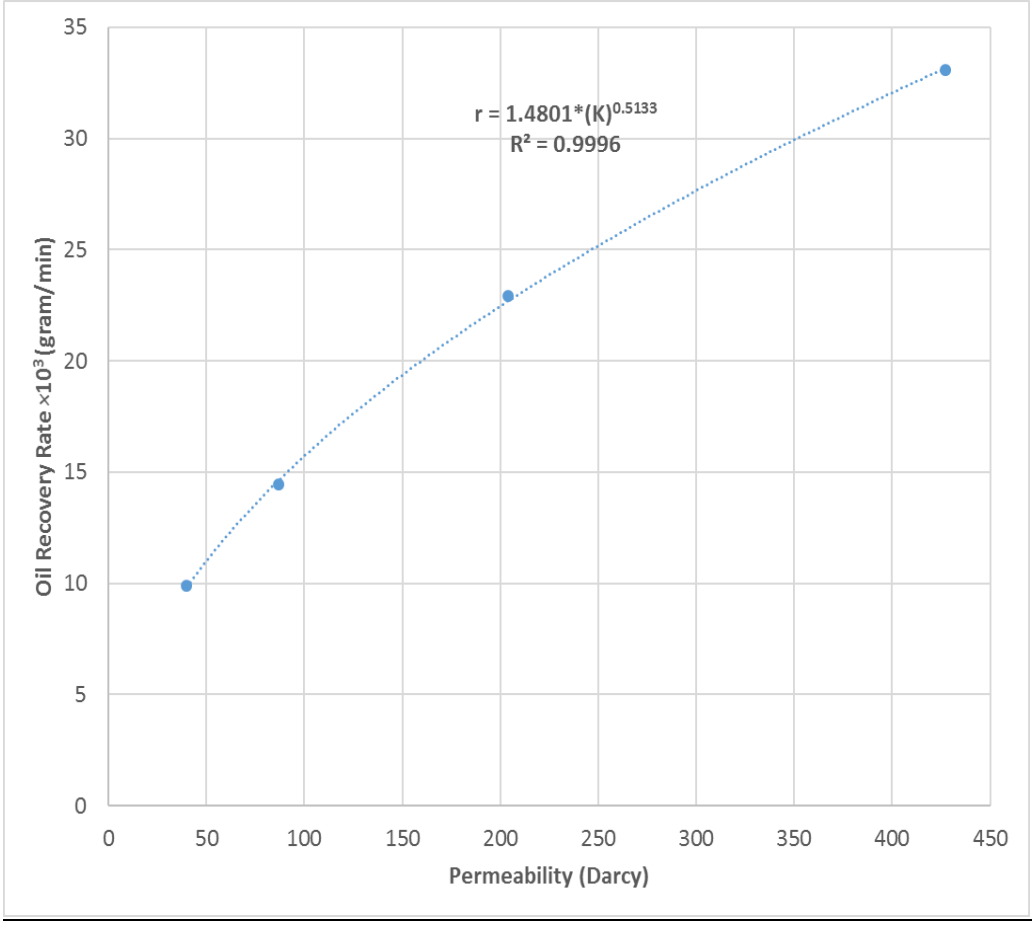

Figure 33: Variation of production rate with model permeability at pressure of 0.514 MPa absolute and temperature of 25°C (Solvent: Nitrogen)

Impact of Pressure

As it can be seen in Figure 34, as the injection nitrogen pressure increased, the recovery factor using nitrogen gas increased from 0.78% to 1.65% of the OOIP.

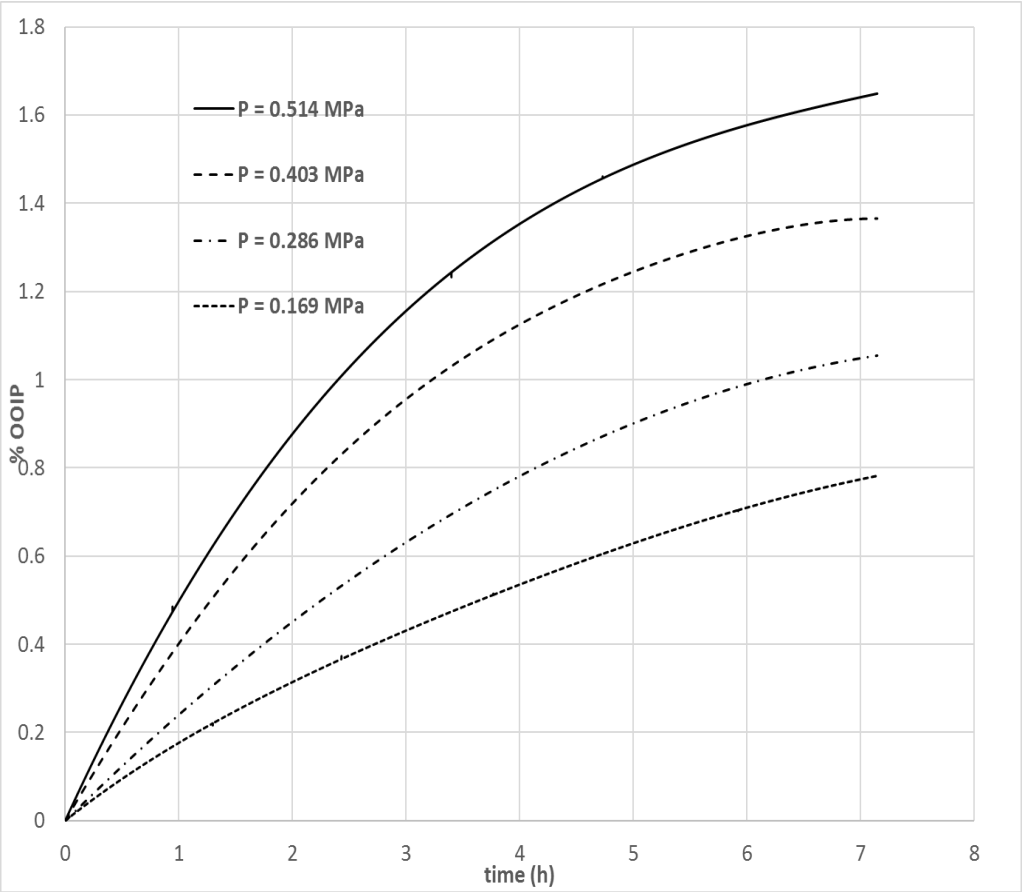

Figure 34: Oil recovery versus time at 25^{o}C nitrogen temperature, 204 Darcy model permeability, and different air pressures (absolute)

Impact of Constant Temperature and Periodic Temperature Variation

Similar to atmospheric air injection, the diffusivity of nitrogen in heavy oil was found to increase with temperature (Figure 35). The results show that by increasing temperature from 25°C to 90°C, oil recovery rose from 1.63% to 42.41% of the OOIP.

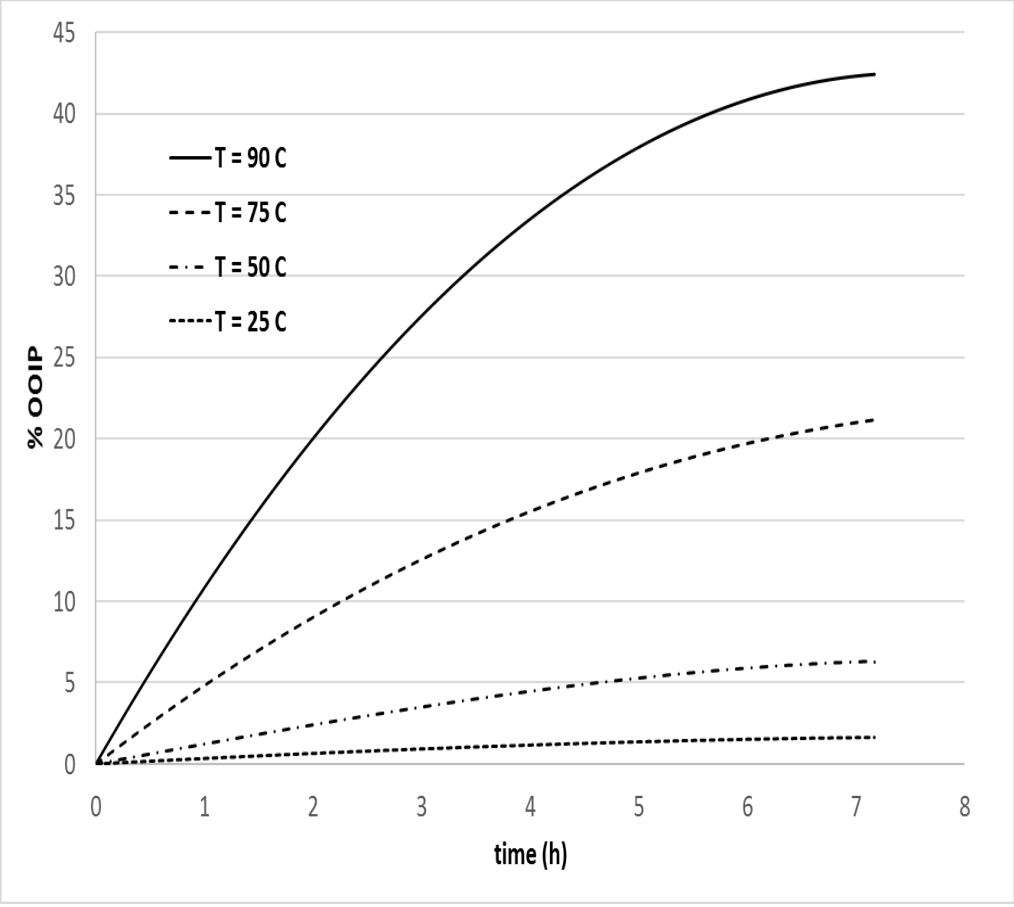

Figure 35: Oil recovery versus time at 0.514 MPa absolute nitrogen pressure, 204 Darcy model permeability, and different nitrogen temperatures

We have also compared the effect of periodic temperature variation using nitrogen for heavy oil recovery under same experimental conditions (see Section 5.1.3). Figure 36 shows the impact of periodic temperature variation between 90°C and 75°C at 0.414 MPa and the physical model of

204 Darcy. As it was expected, we observed an enhancement of oil recovery increased from 42.41% to 49.86% of the OOIP using period temperature variation in comparison to the constant temperature (90^{o}C).

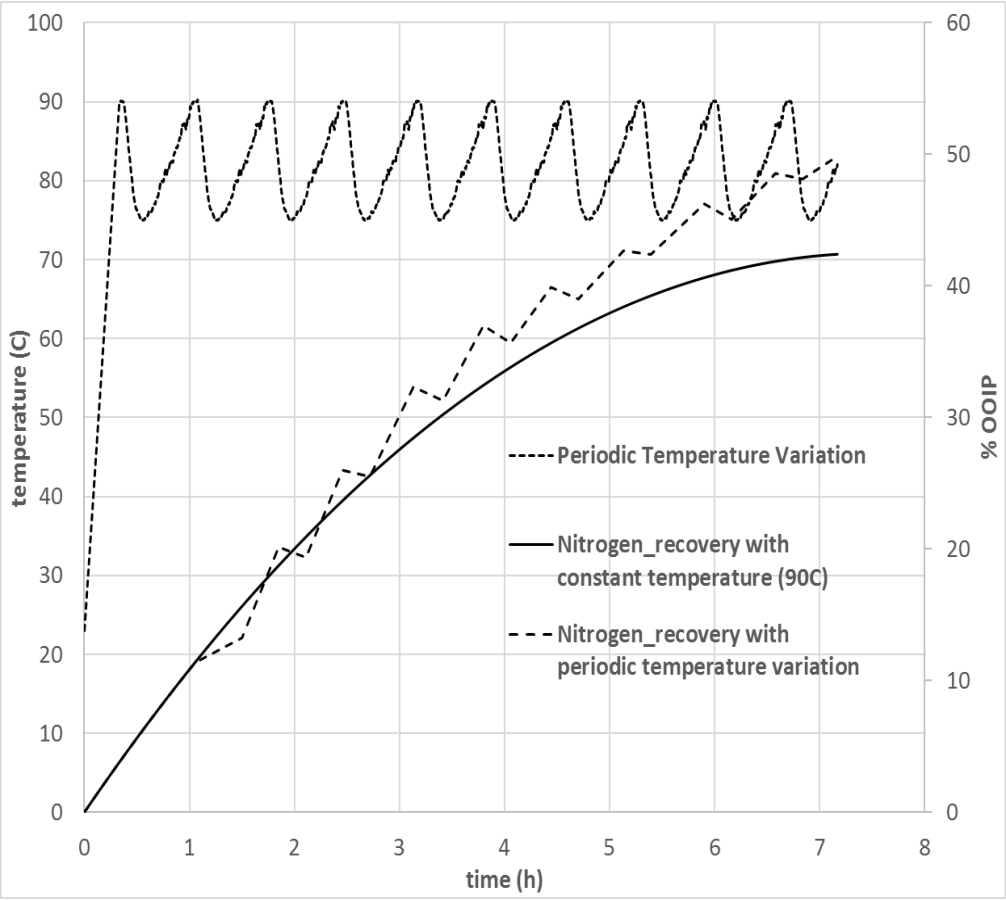

Figure 36: Oil recovery versus time at 0.514 MPa absolute Nitrogen pressure, 204 Darcy model permeability, and constant (90^{o}C) as well as periodically varying nitrogen temperature in the range, 75-90^{o}C

Effect of Varying Temperature with Different Permeabilities for Nitrogen Injection

Similar results were observed using nitrogen injection under period temperature variation between 90ºC and 75ºC, and different physical model permeability with the highest increase in %OOIP was achieved as 427 Darcy with the value of %71.20 (Figures 37-39).

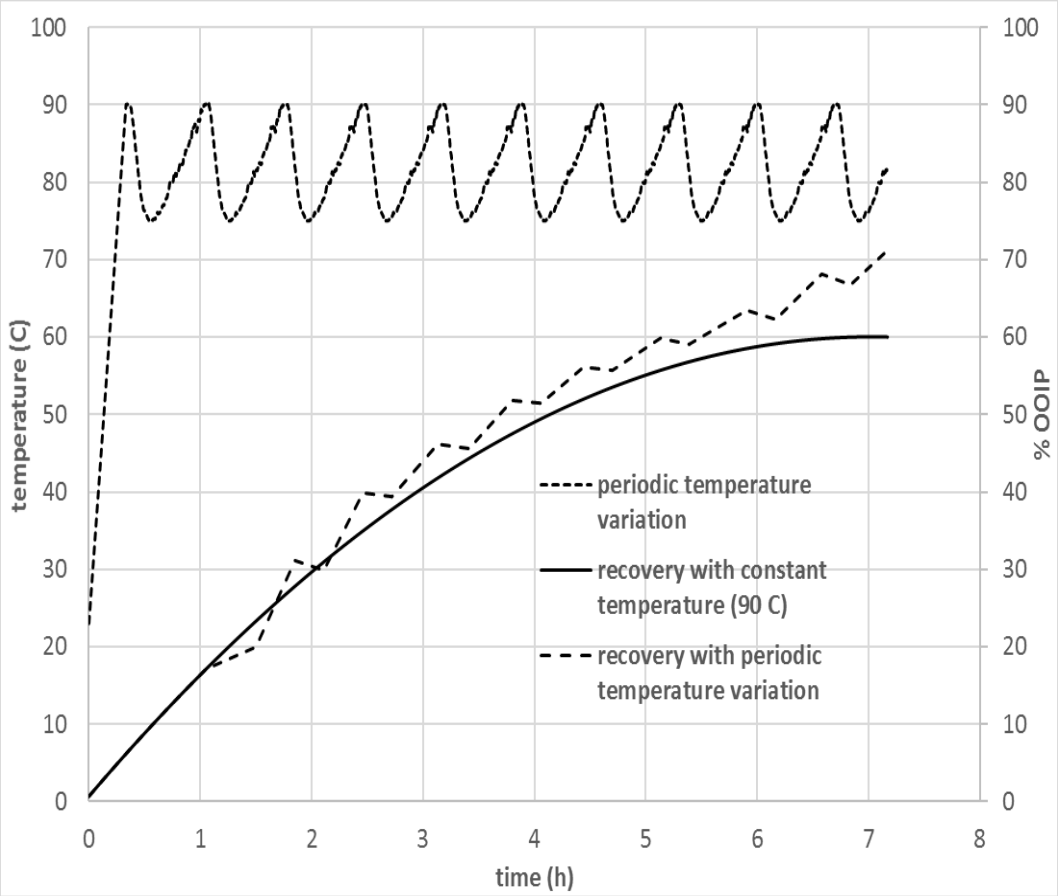

Figure 37: Oil recovery versus time at 0.514 MPa absolute nitrogen pressure, constant (90ºC) as well as periodically varying air temperature in the range, 75-90ºC, and 427 Darcy model permeability

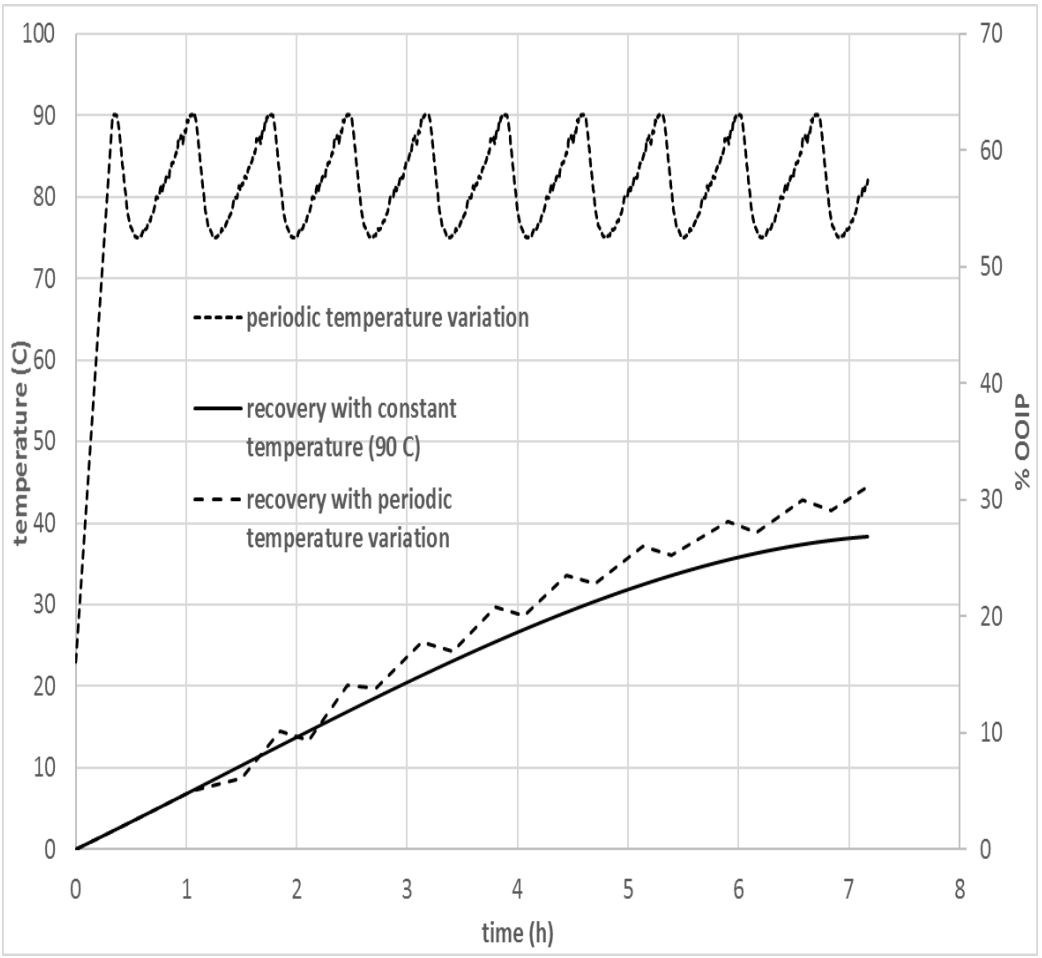

Figure 38: Oil recovery versus time at 0.514 MPa absolute nitrogen pressure, constant (90ºC) as well as periodically varying air temperature in the range, 75-90ºC, and 87 Darcy model permeability

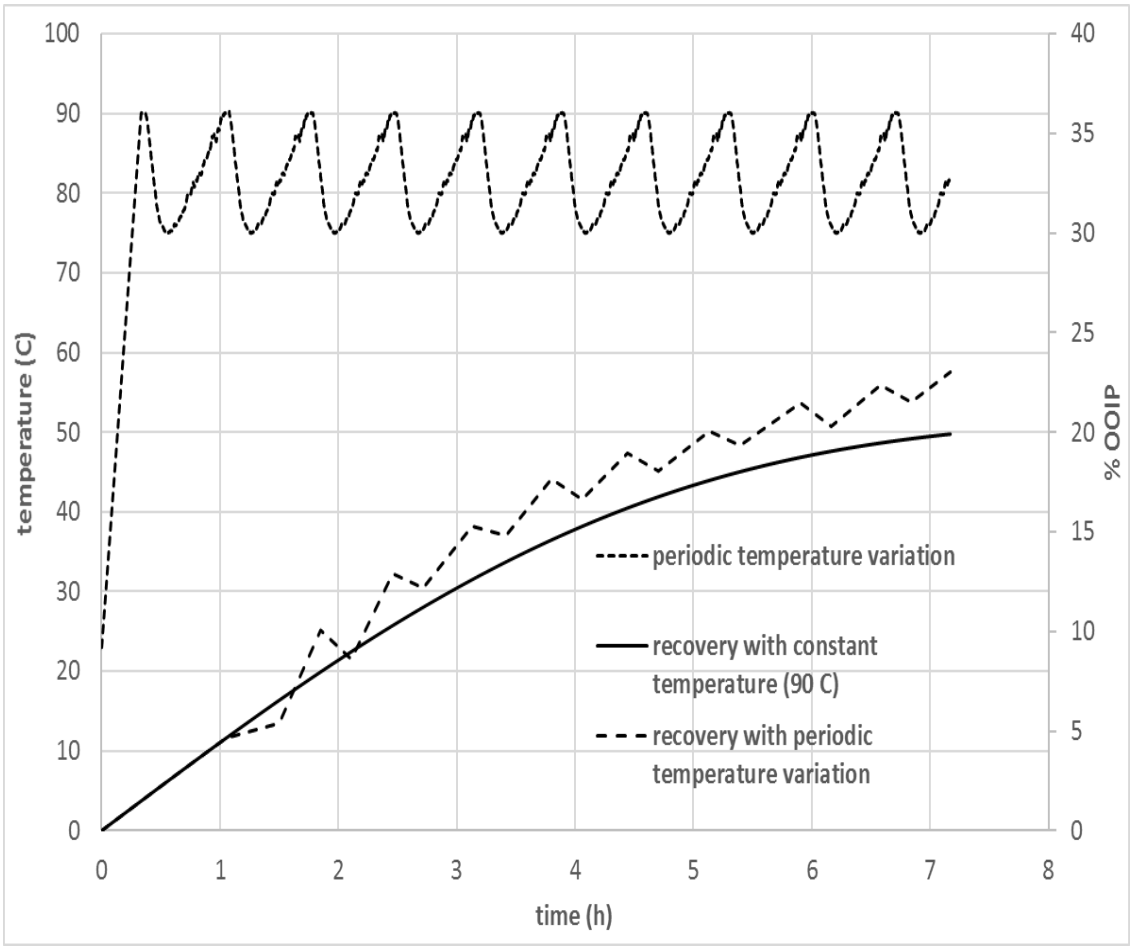

Figure 39: Oil recovery versus time at 0.514 MPa absolute nitrogen pressure, constant (90^{o}C) as well as periodically varying air temperature in the range, 75-90^{o}C, and 40 Darcy model permeability

In summary, the above experimental results indicate that periodic temperature variation effectively enhanced oil recovery in comparison to the constant temperature of 90^{o}C for both nitrogen and atmospheric air injection. Furthermore, the performance of nitrogen injection is marginally higher than air injection for heavy oil recovery. However, atmospheric air is free to access while capture and storage of nitrogen from the air is not cheap.

Appendix D: Dispersion Coefficient Calculation for Nitrogen Injection

The initial and optimal $D(\omega,T)$ of nitrogen injection is plotted in Figure 40 at the injection pressure of 0.514 MPa, the physical model permeability of 204 Darcy, and different temperature of 25ºC, 50ºC, 75ºC, and 90ºC. Similar to Figure 19, the value of [$D(\omega,T)$] respect to 25ºC, 50ºC, 75ºC, and 90ºC increase to a maximum value, and then drops toward the end. Moreover, under the set operational conditions, the objective functional decreased monotonically to the minimum as shown in Figure 41. The maximum value of nitrogen dispersion coefficient is 2.556×10^{-5} (m^2/s) which is marginally higher than air dispersion coefficient.

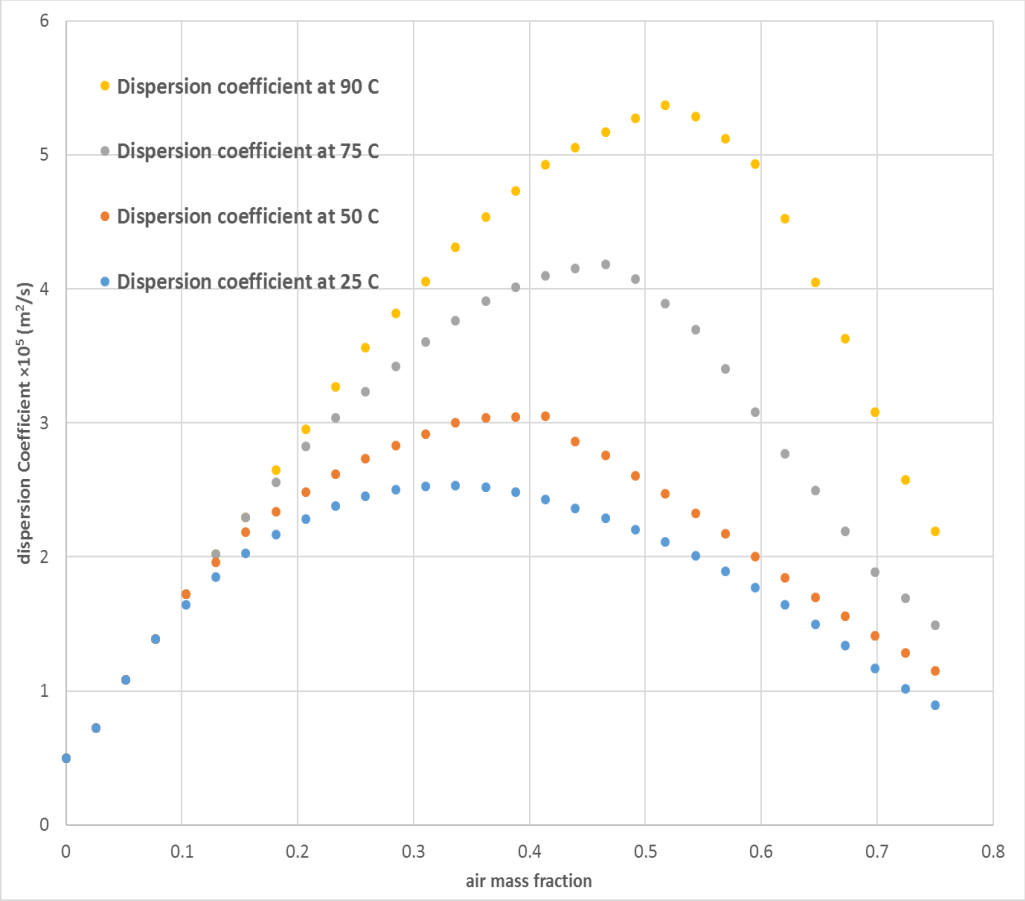

Figure 40: Dispersion coefficient function of nitrogen in heavy oil at different temperatures (25ºC, 50ºC, 75ºC, and 90ºC) (Pressure 0.514 MPa; Permeability 204 Darcy)

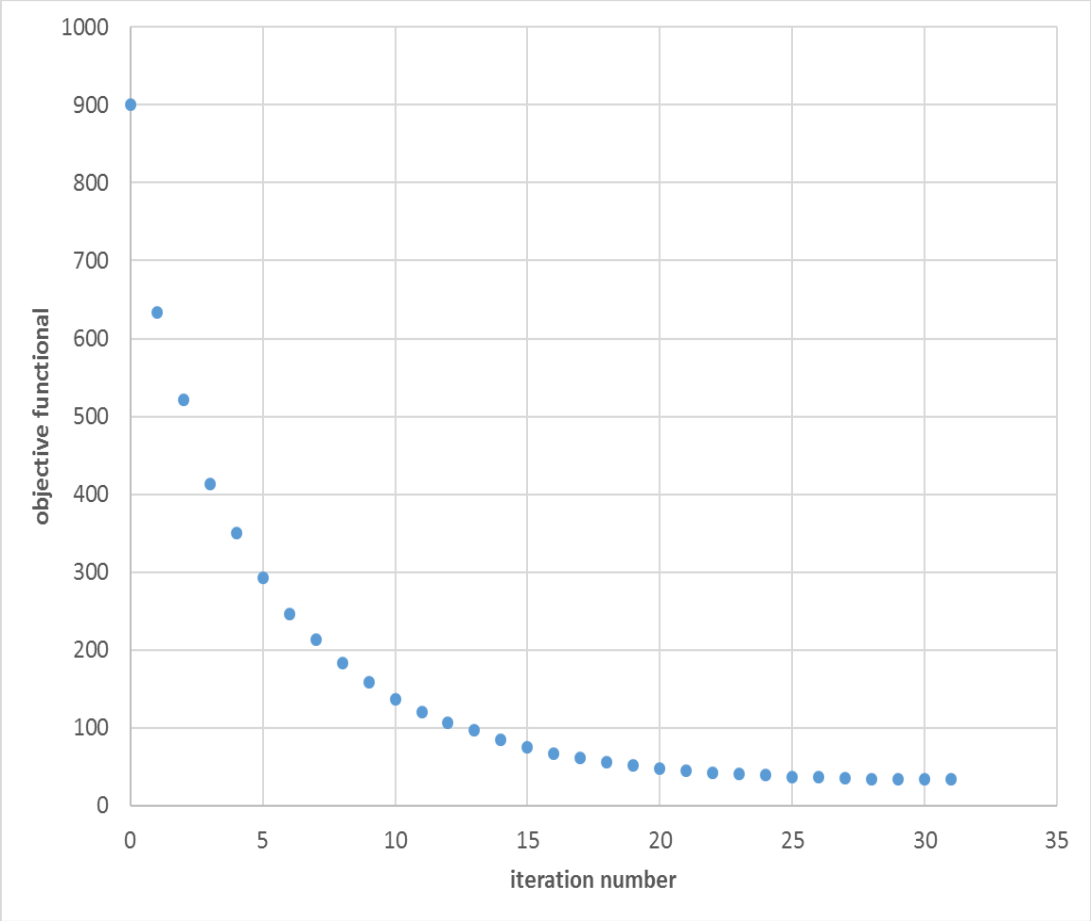

Figure 41: Nitrogen objective functional versus iteration number (Pressure 0.514 MPa; Permeability 204 Darcy)

Appendix E: Optimal Control Policy for Nitrogen Interfacial Temperature

Figure 42 shows the nitrogen interfacial temperature versus time policy for different iteration based on an initial guess of a constant interfacial temperature of 90°C at the pressure of 0.514 MPa and physical media permeability of 204 Darcy for 165 minutes of operational time. It resulted in an iterative increasing of the objective functional accompanied to the maximum improvement in [$T_{int}(t)$]. The objective functional increased monotonically to the highest value of 181.12 (Figure 43).

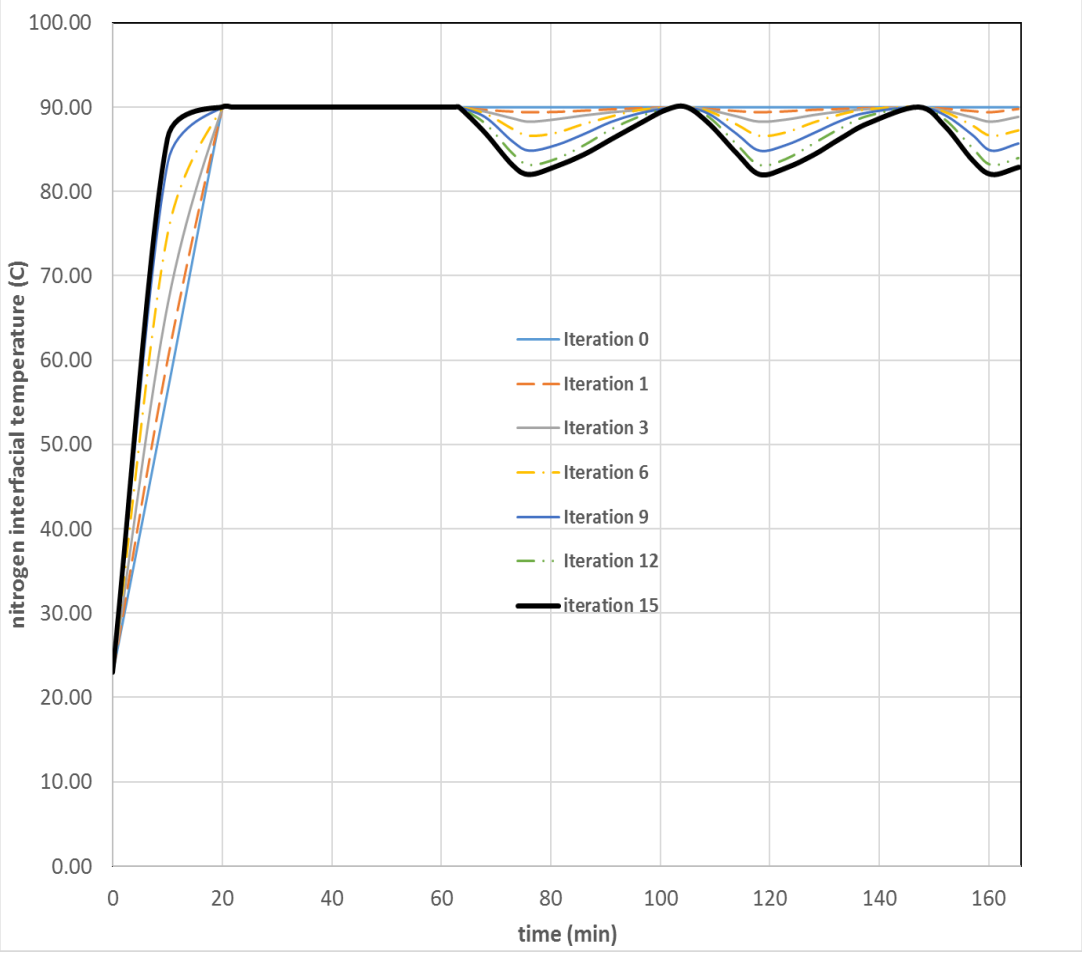

Figure 42: The nitrogen interfacial temperature $T_{int}(t)$ at different iterations of the optimal control algorithm under an initial guess of the constant temperature of 90°C

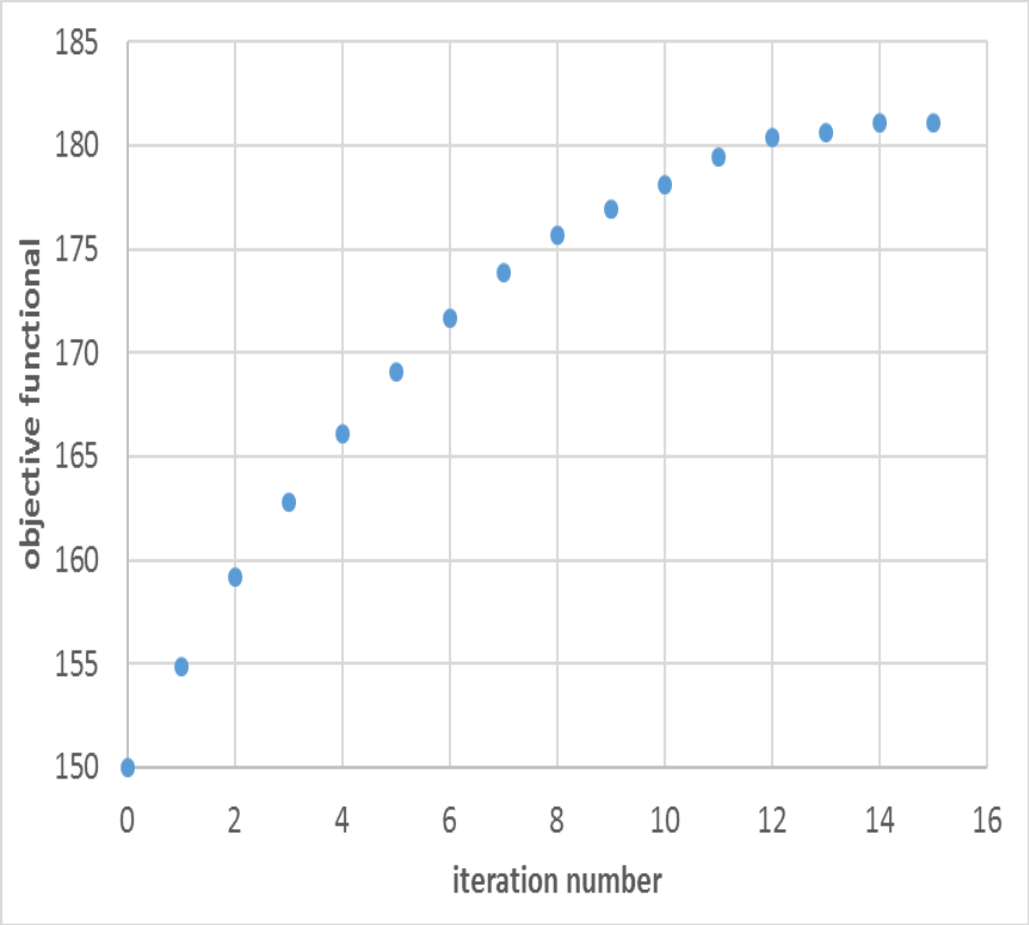

Figure 43: Nitrogen objective functional versus iteration number (204 Darcy and Pressure 0.514 MPa)

Validation of Optimal Control Policy for Nitrogen Injection

Figure 44 shows that the experimental and calculated heavy oil recovery agree very well under the determined optimal [$T_{int}(t)$]. Thus, the average of relative errors at all sample times in the mass of heavy oil recovered was 2.01%. Furthermore, this figure shows the difference between the experimental optimal interfacial temperature and simulated interfacial temperature is very small with the average relative error less than 2%. Therefore, the little relative error demonstrates that we were able to validate the optimal control policy for nitrogen injection. Lastly, according to the results obtained (Figure 43), the optimal [$T_{int}(t)$] policy enhances the heavy oil recovery significantly, with resulting in heavy oil recovery by 20.73% in comparison to the constant temperature of 90^{o}C.

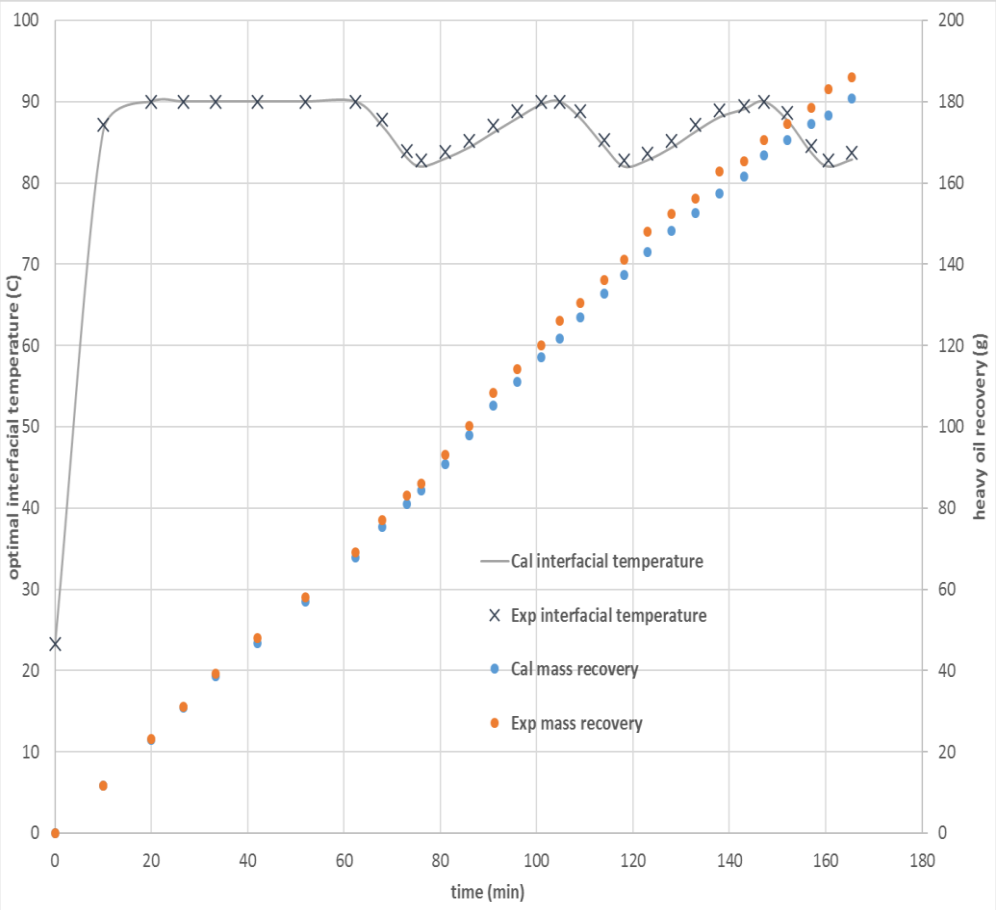

Figure 44: Experimental and calculated mass of live oil produced with time (Pressure 0.514 MPa, 204 Darcy, Solvent Nitrogen)

Appendix F: Permeability Effect on Optimal Policy for Nitrogen Injection

Figures 45, 46, and 47 show the objective functional versus iteration number for nitrogen injection at 427, 87, and 40 Darcy, respectively.

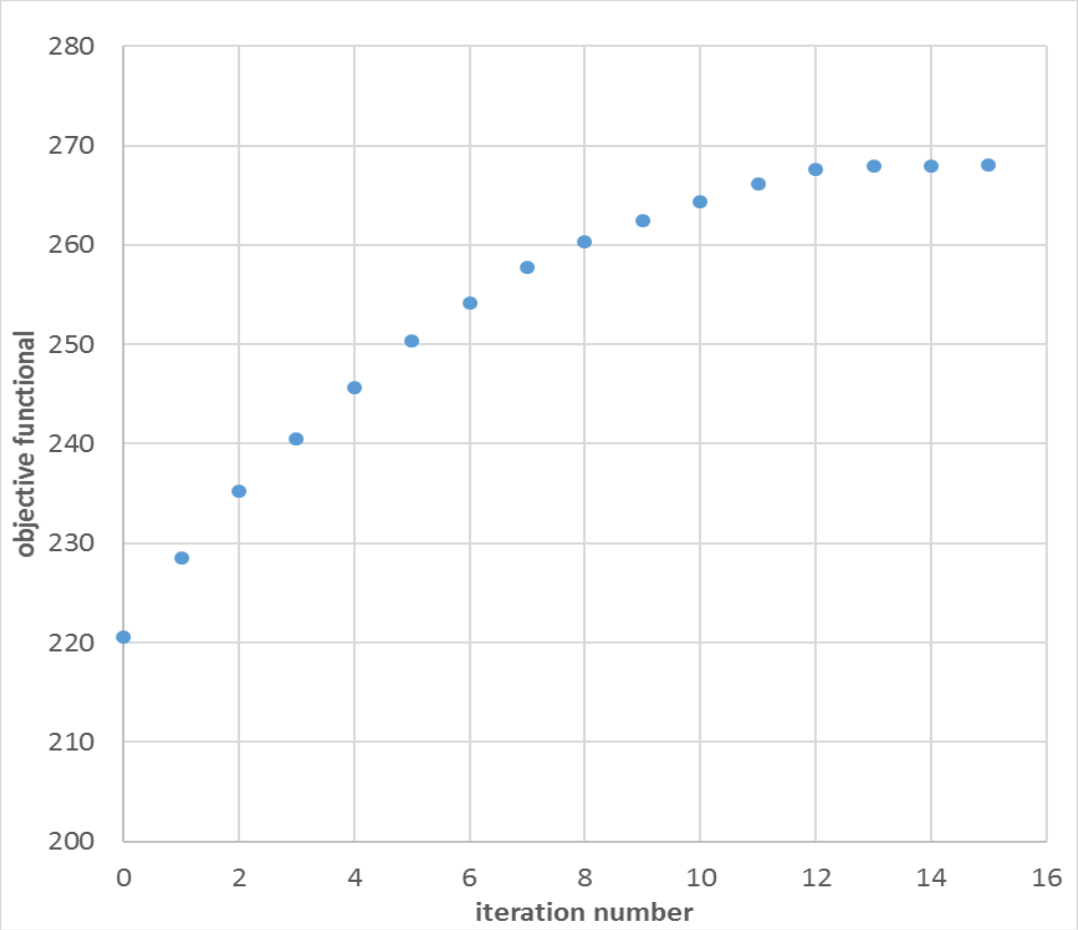

Figure 45: Nitrogen objective functional versus iteration number (427 Darcy and Pressure 0.514 MPa)

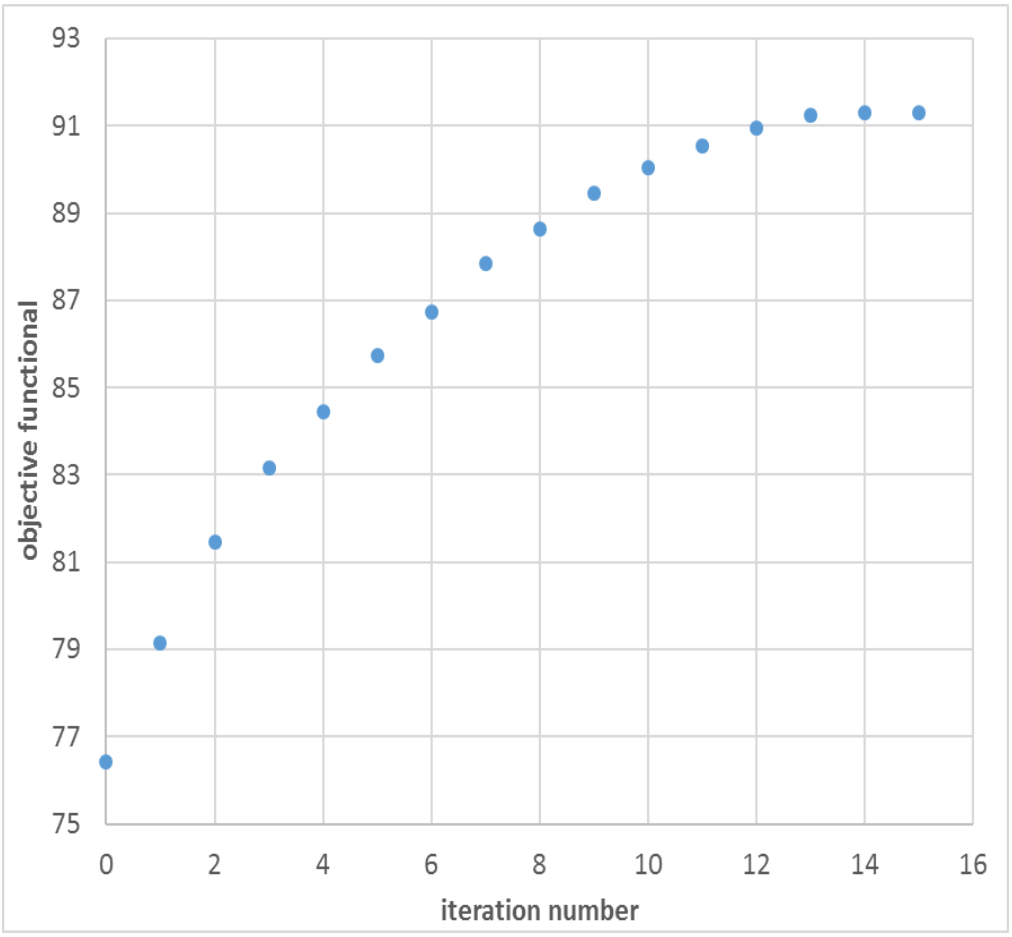

Figure 46: Nitrogen objective functional versus iteration number (87 Darcy and Pressure 0.514 MPa)

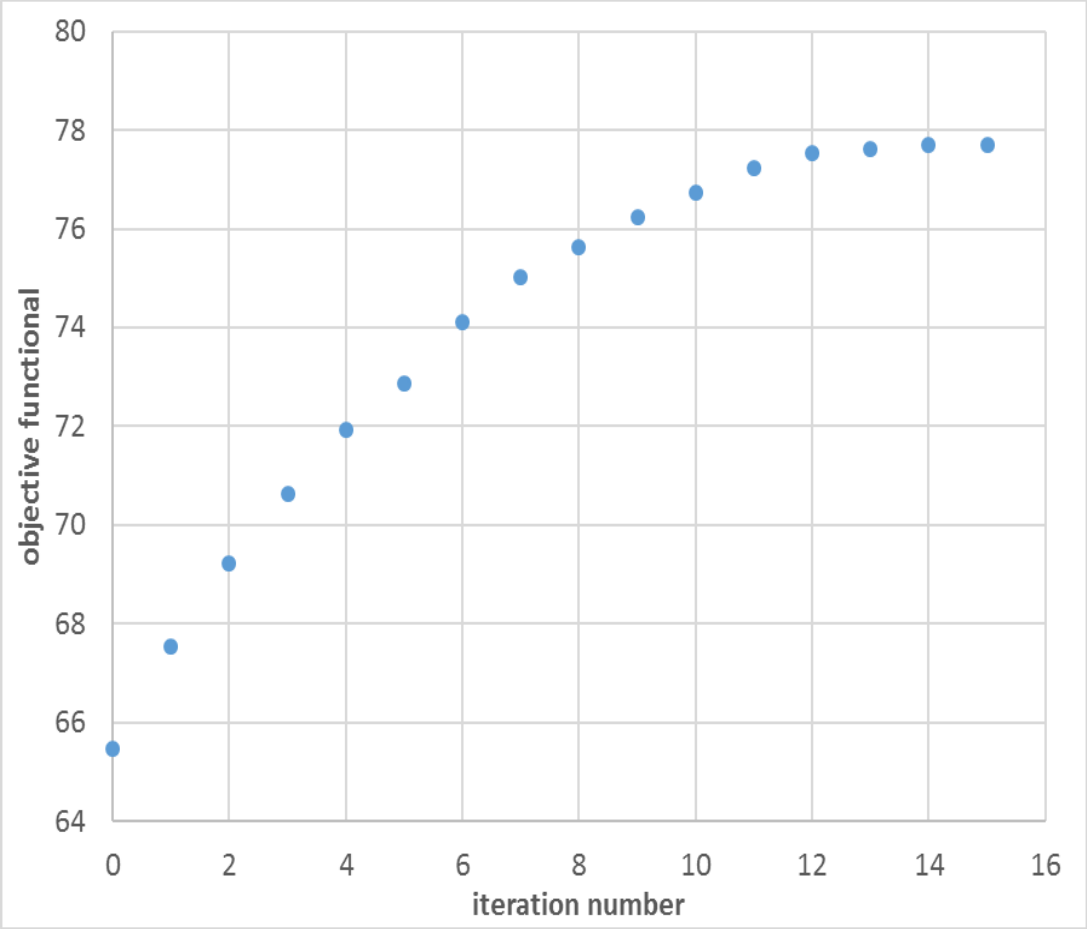

Figure 47: Nitrogen objective functional versus iteration number (40 Darcy and Pressure 0.514 MPa)

Validation of Optimal Control Policy for Nitrogen Injection at Different Permeability

Figure 48 shows the comparison between the calculated objective functional versus the experimental value at three different packs of permeability of 40, 87, and 427 Darcy. The average of relative errors for 40, 87, and 427 Darcy at all sample times in the mass of heavy oil recovered were found to be 2.2%, 3%, and 3.9%, respectively.

Thus, the calculated objective functional agree very well with experimental value at different permeability.

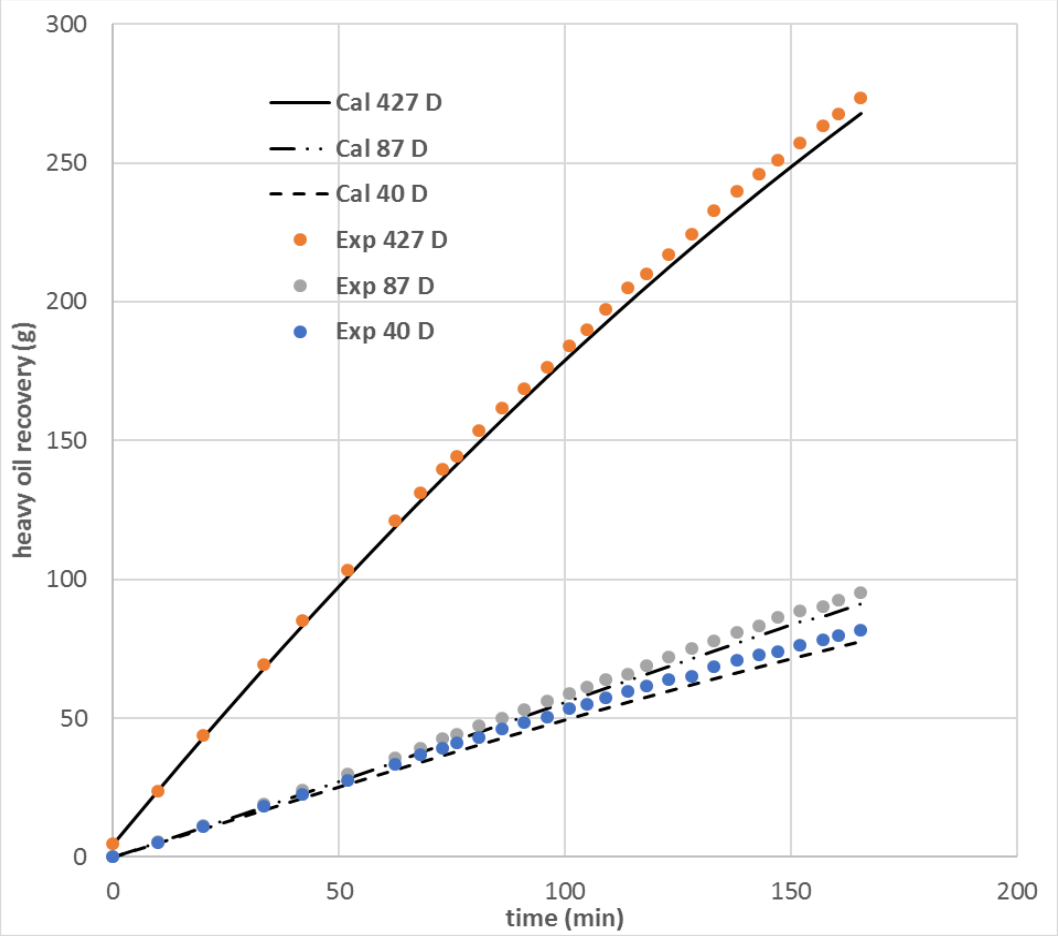

Figure 48: Experimental and calculated heavy oil recovery using Nitrogen at three different medium permeability

References

1. Lyons, W.C.; Plisga, G.J. *Standard Handbook of Petroleum and Natural Gas Engineering, 2th ed.*; Elsevier, Amsterdam, Netherlands, 2005; pp 7-11.
2. National Energy Board, *Canada's Oil Sands - Opportunities and Challenges to 2015: An Update*. *An Energy Market Assessment June 2006 Calgary*; http://www.neb-one.gc.ca/nrg/sttstc/crdlndptrlmprdct/rprt/archive/pprtntsndchllngs20152006/pprtntsndchllngs20152006-eng.pdf, 2006; accessed in 22 October,2016; pp viii-x, 27-28.
3. Alvarado, V.; Manrique E. *Enhanced Oil Recovery - Field Planning and Development Strategies*; Gulf Professional Publishing, Texas, 2010; pp 7-11, 43-64, 133-153.
4. Head, I. M.; Jones, D. M., and Larter, S. R. *Nature*, **2003**, 426, 344–352.
5. Larter, S.; Whilhelins, A.; Head, I; Koopmans, M; Aplin, A; Di Primio, R; Zwach, C; Erdmann, M; Telnaes, N; *Org. Geochem*, **2003**, 34, 601–613.
6. Larter, S.; Huang, H.; Adams, J.; Bennett, B.; Jokanola, O.; Oldenburg, T.; Jones, M.; Head, I.; Riediger, C.; Fowler, M.; *American Association of Petroleum Geologists Bulletin*, **2006**, 90, 921–938.
7. Meyer, R. F; Attanasi, E. D; Freeman, P. A; *Heavy Oil and Natural Bitumen Resources in Geological Basins of the World. US Geological Survey*, Virginia, 2007, Accessed March 22, 2017, http://pubs.usgs.gov/of/2007/ 1084/OF2007-1084v1.pdf
8. Speight, J.G. *Enhanced Recovery Methods for Heavy Oil and Tar Sands*; Gulf Publishing Company, Texas, 2009; pp 221-255.
9. Jayasekera, A. T.; Goodyear, S. G.; *SPE Reservoir Evaluation & Engineering*, **2000**, 3, 371–379.
10. Shah A.; Fishwick, R.; Wood, J.; Leeke, G.; Rigby, S.; Greaves, M. *Energy Environ. Sci.*, **2010**, 3, 700–714
11. Banerjee, D.K. Oil Sands, *Heavy Oil & Bitumen - From Recovery to Refinery*; PennWell, Oklahoma, 2012; pp 59-64.
12. Upreti, S.R.; Lohi, A.; Kapadia, R.A.; El-Haj, R. *Energ. Fuel*.2007, 21, 1562-1574
13. In Encyclopedia of Physical Science and Technology 3rd Edition, vol. 18. Robert A. Meyers Ed., Academic Press, 2001, pp 503-518

14. Stosur, G.J. *EOR: Past, Present and What the Next 25 Years May Bring; Proceedings of the Society of Petroleum Engineers (SPE)*; Kuala Lumpur, Malaysia, October 20-2, 2003 (SPE 84864).
15. Abu El Ela, M.; Samir, M.; Sayyouh, H.; El Tayeb, S. *Oil. Gas. J*.**2008**, 106, 40-45.
16. Satter, A.; Iqbal, G.M.; Buchwalter, J.L.; *Practical Enhanced Reservoir Engineering: Assisted with Simulation Software*. PennWell, Oklahoma, 2008, pp 549-566
17. Li, W.; Mamora, D.D. *Phase Behavior of Steam with Solvent Co-injection under Steam Assisted Gravity Drainage (SAGD) Process*; SPE EUROPEC/EAGE Annual Conference and Exhibition, Barcelona, Spain 14-17 June, 2010 (SPE 130807).
18. Alvarez, J.; Han, S.; *Journal of Petroleum Science Research*. **2013**, 2, 116-127.
19. Upreti, S.R.; Mehrotra, A.K. *Can. J. Chem. Eng*.**2002**, 80, 116-125.
20. Manrique, E.J.; Thomas, C.P.; Ravikiran, R.; Kamouei, M.I.; Lantz, M.; Romero, J.L.; Alvarado, V. *EOR: Current Status and Opportunities*; SPE Improved Oil Recovery Symposium, Oklahoma, USA 24-28 April, 2010 (SPE 130113).
21. Dooley, J.J.; Dahowski, R.T.; Davidson, C.L. *CO2-driven Enhanced Oil Recovery as a Stepping Stone to What?*; U.S. Department of Energy, http://www.pnl.gov/main/publications/external/technical_reports/PNNL-19557.pdf, 2010; accessed in 12 February, 2014; pp 2-27.
22. Alvarado, V.; Manrique, E. *Energies*. **2010**, 3, 1529-1575.
23. Moritis, G. *Oil. Gas. J*.**2008**, 106, 41–42, 44–59.
24. Huang, T.; Zhou, X.; Yang, H.; Liao, G.; Zeng, F. *Petroleum*. **2017**, 3, 68-78
25. Telmadarreie, A., *Evaluating the Potential of CO2 Foam and CO2 Polymer Enhanced Foam for Heavy Oil Recovery in Fractured Reservoirs: Pore-Scale and Core-Scale Studies*. PhD's thesis, University of Alberta, Alberta, Canada. 2017, pp 7-17, 36-39
26. Manrique, E.J.; Muci, V.E.; Gurfinkel, M.E. *Reserv. Eval. Eng*.**2007**, 10, 667–686.
27. Moritis, G. *Oil. Gas. J*.**2001**, 99, 68–73.
28. Muggeridge, A.; Cockin, A.; Webb, K.; Frampton, H.; Collins, I.; Moulds, T.; Salino, P. Phil. *Trans. R. Soc. A*.**2014**, 372, 20120320.
29. Rafiq Islam, M.; Chhetri, A.B.; Khan, M.M. *Greening of Petroleum Operations: The Science of Sustainable Energy Production*. Wiley-Scrivener Publishing LLC, Massachusetts, 2010, pp 577-633

30. Gurgel, A.; Moura, M.C.P.A.; Dantas, T.N.C.; Barros Neto, E.L.; Dantas Neto. A.A.; *Brazilian Journal of Petroleum and Gas.* **2008**, 2, 83-95.
31. Sheng, J., *Modern Chemical Enhanced Oil Recovery - Theory and Practice*. Elsevier, Amsterdam, 2011, pp 101-206, 239-335, 501-567
32. Sandersen, S.B., *Enhanced Oil Recovery with Surfactant Flooding*. PhD's thesis, Technical University of Denmark, Copenhagen, Denmark. 2012, pp 6-20
33. Lazar, I.; Petrisor, I.G.; Yen, T.F.; *Petrol. Sci. Technol.* **2007**, 25, 1353-1366.
34. Fan, C.; Zan, C.; Zhang, Q.; Shi, L.; Hao, Q.; Jiang, H.; Wei, F. *Ind. Eng. Chem. Res.***2015**, 54, 6634−6640.
35. Wang, C.; Liu, H.; Pang, Z.; Wang, J.; Chen, C.; Wang, C.; Wu, Z. *Energy Fuels*. **2015**, 29, 6242−6249.
36. Butler, R. M.; Mokrys, I. J. J. *Can. Pet. Technol*. **1991**, 30, 97-106
37. Das, S. K.; Butler, R. M. J. *Pet. Sci. Eng*. **1998**, 21, 43-59
38. Kapadia, R.A. *Dispersion Determination in Vapex: Experimental Design, Modeling and Simulation.* Master's thesis, Ryerson University, Toronto, Ontario, Canada, 2004, pp 11-26
39. Lederer, E. L. *Proceedings of World Petroleum Congress*, South Kensington, London, July 19-25, 1933; Dunstan, A. E., Sell, G., Eds.; Offices of the Congress: London, 1934.
40. Das, S. K.; Butler, R. M. *Can. J. Chem. Eng*. **1996**, 74, 985-992
41. Jin, W. *Heavy Oil Recovery Using the Vapex Process*. Master's thesis, University of Waterloo, Waterloo, Ontario, Canada, 1999, pp 11-26
42. Upreti, S.R.; Mehrotra, A.K. *Ind. Eng. Chem. Res*.**2000**, 39, 1080-1087
43. Hayduk, W.; Cheng, S. C. *Chem. Eng. Sci*. **1971**, 26, 635-646
44. Perkins, T. K.; Johnston, O. C. *SPE J.* **1963**, 3, 70-84
45. Pal, K.; Joyce, M.K.; Fleming, P.D., *TAPPI JOURNAL*. **2006**, 9, 1-3
46. Ediriweera, M.P.; Halvorsen, B.M., *A Study of the Effect of Relative Permeability and Residual Oil Saturation on Oil Recovery*; Proceedings of the 56th SIMS, Linkoping, Sweden, October 07-09, 2015
47. Kirk, D., Optimal Control Theory: An Introduction, Courier Corporation, 2004, 167-177
48. Upreti, S. R., *Optimal Control for Chemical Engineers*, 1 edition, Taylor and Francis Group, FL, USA, CRC Press, 2012, pp 57-85, 185-231, 235-265

49. Abukhalifeh, H. *Determination of Concentration-dependent Dispersion of Propane in Vapor Extraction of Heavy Oil*; PhD thesis, Ryerson University, Canada, 2010, pp 89-95, 98-104
50. Muhamad, H. *Optimal Control of Vapor Extraction of Heavy Oil*; PhD thesis, Ryerson University, Canada, 2012, pp 33-34, 59-86, 94-97
51. El-Haj, R. *Experimental Determination of Solvent Gas Dispersion in Vapex Process*; MASc Thesis, Ryerson University, Canada, 2007, pp 28-35, 56-68
52. Oduntan, A.R. *Heavy Oil Recovery Using the Vapex Process: Scale Up and Mass Transfer Issues*. Master's Thesis, University of Waterloo, Waterloo, Canada, 2001, pp 12-30
53. Muhamad, H.; Upreti, S. R.; Lohi, A.; Doan, H. *Energy & Fuels*.**2012**, 26, 3514−3520
54. Moghadam, S.; Nobakht, M.; Gu, Y. *J. Pet. Sci. & Eng*.**2009**, 65, 93–104
55. Hepler, L.G.; Hsi, C. *AOSTRA Technical Publication Series #6: Technical Handbook on Oil Sands*; Bitumens and Heavy Oils, Alberta Oil Sands Technology and Research Authority, Alberta 1989; pp 281-300.
56. Ajumobi, A. *A Study on the Heavy Crude Oil Viscosity Reduction with the Dissolution of Nitrogen and Carbon Dioxide*; MASc Thesis, The City College of New York, U.S., 2015, pp 18, 27-31, 36-37.
57. El-Haj, R.; Lohi, A.; Upreti, S.R. *J. Pet. Sci. Technol*.**2009**, 67, 41-47.
58. Mailybaev, A.A.; Bruining, J.; Marchesin, D. *Combustion and Flame* **2011**, 158, 1097-1108.
59. Khoshnevis Gargar, N. *Combustion for Enhanced Recovery of Light Oil at Medium Pressures*. MASc Thesis, University of Calgary, Canada, 2014, pp 71-90.
60. Galas, C.; Clements, A.; Jaafar, E.; Jeje, O.; Holst, D.; Holst, R. *Identification of Enhanced Oil Recovery Potential in Alberta phase 2 Final Report for Energy Resources Conservation Board*. http://www.ags.gov.ab.ca/publications/pdf_downloads/ercb-eor-report2.pdf, 2012; accessed in 14 October, 2015; pp 2-14.
61. Imran, M. *Dispersion Coefficient Determination in Vapex Process*. MASc Thesis, Ryerson University, Canada, 2008, pp 56-65.